Utilising optical Kerr microresonators for polarisation control, logic gates, and quantum optics applications

Imperial College London

Department of Physics

Niall Patrick Moroney

Thesis submitted for the degree of Doctor of Philosophy

Abstract

When high intensities of light are focused inside of a medium, strange effects occur. Light can self-interact. It can be slowed down based on how bright it is, it can be made to go in one direction but not the other, and it can even be made to change colour.

It is hard to imagine how the world would look if these were effects that we experienced in our everyday lives. Fortunately, it takes a significant amount of effort to make the conditions right for such events to occur, specifically, with high optical intensities required. This thesis details some of these efforts.

In this work, I present some applications of Kerr microresonantor based nonlinear and quantum optics. Microresonators are minute devices that can be integrated in photonic circuits. They trap and guide light on a repeating path, with each round-trip leading to an increase in intensity until nonlinear effects start to occur.

I start by explaining how such resonators work, are fabricated, and how nonlinear effects can manifest. Next, an all-optical polarisation controller is introduced, in which the nonlinear splitting of otherwise degenerate polarisation modes is employed. This device could find application in integrated photonic circuits that require fast response times. A similar effect, but this time for counter-propagating light, is then used to demonstrate an all-optical, universal logic gate. Interestingly, a set of such logic gates could be used for the on-chip routing of optical signals to provide low-latency communications for telecoms and distributed computing. Finally, the quantum nature of these nonlinearities is explored, first with the calculation of multi-modal entanglement metrics before then discussing work that is progressing towards a single-photon source. These phenomena show promise for integration into future quantum technologies, in particular in secure quantum communications and for state generation for quantum information processing.

Statement of Originality

I hereby state that I am the sole author of this work, which has not been submitted for any other degree at any University or Institution. To the best of my knowledge, it does not infringe upon the copyright of any other work, which are fully acknowledged with suitable references.

Declaration

Dedication

This thesis is dedicated to all of the scientists and healthcare professionals who have shown throughout the Covid-19 pandemic that the application of science is a powerful tool for the betterment of humankind.

Acknowledgements

I've been incredibly lucky during this period to work at a number of fantastic institutions alongside some truly brilliant scientists of whom there are too many to thank each individually. However there are some who have really made these recent years an unforgettable experience who I would like to show my appreciation.

Firstly, it is said that the most important part of choosing a PhD project is picking a good supervisor. I was fortunate enough to pick two. The first half of my research was conducted at the National Physical Laboratory under the supervision of Pascal Del'Haye, who really introduced me to experimental physics. The friendly environment he fostered in which (at times stupid) questions could be asked freely made this process far easier than it could have been, allowing me to truly get to grips with the subject matter. I'm also very grateful to Pascal for inviting me to join him in his new group at the Max Planck Institute for the Science of Light in Germany.

Understanding my dual desire to move back to London and begin work in quantum optics, my second supervisor - Michael Vanner - was extremely supportive. His group had recently moved to Imperial College London when I joined and it was really incredible to see the kind of progress that had been achieved in spite of the Covid-19 pandemic. Michael's background in both theoretical and experimental quantum optics led to some really fascinating discussions, and his background as an Australian led to some really terrifying discussions about his motherland's fauna.

Fellow members of these groups include: Leonardo Del Bino, possibly the most practically minded person I have ever met (and to whom I owe a demonstration of the catastrophic failure of an erbium doped fiber amplifier). Michael Woodley, with whom conversation can range from the categories of chaotic dynamics, the merits of Russian choral music, philosophy, and word-for-word recitals of 1960's absurdist sketches (all over the course of a single pint). Jonathan Silver, who is annoyingly intelligent. Shuangyou Zhang, who embodies hard work and patience, and reaps both of their rewards. Giorgos Ghalanos, whose love for safety is only eclipsed by that of his love for steak. Andreas Svela, the only person I've met who writes readable code. Toby Bi, with whom I shared some really fun trips. John Price, who hates tapered fibers even more than I do. Lars Freisem, for our mutual love of cowboy games. Evan Cryer-Jenkins, even if he doesn't really believe that any of us exist. Lydia Kanari Naish, for trying to temper my hatred of Mathematica.

I've been incredibly lucky to spend time with the people I've met at these three institutions, and know that the above list will include some lifelong friends.

Author publications

Journal articles

Moroney, N., Del Bino, L., Zhang, S., Woodley, M. T. M., Hill, L., Wildi, T., Wittwer, V. J., Südmeyer, T., Oppo, G.-L., Vanner, M. R., Brasch, V., Herr, T., Del'Haye, P. (2022) A Kerr Polarization Controller *Nat Commun 13, 398*

Moroney, N. Del Bino, L., Woodley, M. T. M., Ghalanos, G., Silver, J., Svela, A., Zhang, S., Del'Haye, P. (2020) Logic Gates Based on Interaction of Counter Propagating Light in Microresonators *J. Lightwave Technol. 38, 1414-1419*

Zhang, S., Bi, T., Ghalanos, G., **Moroney, N.**, Del Bino, L., Del'Haye, P. (2022) Dark-Bright Soliton Bound States in a Microresonator *Phys. Rev. Lett. 128, 033901*

Del'Bino, L., **Moroney, N.**, Del'Haye, P., (2021) Optical memories and switching dynamics of counterpropagating light states in microresonators *Opt. Express 29, 2193-2203*

Silver, J., Del Bino, L., Woodley, M. T. M., Ghalanos, G., Svela, A., **Moroney, N.**, Zhang, S., Grattan, K. T. V., Del'Haye, P. (2021) A Nonlinear Enhanced Microresonator Gyroscope *Optica 8, 1219-1226*

Ghalanos, G., Silver, J., Del Bino, L., **Moroney, N.**, Zhang, S., Woodley, M. T. M., Svela, A., Del'Haye, P. (2020) Kerr-nonlinearity-induced mode-splitting in optical microresonators *Phys. Rev. Lett. 124, 223901*

Zhang, S., Silver, J., Del Bino, L., Copie, F., Woodley, M. T. M., Ghalanos, G., Svela, A., **Moroney, N.**, Del'Haye, P. (2019) Sub-milliwatt-level microresonator solitons with extended access range using an auxiliary laser *Optica Vol. 6, Issue 2, pp. 206-212*

Conference proceedings

Moroney, N., Del Bino, L., Woodley, M. T. M., Ghalanos, G., Silver, J., Svela, A., Zhang, S., Del'Haye, P. (2021) Kerr Logic Gates based on Counterpropagating Light in Microresonators *Photonics in Switching and Computing paper Tu3A. 5*

Moroney, N., Del Bino, L., Zhang, S., Woodley, M. T. M., Hill, L., Wildi, T., Wittwer, V. J., Südmeyer, T., Oppo, G.-L., Vanner, M. R., Brasch, V., Herr, T., Del'Haye, P. (2021) Spontaneous polarization symmetry breaking of light in a microresonator *Conference on Lasers and Electro-Optics (CLEO) Europe paper CD-4.2*

Moroney, N., Del Bino, L., Woodley, M. T. M., Ghalanos, G., Silver, J., Svela, A., Zhang, S., Del'Haye, P. (2020) Logic Gates based on Interaction of Counterpropagating Light in Microresonators *Frontiers in Optics (FiO) paper FW4D.7*

Moroney, N., Del Bino, L., Woodley, M. T. M., Ghalanos, G., Silver, J., Svela, A., Zhang, S., Del'Haye, P. (2019) Logic Gates based on Interaction of Counterpropagating Light in Microresonators *Conference on Lasers and Electro-Optics (CLEO) paper STh3J.7*

Patents

EU patent application, PCT/EP2021/051953 *Polarization alteration device and method for adjusting the polarization of an optical wave.*

Contents

Chapter 1

Introduction

> The endeavor to understand is the first and only basis of virtue
>
> Baruch Spinoza

The ever increasing rate of scientific and technological progress is a staggering thing to behold, sometimes appearing as an ever growing organism beyond human control or comprehension. I've been lucky enough to spend these past several years looking at the workings of this machine and helping to make contributions to the fascinating subject of optics. This thesis encapsulates my findings.

My focus has been in two distinct fields and their intersection: nonlinear photonics and quantum technologies. I will use this chapter to motivate research in these areas and showing how they can be applied together naturally. A short summary of the structure of the rest of the document will then be given.

*Photon*ics, like *electron*ics, is a technological field in which *photons* (rather than *electrons*) are the physical medium which is exploited as a tool to realise various applications. The ubiquity of electronics in all aspects of life makes it hard to appreciate just how much of an effect it has had on the human experience. If photonics has but a tiny fraction of this impact, it will have justified all the time and resources invested.

Why then does photonics not find equally ubiquitous application? Whereas Volta invented the battery - a stable source of electrons - in 1800, the laser (which is key for photonics) wasn't invented until 1960 [1]. Many applications require the exploitation of nonlinear effects which is relatively simple to do in electronics as the Pauli exclusion principle can lead to current blockade in doped semiconductors [2]. Light however, is made up of bosonic photons which do not succumb to the Pauli exclusion principle. Nonlinear effects cannot manifest from photon-photon interactions alone - they must be mediated by a host material. This has been a focus of the last 60 years; fabricating photonic devices that can guide and confine light, creating complex optical circuits for various applications.

The behaviour of light has always fascinated humankind. As a visual species, light gives us our primary means of observing our surroundings and so it is of no surprise that optical effects were of great interest to early thinkers. Indeed, many philosophers of the ancient world saw light as a fundamental component of reality, a concept shared by particle physics today! Ibn al-Haytham, the so-called "father of modern optics", pioneered an early version of the scientific method to increase

our understanding, solidifying the concept of light rays. The enlightenment then gave a series of leaps in our understanding and mastery of light. Galileo's use of lens technology to invent the telescope had birthed a new form of astronomy, and began a new interest in the mechanics of light's behaviour. This famously led to two competing ideas, from two intellectual titans, of the underlying nature of light: Issac Newton's *corpuscular* theory (which would today be described as a *particle* theory), and Christiaan Huygens *wave* theory. As a better descriptor of the diffraction, Huygen's wave model was preferred by contemporary physicists, but the story didn't end there [3].

In 1905, Albert Einsten showed that the photoelectric effect could only be described by a *quantised* field [4], confirming earlier thoughts Max Plank had when considering blackbody radiation [5]. Such quantised systems were said to have a *wave-particle* duality: both Newton and Huygens were correct, but neither had a complete understanding. In some senses light acts as a wave, in some senses it acts as a particle. Such particles were termed *photons*. Theoretical work to describe these phenomena, initiated by Paul Dirac, became the first example of a *quantum field theory* which now give us our most sophisticated understanding of the microscopic world.

The advent of the laser was the development that truly brought *nonlinear* and *quantum optics* into being. Consisting of a gain medium inside of a cavity, which amplifies and outputs only well-defined optical states, precise control of light was now possible [1]. These systems have since been used to develop multiple technologies, with particular success in telecommunications using optical fiber technology [6], and the manufacturing of semiconductor chips which have underpinned the electronics industry [7].

1974 saw the first observation of an important nonlinear phenomenon: optical bistability [8–10]. Bistability describes a system which can have two distinct output states for the same input. *Electronic* bistability is the concept which underpins all (classical) electronic information processing and storage technology. Accordingly, there was significant interest in developing optical devices to mimic their electronic counterparts [11–13]. The weak nature of light-matter interactions is double edged: on the one hand, this leads to low signal absorption allowing for the transmission of information over great distances with modest input power in fiber optic networks. However, it creates difficulties in achieving the optical nonlinearities required for the realisation of bistability based information processing devices. Luckily, there is a way to enhance light-matter interactions: the optical resonator.

Resonance is an effect that is ubiquitous in physics and engineering. When a system is driven by an oscillation, it will itself begin to oscillate. When driven at the correct frequency, these oscillations constructively interfere, potentially growing in amplitude far beyond that of the input itself. This idea underpins the optical resonator: input light is made to traverse a repeating path around an optical cavity. When the input field is of the correct frequency, it is entirely in phase with the cavity field leading to constructive interference and hence intensity buildup. When the cavity round-trip losses are low, extreme intensity buildup is possible.

Thus, optical resonators allow for the build up of high intensities, allowing for the exploitation of nonlinear effects with only modest input powers. Accordingly, optical resonators are an important tool for the development of practical photonic devices, and indeed the first demonstration of optical bistability was completed using

a Fabry-Pérot cavity [8].

In the decades since these first demonstrations of prototype optical devices, much work has gone into developing them into a useful technology. This is best exemplified in the field of optical communications, with fiber optic networks underpinning global telecoms and the internet. Previous work has broken these applications into three main categories: diversifying laser light (e.g. through the generation of pulses or new colours), material interaction, and information processing [13]. Of particular interest is the frequency comb - a set of equidistant frequency modes that are all mutually phase locked, the invention of which earned its inventors, John Hall and Theodor Hänsch, half of the 2005 Nobel Prize in Physics [14, 15]. Allowing the coherent links between different parts of the electromagnetic spectrum, this technique has allowed for improved precision in time keeping, spectroscopy, and waveform generation and is likely to be a key component in the LIDAR systems used by autonomous vehicles [16]. In particular, progress in integrating frequency combs - so called *Kerr combs* - onto photonic chips is a promising route to a future commercial technology [17, 18].

Another field that promises to develop exciting new technologies is quantum optics. In their seminal work of 2000, Knill, Laflamme and Milburn showed that linear optical devices and single photon sources/detectors are sufficient to construct a universal quantum computer which has been shown to be able to outperform classical information processing systems [19, 20]. Quantum optics can also be used with existing fiber optics technology to provide provably secure communications over long distances and at high speed [21].

In quantum optics, the outputs of a laser are called *coherent states*, and are the analog of the classical harmonic oscillator. Similarly, such states propagate rather unremarkably through empty space - the bosonic nature of photons means they don't typically interact with each other. How then, are quantum and nonlinear optical effects produced? Laser light must interact with matter.

A key early demonstration of an optical state that could *only* be described using a quantum description was given by Jeff Kimble et al. in 1977 [22]. Here, Sodium atoms were resonantly excited such that they absorb an input photon which is then emitted fluorescently. As this process happens one-at-a-time, the statistics are said to be *anti-bunched* - direct evidence for the quantised nature of light.

The real marriage between nonlinear and quantum optics was shown in the 1980s with the generation of *squeezed states* [23]. Optical states can be described using two non-commuting observables (such as the amplitude and phase quadratures), which obey Heisenberg's uncertainty relations. Coherent states share this uncertainty equally between both quadratures, though squeezed states sacrifice certainty in one quadrature to increase it in the other. Accordingly, squeezed states have a great interest to metrology, and have recently been implemented into the LIGO interferometer to improve the resolution of gravitational wave astronomy [24]. Again, our increased understanding of the mechanics of light has given us a new way to observe our universe.

Nonlinear optics can lead to squeezed state generation by the coupling of different optical fields by a host material's nonlinear susceptibility. This can be achieved by the electric dipole that is induced in a medium by incident electric fields. For low intensity input fields, the induced dipole response is small and thus only affected by the host atom, giving a linear response. For input fields of higher intensity, the dipole response becomes affected by neighbouring atoms, giving a nonlinear response

which can couple fields of different frequency in a way that leads to squeezed states [23, 25]. This was first demonstrated in the mid-1980s using two different types of material nonlinearity [26, 27].

Since then, quantum optics has made a number of impressive advancements both in terms of fundamental physics and technological progress. The non-local nature of quantum entanglement has been proven by Bell test violations [28], quantum states have been teleported [29], and photonic quantum computation is also making rapid progress [30, 31], to name a few major advances. Interestingly, the latter two examples rely on squeezed states, and are pioneering works in the fields of quantum communication and information processing.

Thus, both classical and quantum information processing technologies could benefit from the use of on-chip optical resonators. Such devices allow for the realisation of optical nonlinearities with only low input powers required. Furthermore, these devices have a small footprint and are an essential component in any future photonic circuit system.

This thesis focuses on applications using the Kerr-nonlinearity in microresonators, starting with classical before moving onto quantum phenomena. All nonlinear optics requires high optical intensities, which can be generated inside of an optical resonator - a device which allows light to propagate around many times, building up in intensity as it does so. The next chapter describes how this buildup occurs, how to fabricate the required devices, and the origins of the Kerr-nonlinearity and associated phenomena. Next, the spontaneous symmetry breaking of the polarisation of light is presented. This is a form of bistability, and is used to demonstrate an all-optical polarisation controller using the nonlinear resonance splitting of orthogonal polarisation modes of a fiber cavity. Then, using a similar effect, an all-optical (classical) logic gate is presented, which could see application in optical computation or the on-chip routing of light. Then the quantum nature of the Kerr-comb is explored, starting with a chapter developing theory to quantify the associated multi-modal entanglement, showing promise for application in quantum communications networks. Finally, the experimental efforts to use such a system as a heralded single-photon source is discussed, which could see such systems employed in quantum communications, information processing, and measurements.

I have been lucky enough to be involved in a diverse set of projects and, for brevity, this thesis will focus on the work for which I would be considered "first-author". Accordingly, I led the development and execution of all methods here presented along with the subsequent analysis, though with valuable help from my collaborators.

Chapter 2

Background

In this chapter, I detail the underlying concepts and background material to my research. Appreciable nonlinear effects require high optical intensities which were realised by using a suitable resonator. Accordingly, this chapter begins with a discussion on how coupling coherent light to such a resonator leads to a build-up of optical intensity. This leads to a description of the parameters which characterise such a resonator and their physical meaning. Finally, fabrication methods for such cavities, along with the practical methods for coupling light into them, is discussed.

With this understanding of optical resonators, the fundamentals of nonlinear optics is presented. Starting with the origins of optical nonlinearities, there is then a focus on the particular nonlinear effect here studied - the Kerr effect. It is shown that, when one or two resonator modes are studied, this nonlinearity manifests as an intensity dependent refractive index due to the phenomena of self- and cross-phase modulation. Increasing the number of modes that are considered, it is then shown that four-wave mixing can be exploited to generate quantum states of light.

This chapter should not be taken as a complete description of either optical resonators or nonlinear optics (which can be found in e.g. Refs [25, 32]), rather it concerns the topics which are of direct relevance to the work subsequently discussed. Later chapters will then detail the specific phenomena and experimental considerations related to their subject matter, with the reader able to refer back to this chapter for the more general considerations.

2.1 Optical resonators

2.1.1 Types of optical resonator

An optical resonator is simply a device that traps light in a region in space by making it repeatedly follow a closed path multiple times. This results in an increase of the intensity of the light inside the resonator in comparison to that which is input to it. Whispering gallery mode (WGM) and Fabry-Perot (FP) resonators are two common examples, and both have been utilised in this work.

The impact of the advent of optical resonators is difficult to overstate. Building upon the development of the *m*aser, the development of the *l*aser required a resonator for optical wavelengths [1, 33]. The pioneering theoretical work by Fox and Li then furthered the development of practical lasers which have found ubiquitous application in modern technology [34]. Alongside the nonlinear effects that can be

accessed inside optical resonators with only modest input power, optical resonators have recently also been used in the first observation of gravitational waves in the LIGO interferometer, opening up a new way to look into our universe [35].

A WGM resonator (cf. Fig. 2.1a) consists of a circular dielectric structure along with an adjacent waveguide which couples light into/out of the device via their overlapping evanescent fields [36]. The cavity field is then guided around the interface of the dielectric via total internal reflection, with cavity intensity building up when there is constructive interference with the input after a round trip.

A FP resonator (cf. Fig. 2.1b) consists of two co-axial mirrors. The input (output) to (from) the cavity comes from the light that is transmitted through the mirrors, which are taken as having sub-unity reflectivity [37, 38]. In contrast to a WGM resonator, this leads to a standing wave as the field counter-propagates against itself during each half-round trip of the cavity.

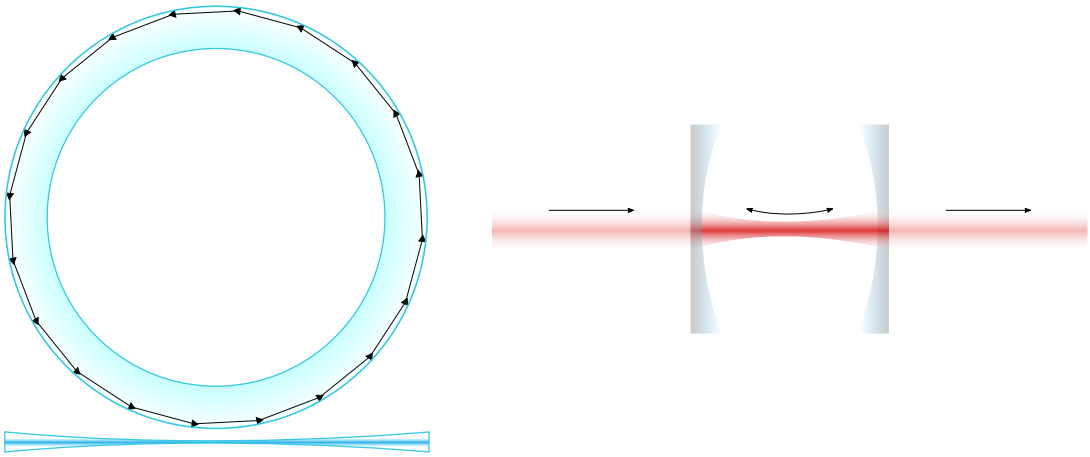

(a) *(b)*

Figure 2.1: Optical resonator types. a) A whispering-gallery mode (WGM) resonator. Light couples into a circular resonator inside which it is guided through multiple round-trips by total internal reflection. b) A Fabry-Perot (FP) cavity. Light couples through a semi-transparent mirror into a cavity in which it undergoes multiple reflections from the bounding mirrors.

Both the WGM and FP cavities have symmetries which make them useful choices for this work. The WGM resonator has a reflective symmetry, leading to degenerate counter-propagating modes. Similarly, the FP cavity exhibits an axial symmetry, leading to degenerate polarisation modes in the absence of any birefringence. These make WGM and FP resonators effective tools for exploring the nonlinear interactions between counter-propagating and orthogonally polarised light respectively.

2.1.2 Build-up of optical intensity

Many of the important parameters which define the characteristics of an optical resonator arise naturally from a model of the constituent fields, as shown in Fig. 2.2. The same model can be used to describe both WGM and FP resonators, though with some negligible differences arising from different path lengths and phase accumulation upon reflection from the FP cavity's mirror. The following model describes the fields of a WGM resonator.

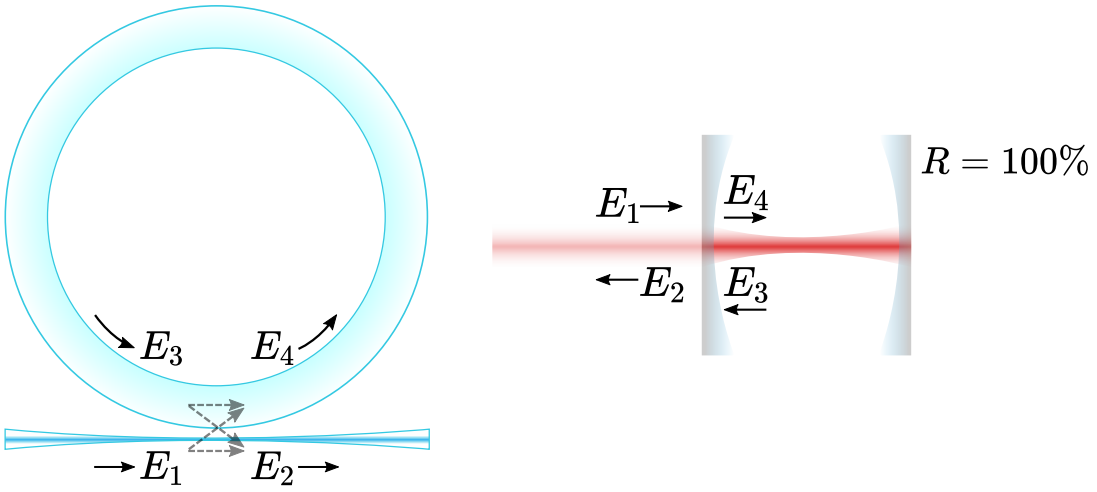

Figure 2.2: Cavity fields with a single coupling location. a) The input field E_1 partially couples into the WGM resonator field E_4, which undergoes loss and phase accumulation as it is guided around the resonator to E_3. Near resonance, this field will constructively interfere with the input field leading to an intensity build-up inside the resonator. The output field E_2 is then the interference between the out-coupled cavity field and the remaining input field. b) A FP cavity is equivalent to a WGM resonator with a single coupling waveguide when one of its mirrors has perfect reflectivity.

Fig. 2.2a shows the important fields for a WGM resonator. An input field, E_1, partially couples into the cavity field E_4. This field propagates around the cavity to E_3, accumulating phase and losing amplitude due to intrinsic losses as it does so. The output field E_2 is then the interference between the input field (which is transmitted past the resonator) and the cavity field that couples out of the resonator. The coupling between the waveguide and cavity fields can be described by the following matrix equation, which treats the coupling as happening at a point, characterised by the reflectivity, r, and transmission, t [39]. The coupling is assumed lossless (i.e. $|r|^2 + |t|^2 = 1$)

$$\begin{bmatrix} E_4 \\ E_2 \end{bmatrix} = \begin{bmatrix} r & it \\ it^* & r^* \end{bmatrix} \begin{bmatrix} E_3 \\ E_1 \end{bmatrix}. \tag{2.1}$$

Also, assuming that all field amplitudes are slowly changing in comparison to the round trip time of the cavity, the fields E_3 and E_4 are related by the following equation, in which t_{RT} is the round-trip time of the light, α is the optical loss rate, and ω is the field frequency:

$$E_3 = e^{t_{\mathrm{RT}}(-\alpha + i\omega)} E_4. \tag{2.2}$$

According to Eq. (2.1):

$$E_4 = rE_3 + itE_1, \tag{2.3}$$

which with Eq. (2.2) becomes:

$$\begin{aligned} E_4 &= re^{t_{\mathrm{RT}}(-\alpha+i\omega)}E_4 + itE_1, \\ E_4\left(1 - re^{t_{\mathrm{RT}}(-\alpha+i\omega)}\right) &= itE_1, \\ \frac{E_4}{E_1} &= \frac{it}{1 - re^{t_{\mathrm{RT}}(-\alpha+i\omega)}}. \end{aligned} \tag{2.4}$$

This gives a way to find the linear relationship between the intracavity field E_4 in terms of the input field E_1 and all relevant cavity parameters. Similarly the relationship between the output field E_2 and input field E_1 can be found from Eq. (2.1):

$$\begin{aligned} E_2 &= it^*E_3 + r^*E_1, \\ &= it^*e^{t_{\mathrm{RT}}(-\alpha+i\omega)}E_4 + r^*E_1, \\ &= \left(it^*e^{t_{\mathrm{RT}}(-\alpha+i\omega)}\frac{E_4}{E_1} + r^*\right)E_1, \\ \frac{E_2}{E_1} &= \frac{r^* - e^{t_{\mathrm{RT}}(-\alpha+i\omega)}}{1 - re^{t_{\mathrm{RT}}(-\alpha+i\omega)}}. \end{aligned} \tag{2.5}$$

2.1.3 Resonator parameters

This section will use Eqs. (2.4) & (2.5) to derive the useful parameters for characterising resonators, which will be used in the remainder of this work.

Build-up factor

As previously mentioned, the light intensity is the most important parameter required for the observation of nonlinear effects. This characteristic is well described by the build-up factor, defined as:

$$\begin{aligned} \left|\frac{E_4}{E_1}\right|^2 &= \left(\frac{it}{1 - re^{t_{\mathrm{RT}}(-\alpha+i\omega)}}\right)\left(\frac{-it^*}{1 - r^*e^{t_{\mathrm{RT}}(-\alpha-i\omega)}}\right), \\ &= \frac{|t|^2}{1 + |r|^2 e^{-2t_{\mathrm{RT}}\alpha} - 2|r|e^{-t_{\mathrm{RT}}\alpha}\cos\left(\omega t_{\mathrm{RT}} + \phi_{\mathrm{r}}\right)}, \end{aligned} \tag{2.6}$$

in which $\phi_{\mathrm{r}} = \arg(\mathrm{r})$ is the phase accumulation from the reflection at the coupling point and will subsequently be taken as 0 with no loss of generality.

Figure 2.3 shows the resonant nature of these optical cavities. The cosine term in the denominator of Eq. (2.6) leads to periodic minima, giving rise to periodic maxima of the cavity intensity - this is resonance - which occurs when the input frequency satisfies $\omega t_{\mathrm{RT}} + \phi_{\mathrm{r}} = n2\pi, n \in \mathbb{Z}$ - the cavity resonance condition, in which n gives the longitudinal mode number for a particular resonance.

Lorentzian lineshape

Resonators are often described as having a Lorentzian lineshape. This arises when taking a small angle approximation for the cosine term in Eq. (2.6) i.e. $\cos(x) \approx$

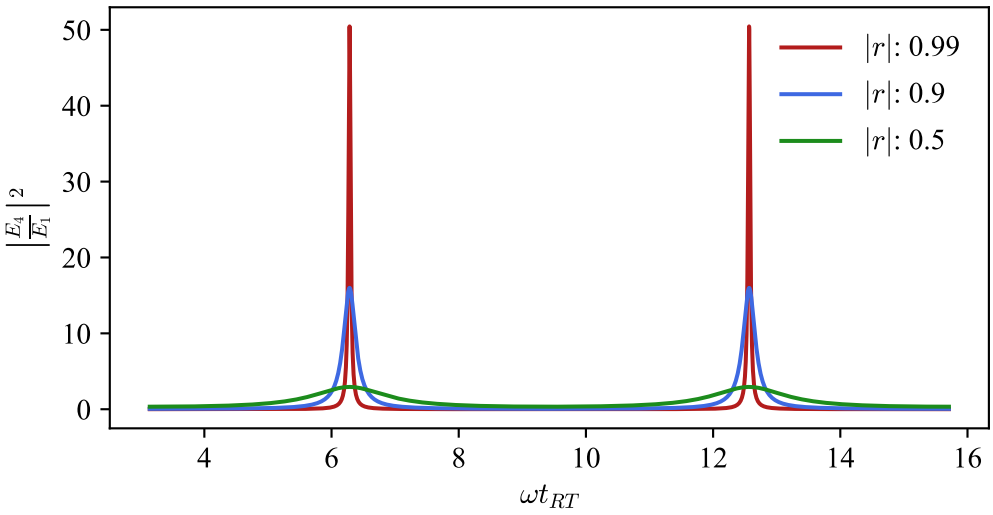

Figure 2.3: Cavity build-up factor for various coupling parameters (round-trip loss $t_{RT}\alpha = 0.01$ and reflected phase shift $\phi_r = 0$). This figure shows the resonant nature of the cavity; for suitable input frequencies, the cavity intensity can far exceed that of the input. The magnitude of this increase, and the range of input frequencies over which it occurs is a function of the coupling parameter (and round-trip losses).

$1 - \frac{x^2}{2}$, which is valid in the vicinity of any resonance with low round-trip losses, which is the case for all devices here studied. These give:

$$\left|\frac{E_4}{E_1}\right|^2 = \frac{|t|^2}{t_{\mathrm{RT}}^2 \left|r\right| e^{-t_{\mathrm{RT}}\alpha}} \frac{1}{\left(\omega - \omega_{\mathrm{n}}\right)^2 + \left(\frac{\gamma}{2}\right)^2}, \tag{2.7}$$

in which ω_{n} is the n^{th} order resonance of the cavity and $\gamma = \frac{2}{t_{\mathrm{RT}}}\left(\left[\left|r\right| e^{-t_{\mathrm{RT}}\alpha}\right]^{-\frac{1}{2}} - \left[\left|r\right| e^{-t_{\mathrm{RT}}\alpha}\right]^{\frac{1}{2}}\right)$, and gives a Lorentzian spectrum for each longitudinal mode.

Linewidth

In Eq. (2.7), γ is the full width at half maximum (FWHM) linewidth of the resonant mode. It is inversely related to the losses in the cavity - both from intrinsic loss (α) and out-coupling ($|t| = \sqrt{1 - |r|^2}$). This linewidth limits the rate at which the cavity can respond to a change in the input field, making it an important parameter for signal processing applications. In particular, it is related to the fractional round-trip losses $L_{\mathrm{RT}} = \left|r\right| e^{-t_{\mathrm{RT}}\alpha}$ by:

$$\gamma = \frac{2}{t_{\mathrm{RT}}} \frac{1 - L_{\mathrm{RT}}}{\sqrt{L_{\mathrm{RT}}}}. \tag{2.8}$$

Decay time

The inverse of the cavity linewidth is the decay time. This is the time constant for the ring-down of the cavity and is given by:

$$\tau_{\mathrm{ph}} = \frac{1}{\gamma}. \tag{2.9}$$

Round-trip time

The other main temporal characteristic of the cavity is its round-trip time, t_{RT}. For a circular resonator of diameter d and refractive index n_0, it is given by:

$$t_{\mathrm{RT}} = \frac{2\pi d n_0}{c}. \tag{2.10}$$

Free spectral range

The free spectral range (FSR) of the cavity is the difference in frequency between adjacent modes, and the inverse of the round-trip time. Accordingly:

$$\begin{aligned} f_{\mathrm{FSR}} &= \frac{1}{t_{\mathrm{RT}}}, \\ &= \frac{c}{\pi d n_0}. \end{aligned} \tag{2.11}$$

$$\omega_{\mathrm{FSR}} = \frac{2c}{d n_0}. \tag{2.12}$$

Finesse

The cavity finesse, F, is the ratio of the free spectral range to the linewidth:

$$F = \frac{\omega_{\mathrm{FSR}}}{\gamma} = \pi \frac{\sqrt{L_{\mathrm{RT}}}}{1 - L_{\mathrm{RT}}}. \tag{2.13}$$

It is a function of only the round-trip losses, high finesse implies low losses, and so is a useful metric to compare resonators of different length.

Q-factor

The Q-factor is the ratio of the resonance frequency and the linewidth, and so gives a sense of the photon lifetime associated with the cavity:

$$Q = \frac{\omega_{\mathrm{n}}}{\gamma} = \omega_{\mathrm{n}} \tau_{\mathrm{ph}}. \tag{2.14}$$

Both the Q-factor and the finesse give a sense of the optical build up associated with a cavity, with the Q-factor being the finesse multiplied by optical frequency then divided by the free-spectral range. Although both the Q-factor and finesse give a metric for the build-up of optical intensity inside of a resonator, their different properties lead to them typically being used in different situations. The Q-factor is related to the photon lifetime of the cavity and so is used when operating speeds are important, whereas the finesse is related to the round-trip losses and so is used for example in free-space cavities which can have variable lengths with minimal associated change to these losses. With the speed of operation being an important factor for many of the devices here studied, typically the Q-factor will be used for the remainder of this work to characterise the resonator losses.

Transmission factor

For the transmission factor - the relationship between the output intensity to the input intensity - a similar method to that used in Eq. (2.6) leads to:

$$\begin{aligned}\left|\frac{E_2}{E_1}\right|^2 &= \frac{|r|^2 + e^{-2\alpha t_{\mathrm{RT}}} - 2|r|\,e^{-\alpha t_{\mathrm{RT}}}\cos(\omega t_{\mathrm{RT}})}{1 + |r|^2\,e^{-2\alpha t_{\mathrm{RT}}} - 2|r|\,e^{-\alpha t_{\mathrm{RT}}}\cos(\omega t_{\mathrm{RT}})}, \\ &= \frac{1}{(\omega-\omega_n)^2 + \left(\frac{\gamma}{2}\right)^2}\left(\frac{|r|}{t_{\mathrm{RT}}^2 e^{\alpha t_{\mathrm{RT}}}} + \frac{e^{-\alpha t_{\mathrm{RT}}}}{t_{\mathrm{RT}}^2\,|r|} - \frac{2}{t_{\mathrm{RT}}^2}\left[1 - \frac{t_{\mathrm{RT}}^2}{2}\{\omega-\omega_{\mathrm{n}}\}^2\right]\right).\end{aligned} \tag{2.15}$$

Example transmission factors for different parameters are plotted in Fig. 2.4.

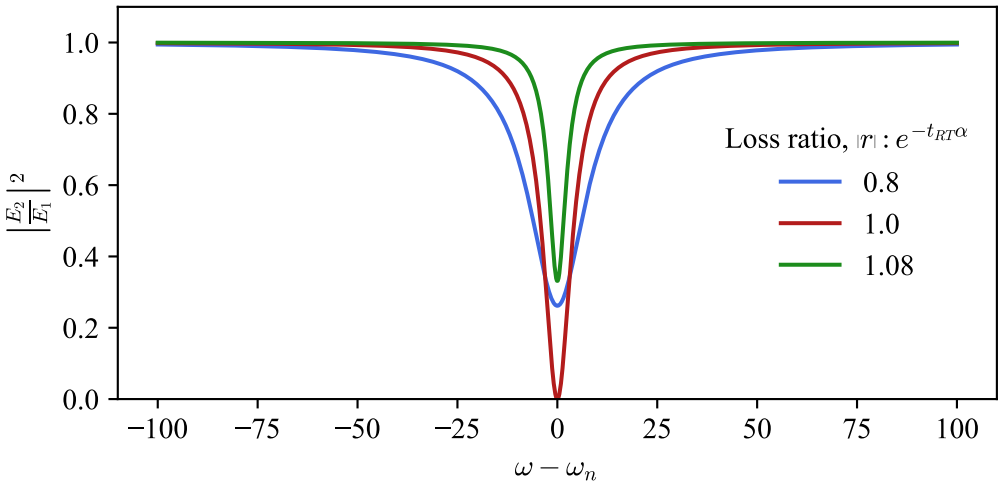

Figure 2.4: Cavity transmission factor across a resonance for different relative values of the coupling loss, $|r|$, and the intrinsic loss, $e^{-t_{RT}\alpha}$ ($e^{-t_{RT}\alpha} = 0.9$, $t_{RT} = 0.05$). For all conditions, the transmission approaches unity far from resonance, with a dip corresponding to resonance. The green curve has the lowest total losses and so has the narrowest dip - under-coupling. When both loss sources are equal in magnitude, the system is critically coupled - the red curve - in which the transmission drops to zero on resonance. Over-coupling happens when the coupling losses exceed the intrinsic losses, blue curve, here the dip is broadest and there is residual transmission on resonance.

Coupling conditions

Equation (2.6) shows that, when the input frequency is resonant with the cavity, the magnitude of the intensity build-up is a function of the round-trip losses $e^{-\alpha t_{\mathrm{RT}}}$ and the coupling parameter $|r|$. Typically, there is little that can be done to reduce round-trip losses of a cavity after its fabrication, but the coupling parameters remain a tool which can be used to maximise device performance (this can be done by moving the coupling waveguide relative to the resonator).

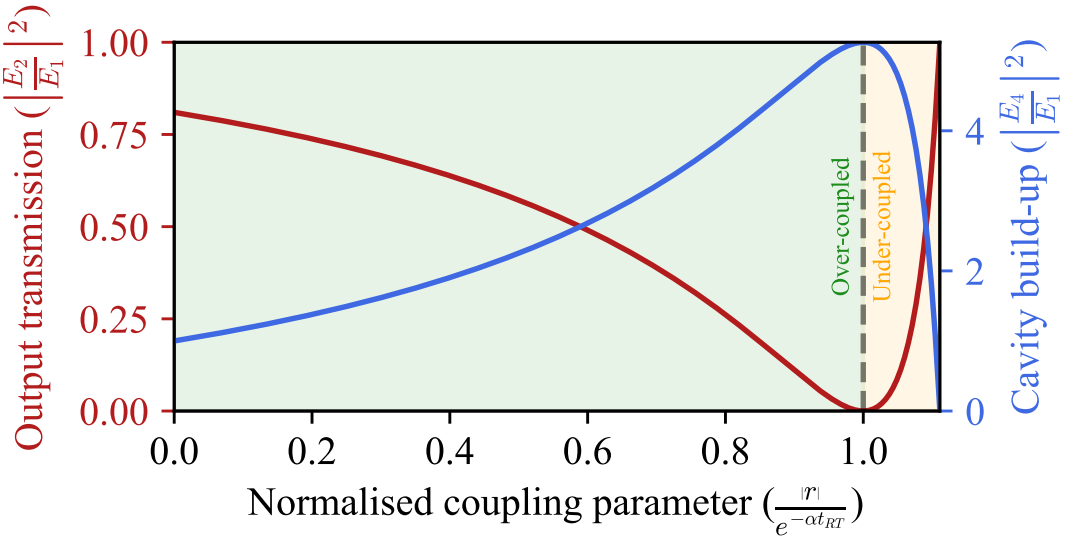

Figure 2.5: Cavity build-up factor (blue) and output transmission (red) for different coupling parameters. The coupling parameter $|r|$ is normalised by the fractional cavity round-trip losses $e^{-\alpha t_{RT}}$ which is here set to 0.9. Critical coupling (dashed black line) is achieved when the coupling parameter equals the round-trip loss. At this point all of the input light couples into the cavity, leading to maximal cavity intensity as the transmission drops to 0. The region to the right of this is said to be under-coupled, and to the left it is over-coupled.

Figure 2.5 shows how the transmission and build-up factors change with different coupling parameters (normalised to the round-trip loss). From this, three distinct coupling regimes can be seen:

Under-coupling (right of dashed line in Fig. 2.5, green line in Fig. 2.4) - when the coupling parameter is below the round-trip loss, the resonator is said to be under-coupled. This regime has the lowest total losses and thus the narrowest linewidth, but the inability for the input to couple into the cavity limits the intra-cavity power.

Critical-coupling (dashed line in Fig. 2.5, red line in Fig. 2.4) - when the coupling parameter equals the round-trip loss, the resonator is said to be critically-coupled. In this condition the out-coupled cavity field completely destructively interferes with the transmitted input field, eliminating all output transmission. Accordingly the intra-cavity intensity is maximal for a critically coupled resonator.

Over-coupled (left of dashed line in Fig. 2.5, blue line in Fig. 2.4) - when the coupling parameter exceeds the round-trip losses, the resonator is said to be over-coupled. This regime has the highest losses thus exhibits the broadest linewidth and an intra-cavity intensity that is smaller than that for critical-coupling. Although these both seem to be detrimental, this regime is useful for signal-processing and quantum photonic applications; broad linewidths allow for the manipulation of faster signals, and the dominance of the coupling parameter over intrinsic losses reduces the rate at which quantum states will be lost to the environment.

The idea of intrinsic loss is valuable when discussing resonator parameters, it describes the resonator as a single system without a coupling waveguide (i.e. $|r| = 0$). The intrinsic loss, due to material absorption and bending losses, gives rise to an intrinsic linewidth γ_0. The actual linewidth is then given by:

$$\gamma = \gamma_0 + \gamma_c, \tag{2.16}$$

where γ_c is the linewidth associated with the effective cavity losses due to coupling. Similarly the cavity Q-factor can be decomposed into intrinsic and coupling Q-factors as:

$$\frac{1}{Q} = \frac{1}{Q_0} + \frac{1}{Q_c}. \tag{2.17}$$

At critical coupling, $\gamma_c = \gamma_0$ (thus $Q_c = Q_0$) and so:

$$\begin{aligned} \gamma_{crit} &= 2\gamma_0, \\ Q_{crit} &= \frac{Q_0}{2}. \end{aligned} \tag{2.18}$$

2.1.4 Add-drop coupling

Thus far we have only considered the cavity field as being a coherent build-up of the pump and we now turn to a technique how to better access the new fields generated inside the cavity. Using a single waveguide coupling as in Fig. 2.2, the output field E_2 is an interference of the cavity field E_3 and the transmitted input E_1. Instead, we can access the cavity field with no interference effects from the residual pump using two waveguides coupled to the cavity (cf. Fig. 2.6) with one waveguide serving as an input and the other serving as an output.

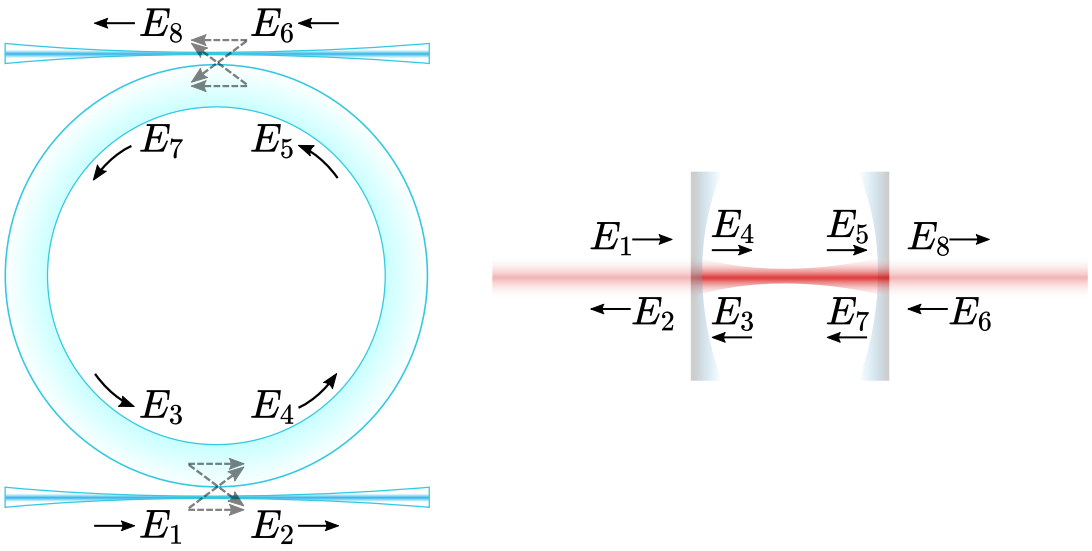

(a) (b)

Figure 2.6: Cavity fields with two coupling locations for a WGM (a) and FP (b) resonator respectively. In this configuration, the intracavity field can be monitored directly via E_8, without any interference with the un-coupled input field E_1 so long as there is no further input at E_6 (N.B. this is not strictly true for quantum optical effects, as a vacuum state input at E_6 will still exhibit quantum fluctuations, but this is beyond the current background discussion).

In this situation, if no light is input to the second waveguide (i.e. $|E_6| = 0$), the output (E_8) is simply a scaled down version of the intracavity field, with no unwanted interference with pump light. Admittedly, this is a simplistic description particularly when considering quantum optics for which there will always be (at minimum) vacuum fluctuations input to this waveguide, but it highlights how a second waveguide can be used to separate the input light from the output.

The fields are once again taken to change slowly in comparison to the round-trip time, with both waveguides coupling, without loss, to the resonator at a point. For the FP resonator in Fig. 2.6b the second mirror is necessarily half a round-trip away from the first, whereas there is some freedom as to the second coupling point's location with respect to the first for the WGM resonator of Fig. 2.6a. This will be assumed to be exactly halfway through the round-trip with negligible bearing on the results of this work. Accordingly, the fields are related by:

$$\begin{aligned}
\begin{bmatrix} E_4 \\ E_2 \end{bmatrix} &= \begin{bmatrix} r_1 & it_1 \\ it_1^* & r_1^* \end{bmatrix} \begin{bmatrix} E_3 \\ E_1 \end{bmatrix}, \\
E_5 &= e^{\frac{t_{\mathrm{RT}}}{2}(-\alpha+i\omega)} E_4, \\
\begin{bmatrix} E_7 \\ E_8 \end{bmatrix} &= \begin{bmatrix} r_2 & it_2 \\ it_2^* & r_2^* \end{bmatrix} \begin{bmatrix} E_5 \\ E_6 \end{bmatrix}, \\
E_3 &= e^{\frac{t_{\mathrm{RT}}}{2}(-\alpha+i\omega)} E_7.
\end{aligned} \tag{2.19}$$

where r_{i} (t_{i}) is now the reflectivity (transmission) for the coupler i which is 1 (2) for the input (output) waveguide. The assumption of lossless coupling sets $|r_{\mathrm{i}}|^2 + |t_{\mathrm{i}}|^2 = 1$. Ensuring that no light is incident to the output waveguide ($E_6 = 0$), the following equations are determined:

$$\begin{aligned}
\frac{E_4}{E_1} &= \frac{it_1}{1 - r_1 r_2 e^{t_{\mathrm{RT}}(-\alpha+i\omega)}}, \\
\frac{E_8}{E_1} &= \frac{-t_1 t_2^* e^{\frac{t_{\mathrm{RT}}}{2}(-\alpha+i\omega)}}{1 - r_1 r_2 e^{t_{\mathrm{RT}}(-\alpha+i\omega)}}, \\
\frac{E_2}{E_1} &= r_1^* - \frac{|t_1|^2 r_2 e^{t_{\mathrm{RT}}(-\alpha+i\omega)}}{1 - r_1 r_2 e^{t_{\mathrm{RT}}(-\alpha+i\omega)}}.
\end{aligned} \tag{2.20}$$

The cavity build-up factor is now:

$$\left|\frac{E_4}{E_1}\right|^2 = \frac{|t_1|^2}{t_{\mathrm{RT}}^2 |r_1| |r_2| e^{-t_{\mathrm{RT}}\alpha}} \frac{1}{(\omega - \omega_{\mathrm{n}})^2 + \left(\frac{\gamma}{2}\right)^2}, \tag{2.21}$$

i.e. it is still a Lorenztian lineshape, though now with a broader linewidth as it is the sum of the intrinsic and now two coupling linewidths ($\gamma = \gamma_0 + \gamma_{\mathrm{c},1} + \gamma_{\mathrm{c},2}$). It is still possible to critically couple to such a cavity to ensure that no power leaves the waveguide through E_2 by setting the linewidth associated with the input waveguide to equal the sum of the intrinsic and output waveguide linewidths ($\gamma_{\mathrm{c},1} = \gamma_0 + \gamma_{\mathrm{c},2}$). However it is not possible to critically couple two waveguides to a cavity simultaneously, as it is not possible to have $\gamma_{\mathrm{c},1} = \gamma_0 + \gamma_{\mathrm{c},2}$ and $\gamma_{\mathrm{c},2} = \gamma_0 + \gamma_{\mathrm{c},1}$ in a physical system that exhibits intrinsic loss.

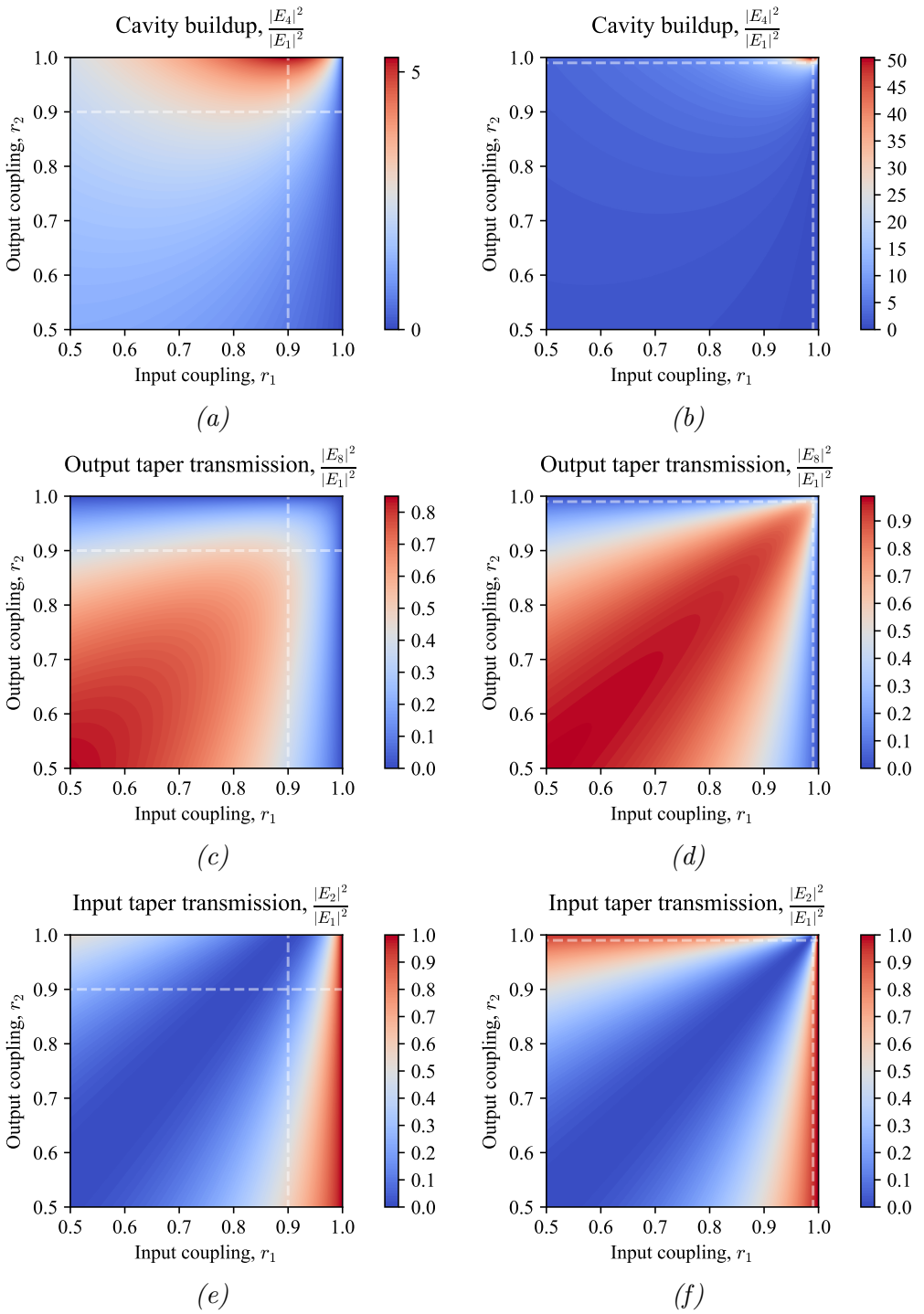

Figure 2.7: Performance associated with different add-drop coupling parameters. The upper row shows the cavity build-up factor, the middle row the output taper transmission, and the lower row the input taper transmission. The left column corresponds to an intrinsic round trip loss of 10%*, with the right corresponding to* 1% *(dashed white lines show the coupling parameters that would correspond to losses equal to this intrinsic loss). These plots show that there may be some compromises required with add-drop coupling, with a competition between the drop port transmission and the associated reduction in cavity build-up.*

This analysis demonstrates some of the compromises that must be considered for applications involving optical resonators for nonlinear and quantum optics; one may wish to have direct access to a cavity field and thus use a second coupling waveguide, however this comes at the expense of either losing critical coupling, or increasing the linewidth and thus reducing the intracavity intensity. Both of these situations reduce the efficiency of the system and so it becomes an important experimental endeavor to balance all outcomes. Fig. 2.7 shows how these performance parameters can change for different coupling conditions, with the top row showing the cavity build-up factor, the middle row showing the relative transmission to the output port, and the lower row showing the (here unwanted) transmission out of the input waveguide. Ideally the top two parameters would be maximised, with the lower one minimised, but there are no coupling conditions that simultaneously allow for this and so compromises must be made when choosing the intended device performance.

Intrinsic resonator losses

The previous discussion showed that the linewidth of a resonance, and thus many associated resonator characteristics, is in part dependent on the intrinsic resonator losses. Such losses give the ultimate limit on the resonator performance, leading to a ceiling of the attainable intensity build-up which sets threshold powers for nonlinear phenomena. Accordingly, a brief discussion on the origins of such losses follows.

Firstly, fused silica was chosen for the material to fabricate all resonators in this study due to its high transparency in the telecoms band. However, in spite of this high transparency, silica still exhibits some residual optical absorption. In particular, it has been shown that adsorption of water into the surface of the silica resonator can lead to excess optical absorption by the presence of OH bonds [40, 41].

Secondly, optical scattering can occur due to surface inhomogeneities [40]. Accordingly, some proportion of the resonator optical mode is coupled into unguided spatial modes, acting as a source of loss. Great care is taken in the fabrication process to ensure all surfaces are smooth, and subsequent handling of the devices done in a clean environment to prevent the accumulation of surface contaminants.

Finally, bending losses are a phenomena well known to the fiber optic community and can be seen in microresonators. In both fiber optics, and WGM resonators, light is guided by total internal reflection at the interface of two materials with contrasting refractive indices. These structures support a travelling wave within the waveguide itself, and lead to the development of an evanescent field at the material interface, which decays exponentially away from the guided mode. In the presence of a bend in a waveguide, one can imagine an effective refractive index that increases linearly from the bend centre to account for the increasing distance the field has to travel. Accordingly, some proportion of the evanescent field will experience a high effective refractive index, and will then couple into this region. This proportion of the field is no longer constrained by the waveguide and radiates away as a form of loss. The magnitude of this effect is mediated by the bend diameter and refractive index contrast in the waveguide (which is high for the silica-air interface exploited in the WGM resonators here studied). Thus, this effect is only appreciable for WGM resonators of diameters $\lessapprox 30\mu m$ [40], which is smaller than any device here studied. Similarly, fiber Fabry-Pérot cavities can have their bending losses reduced to negligible amounts by ensuring there are no tight bends.

2.2 Fabrication methods

Thus far, I have detailed the theory of coupling of light to a resonator and how this leads to a build up of the intensity of the cavity field. But how is this implemented in practice?

This section details the fabrication methods for the main devices used in this work - the micro-toroid and rod WGM resonators - along with those for the tapered fibers used to couple light into them. The Fabry-Pérot cavities used in this work were made using fiber mirrors fabricated by a collaborator, so associated methods will be presented briefly, for the reader's interest.

2.2.1 Micro-toroid

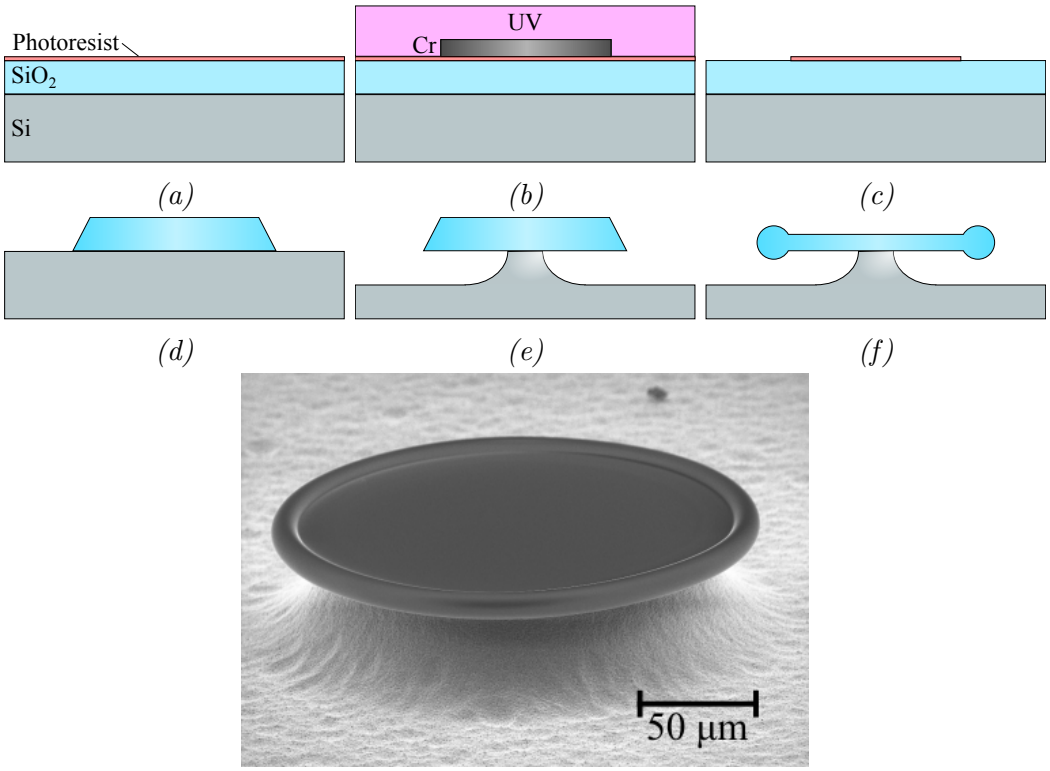

Figure 2.8: Illustration of the fabrication process for a micro-toroid resonator. a) A fused silica-on-silicon wafer is taken and a uniformly thin layer of photoresist is coated on top by spin-coating. b) A disc shape is patterned onto the photoresist using UV lithography and a chromium mask. c) The remaining photoresist is removed in a development process. d) The silica is etched using a BOE (HF acid mixture) which is inhibited by the photoresist disc, leaving a wedge shaped silica disc. e) The underlying silicon is etched away using XeF_2 gas, leaving a silica disc on a silicon pillar. f) A CO_2 laser pulse is used to reflow the disc into a toroidal shape. g) Image of silica-on-silicon micro-toroid resonator fabricated in this method.

The ideal material for making a resonator has to be transparent to minimise losses and a high refractive index is preferred to increase the optical confinement. Although multiple materials can be used as microtoroid cavities, such as lithium niobate and

silicon nitride [42, 43], silica remains a popular choice due to the relative ease of fabrication and high quality factors achievable (despite relatively modest material nonlinearities).

The fabrication process used, similar to the method given in [44], uses a silica-on-silicon chip and a process of lithography, dry etching and reflow to create toroids with exceptionally smooth surfaces and associated high quality factors.

A commercially available silica-on-silicon chip ($2 - 6$ µm thick layer of silica on a 360 µm silicon chip) is taken and deposited with a thin ($\approx$ 1 µm) layer of photoresist by spin-coating which ensures uniform thickness, as shown in Fig. 2.8a). This (positive) photoresist is made from a chemical which becomes soluble to some developer under exposure to UV light (in contrast, a negative photoresist *loses* solubility to a developer under similar exposure).

A mask - a thin layer of chromium patterned with the desired design - is clamped to the top of the photoresist and all is exposed to UV light, Fig. 2.8 b). Due to the mask, only the regions of photoresist that are not directly below chromium will be exposed to UV and become soluble to the developer. After exposure, the mask is removed and the chip is placed in developer to dissolve the exposed photoresist.

The chip is then immersed in a Buffered Oxide Etch (BOE, a HF acid mixture), which then etches the exposed silica away but is inhibited by the photoresist. The BOE acts to slow and control the etching speed of the HF, ensuring the ability to control the process. Figure. 2.8 c) shows the result of this stage, with wedge shaped silica discs sitting atop the silicon chip.

The relatively high refractive index of silicon compared to silica ($n_{\mathrm{Si}} \approx 3.47$, $n_{\mathrm{SiO_2}} \approx 1.45$) means that light would preferentially couple from the silica to the silicon, inhibiting optical confinement. Accordingly, the underlying silicon is dry-etched using xenon diflouride (XeF_2) gas, leaving silica discs atop silicon pillar as shown in Fig. 2.8d).

The final step is to reflow the silica disc to reduce surface roughness. A CO_2 laser pulse is focused, from above, onto the disc. This momentarily melts the edge of the disc, which collapses into a toroidal shape under surface tension and then cools in place, leaving a smooth surface.

This process can be used to make toroids with major diameters ranging from 30 µm to 2 mm, and with Q-factors around 3×10^8, with an example 200 µm diameter micro-toroid shown in Fig. 2.8 f).

2.2.2 Rod resonator

Rod resonators are fabricated in a process using a CO_2 laser lathe, following a method similar to that set out in [45] and illustrated in Fig. 2.9. Rods of optical quality fused silica are bought from commercial suppliers and inserted into a spindle and spun, Fig. 2.9a). A CO_2 laser is focused and directed by computer controlled galvo mirrors onto the upper surface of the spinning rod, with the aid of a visible collinear laser.

The focal point is swept across the upper surface of the spinning rod, with the laser power set to machine away this upper layer, Fig. 2.9b). This stage has multiple purposes: it removes impurities, which are mainly found in the outer region of the silica, gives symmetry about the spindle's rotation axis and machines the rod to the desired diameter. Next, the focal point is swapped between two locations just below

the upper surface, machining two channels into the glass, Fig. 2.9c). These channels are formed by the vaporisation of the glass, due to the extreme intensity of the high power laser at the focus, which then melts the surrounding region, forming a curved surface shown in Fig. 2.9d).

The vaporised glass can stick to the surface of the spinning rod, giving it a milky colour but more importantly leading to large optical losses. To account for this, the steps from Fig. 2.9b) and c) are alternated, with a lower power for step b) to continually remove the build up of impurities.

This process can make rod resonators with (major) diameter between 170 µm-8 mm, and with Q-factors up to 1×10^9. In comparison to micro-toroid fabrication, this process is fast and affords the user better control over the geometric parameters of the resonator. In particular the important geometric parameters are: the diameter of the resonator, which is dependent on the final reflow stage in micro-toroid fabrication (and hard to accurately control), which then sets the resonator FSR. Also the resonator cross section is easier to control for rod resonators, which helps to engineer dispersion (see section 2.3.7). Finally, the larger diameters of rod resonators make them experimentally easier to access from two locations simultaneously, allowing for the add-drop coupling presented in Fig. 2.6. However, in comparison, micro-toroid resonators have smaller associated dimensions which allow for the fabrication of high FSR cavities and, most importantly, have far smaller mode volumes than rods. This concentrates light into a smaller space, leading to higher intensities thus allowing for the realisation of nonlinear effects at lower input powers. Whilst rods may be more appropriate in a research laboratory setting due to their ease of implementation, micro-toroids are more likely to be integrated into future photonic technologies.

2.2.3 WGM fabrication requirements

With silica chosen as the material for the resonator due to its high transparency in the telecom band and its ease of fabrication, there remain two major aims for the fabrication process: ensuring a smooth surface, and achieving a diameter such that the resonator has the desired FSR.

As described above for both the micro-toroid and rod resonator geometries, a CO_2 laser is used to ensure smooth surfaces. This is achieved by reflowing the surface: melting it for a short amount of time during which surface tension pulls it into a smooth and regular shape. This ensures that all surface roughness features are on a length scale much smaller than the optical wavelength, ensuring that scattering losses are minimised.

Chapters 3 & 4 concern the dynamics of degenerate optical modes of the same longitudinal mode number and so do not have any requirements on the resonator FSR, and thus its diameter. Chapter 6, however, describes the generation of photons into spectral modes that can be separated by a dense wavelength division multiplexer (DWDM). DWDMs are commercial devices with channels at frequencies specified by international standards, each separated by 100 GHz. Thus, according to Eq. 2.11, to match the resonator FSR to the DWDM spacing, its diameter must be 660 µm. The tolerance to this value is set by the DWDM channel bandwidth (typically 10GHz) and the number of modal pairs required to be separated. For five modal pairs, a diameter of 660 ± 12 µm is required. Such precision is within that available from the WGM fabrication methods previously described.

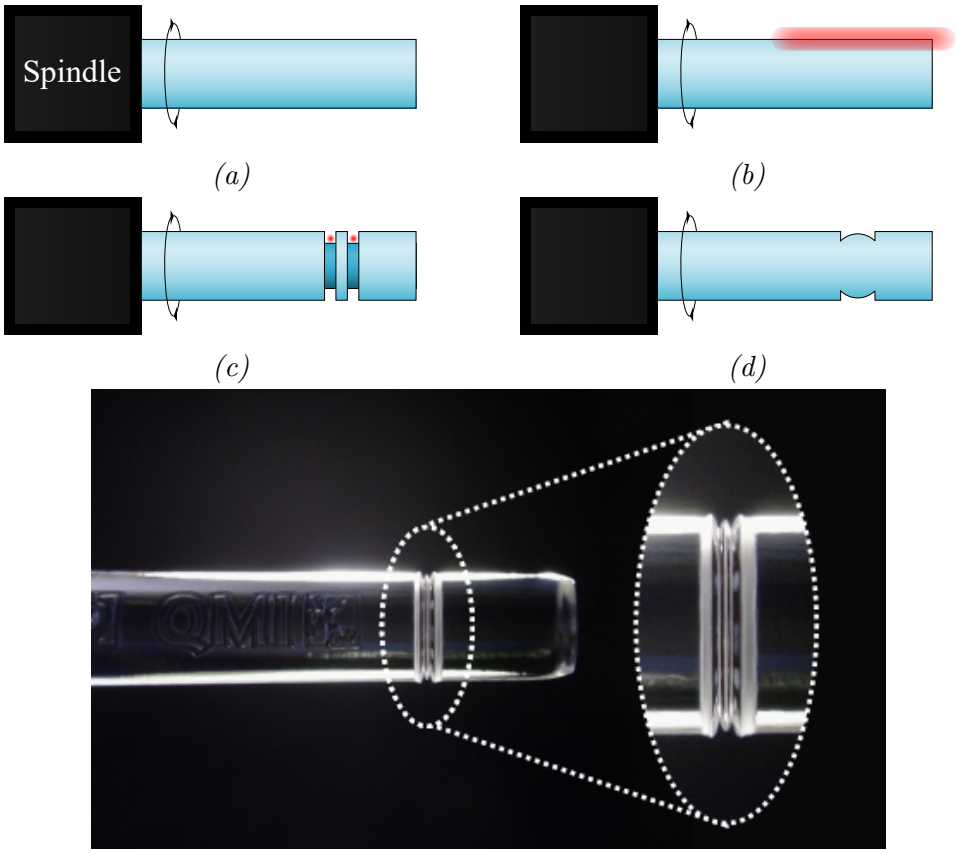

Figure 2.9: Illustration of the fabrication process for a rod resonator using a CO_2 laser lathe. a) A length of fused silica rod is spun in a spindle. b) The outer layers of the rod are removed by scanning the focal point of a CO_2 laser beam over the top surface. c) The beam is focused onto two spots to dig two channels into the spinning rod. d) The laser is scanned over the machined region, softening the silica which reforms into a smooth shape. e) Image of a rod resonator fabricated using this method.

2.2.4 Tapered fiber

In order to couple light into, and out of, these high-Q resonators without excessive interference with the cavity fields, the evanescent field is exploited. As electromagnetic waves propagate around a WGM resonator via total internal reflection, it would initially appear that there is a discontinuous jump in the electric and/or magnetic field at the resonator-air interface. Of course this can not happen and is prevented by the development of an evanescent field in the region - an oscillating EM field that matches the cavity field at the resonator boundary but then exponentially reduces further away such that there is no associated propagation (N.B. this is not *strictly* true as for a curved interface some proportion of the evanescent field will radiate away and is termed a "bending loss", which sets a maximum curvature - and so minimum diameter - of WGM resonators).

Accordingly, one can use the evanescent field of another device which guides light via total internal reflection to excite the evanescent field of the cavity. This leads to the coupling between the field input to the device and the cavity field, with

some proportion propagating around the WGM resonator. Three main methods have been used for this:

- *Prisms.* These can have very strong evanescent fields and associated coupling to WGM resonators, but are large and require free-space optics making them less easy to use [46].

- *Waveguides.* On-chip WGM resonators can couple to waveguides made using the same lithographic techniques. This mechanically robust technique is undoubtedly the most promising method for implementation in photonic technologies, but can be inflexible in a research setting as there can be no changes post-fabrication [47].

- *Tapered fibers.* Tapering an optical fiber can allow the evanescent field to be accessible from its surface, giving a coupling device that is easy to send light through and flexible in positioning making it useful for research purposes, albeit with a fragility that makes it difficult to be used outside of a laboratory environment [48].

In this work, tapered fibers were used as the coupling device due to their versatility. In particular, the ability to change the coupling position in three dimensions was found to be useful - the vertical position of the taper with respect to the WGM plane determining the spatial mode of the resonator being excited; the axial position of the taper determining its diameter at the coupling location and hence the phase matching between the taper and cavity fields; and finally the distance between the taper and WGM resonator giving a control for the degree of coupling between the taper and cavity fields (i.e. under-, critically- or over-coupled). Moreover, the ability to avoid free-space optics and simply have all fields inside of fibers and commercially available fiber components simplifies experimental setups significantly.

The principle for the tapered fiber fabrication process is simple (though in practice it is often not!), and is illustrated in Fig. 2.10. A standard, single mode fiber ($\approx$ 10 µm diameter core, 125 µm diameter cladding) is taken, and the protective plastic coating is removed over a $\approx$ 10 mm length. This exposed region is clamped in place above a hydrogen nozzle, Fig. 2.10a), and a laser is sent through it to a photodiode (PD) to monitor transmission.

Hydrogen is then pumped through the nozzle and ignited, creating a flame positioned such that the hottest part is on the fiber. The fiber clamps are then moved slowly away from each other using two computer controlled translation stages, adding tension to the hot fiber which draws the central region into a taper as shown in Fig. 2.10b).

In a normal fiber, the higher-index core guides light due to total internal reflection at the core-cladding interface. However, during tapering, the diameters of both cladding and core reduce and the light is no longer fully guided by the core with the fiber now becoming multi-modal and shows a complex interference pattern in transmission, see Fig. 2.10c). Eventually the cladding becomes so narrow that light is guided through the cladding-air interface, and the fiber becomes once more single mode. Due to the higher index contrast between the cladding and air, relative to that between the core and the cladding, this happens for a relatively narrow taper of $\approx$ 1 µm.

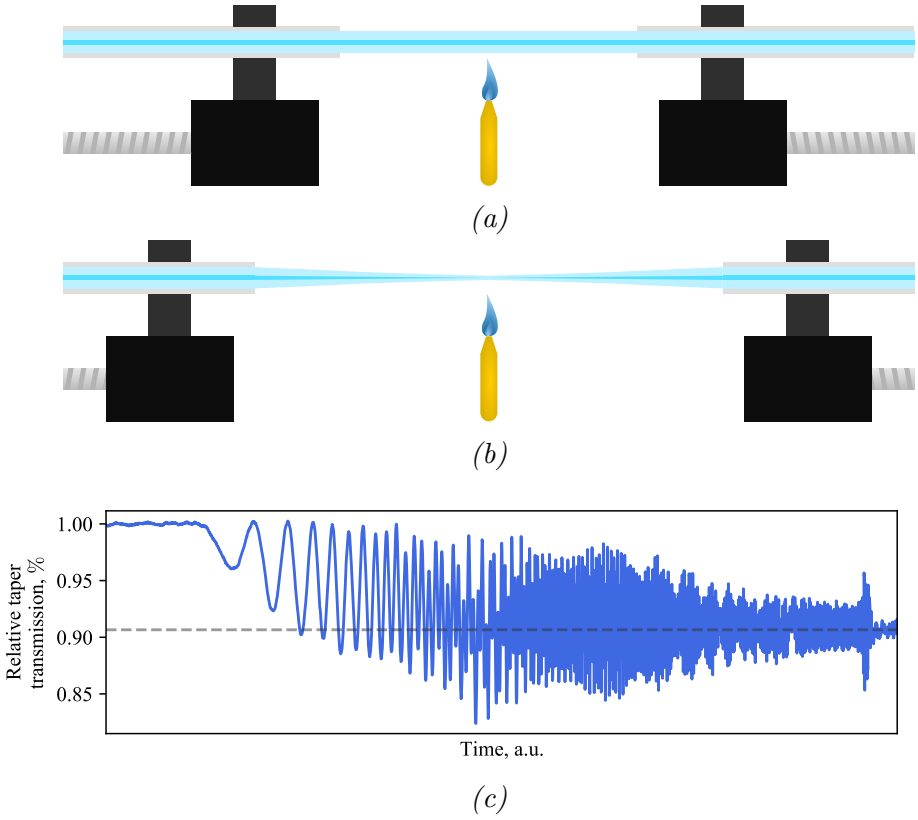

Figure 2.10: Illustration of the fabrication process for a tapered optical fibre. a) The plastic coating over a length of optical fibre is removed and clamped onto translation stages above a hydrogen flame. b) The translation stages slowly move apart from each other, leading to a taper with a sub-micron waist. c) The transmission through a fiber during tapering. The ordinarily single mode fiber becomes multi-modal as the light is guided by both the core and cladding as their diameters reduce exhibiting the complex interference shown. Eventually the taper becomes so narrow that the light is guided by the cladding-air interface and the taper becomes once again single mode, which is indicated by a dramatic reduction in the amplitude of the oscillations in transmissions following a short increase in these amplitudes, shown at the right of the image.

The flame is then removed, with a small amount of tension applied to the taper to counter any thermal relaxation, and it is glued onto a bracket. The fiber ends are then spliced onto commercially available fiber pigtails to be connected to photonics circuits as required.

Subsequent handling of tapered fibers requires great care to protect them from breaking. Although glued onto a bracket, having a sub-micron waist means that vibrations or gently touching another object can break them. This can be a particular issue when coupling light from the taper into a resonator as they need to be very close for their respective evanescent fields to overlap. On a similar note, the exposed evanescent fields of a tapered fiber mean that surface contaminants (e.g. dust) can easily lead to scattering. This prevents meaningful transmission from the taper to the resonator and it is thus important to maintain them in a clean environment which can be done using an enclosure with a positive pressure to reduce the likelihood of dust entering. Despite these issues, the versatility of operation afforded

by the ease at which tapered fibers can be manoeuvred, along with the fact they are intrinsically fiber-coupled, give a useful experimental tool.

2.2.5 Fiber mirrors

For fiber Fabry-Pérot cavities, coupling is much simpler. When the cavity is made of optical fiber itself, mirrors can be deposited directly onto the ferrule connectors at the fiber ends, with input/output coupling attained by merely connecting other fibers to these ferrules. These fiber mirrors were made by a collaborator using a technique called sputtering.

Sputtering allows for individual layers of material to be grown onto a surface with very precise thicknesses. This allows for the fabrication of Bragg mirrors - alternating layers with differing refractive index and very well defined thickness - to be fabricated on the ends of fibers. These mirrors, made from layers of tantalum pentoxide (Ta_2O_5) and silica (SiO_2) can have reflectivities well above 99% (up to 99.9% is feasible!).

A fiber Fabry-Pérot cavity, which was first introduced in Ref [38], is then made by simply attaching two such mirrors to either end of a given fiber. As optical fibers exhibit low loss, it is possible to make such cavities longer with minimal addition to the round-trip loss, increasing the net nonlinearity exhibited by the cavity for a given input power.

2.3 Nonlinear optics

This section details the emergence of the nonlinear optical effects that underpin the phenomena studied in this work, in particular those of the third order nonlinearity: the optical Kerr effect. The first half of this thesis relies on the intensity dependent refractive index that the Kerr effect manifests leading to self- and cross-phase modulation (SPM and XPM). In particular, the difference in magnitude between SPM and XPM [49] is of vital importance for understanding Chapters 3 and 4 and so is derived in this section. Finally the process of four-wave mixing (FWM) is discussed as a manifestation of the Kerr-effect in which light coherently couples to other frequency modes. This process is here treated classically, and will be quantised in Chapter 5 to show how it can yield states interesting for a variety of proposed quantum technologies.

2.3.1 Maxwell's Equations

All classical optics can be described using Maxwell's equations:

$$\nabla \cdot \boldsymbol{D} = \rho_{\mathrm{f}}, \tag{2.22}$$

$$\nabla \cdot \boldsymbol{B} = 0, \tag{2.23}$$

$$\nabla \times \boldsymbol{E} = -\frac{\partial \boldsymbol{B}}{\partial t}, \tag{2.24}$$

$$\nabla \times \boldsymbol{B} = \mu_0 \left(\boldsymbol{J}_{\mathrm{f}} + \frac{\partial \boldsymbol{D}}{\partial t} \right), \tag{2.25}$$

in which $\boldsymbol{D} = \epsilon_0 \boldsymbol{E} + \boldsymbol{P}$ is the electric displacement vector - the sum of the electric field $\boldsymbol{E}$ multiplied by the permittivity of free space ϵ_0 and the electric dipole moment

density $\boldsymbol{P}$, ρ_{f} is the density of free charge carriers (taken to be zero), $\boldsymbol{B}$ is the magnetic field, μ_0 is the permeability of free space and $\boldsymbol{J}_{\mathrm{f}}$ is the free current density (taken to be zero). Eqs. (2.24)-(2.25) together give:

$$\nabla \times \nabla \times \boldsymbol{E} + \frac{1}{c^2}\frac{\partial^2}{\partial t^2}\boldsymbol{E} = -\mu_0 \frac{\partial^2}{\partial t^2}\boldsymbol{P}, \tag{2.26}$$

which with the identity $\nabla \times \nabla \times \boldsymbol{E} = \nabla\left(\nabla \cdot \boldsymbol{E}\right) - \nabla^2 \boldsymbol{E}$ and Eq. (2.22) (assuming $\nabla \cdot \boldsymbol{D} \approx \nabla \cdot \boldsymbol{E} = 0$) gives:

$$\nabla^2 \boldsymbol{E} - \frac{1}{c^2}\frac{\partial^2}{\partial t^2}\boldsymbol{E} = \mu_0 \frac{\partial^2}{\partial t^2}\boldsymbol{P}. \tag{2.27}$$

This is a wave equation for $\boldsymbol{E}$ in which $\boldsymbol{P}$ is a driving term. However, the dipoles are induced by the electric field and so Eq. (2.27) can be expressed in terms of the single field $\boldsymbol{E}$.

2.3.2 Electric dipole moment density, $\boldsymbol{P}$

The electric dipole moment density $\boldsymbol{P}$ is an important parameter, describing parametric light-matter interactions. An oscillating electric field passing through a medium induces oscillating electric dipole moments, which in turn radiate light. It is for this reason that $\boldsymbol{P}$ appears as a driving term in Eq. (2.27), and it can be given as a Taylor expansion in terms of $\boldsymbol{E}$:

$$\boldsymbol{P} = \epsilon_0 \left(\chi^{(1)}\boldsymbol{E} + \chi^{(2)}\boldsymbol{E}^2 + \chi^{(3)}\boldsymbol{E}^3 + \ldots\right), \tag{2.28}$$

in which $\chi^{(N)}$ is the N-th order susceptibility - a tensor of rank $N+1$ with, in general, 3^{N+1} components each of which is dependent on the frequency of the electric field oscillations. For optically isotropic media, such as fused silica, the polarisation dependence of the susceptibility tensor is lost simplifying the situation greatly. Moreover, all parameters of $\chi^{(2)}$ equal zero for media which exhibit such (inversion) symmetries, and so only $\chi^{(3)}$ nonlinearities are observed (higher order effects are negligible due to the extreme intensity requirements due to the very small contributions from higher order susceptibility tensors).

2.3.3 Linear Optics

For isotropic media, the $\chi^{(1)}$ susceptibility loses its tensor nature, becoming simply a number. Ignoring nonlinear phenomena, Eq. (2.27) becomes:

$$\begin{aligned}
\nabla^2 \boldsymbol{E} - \frac{1}{c^2}\frac{\partial^2}{\partial t^2}\boldsymbol{E} &= \mu_0 \epsilon_0 \chi^{(1)} \frac{\partial^2}{\partial t^2}\boldsymbol{E}, \\
\nabla^2 \boldsymbol{E} - \frac{1+\chi^{(1)}}{c^2}\frac{\partial^2}{\partial t^2}\boldsymbol{E} &= 0, \\
\nabla^2 \boldsymbol{E} - \left(\frac{n_1}{c}\right)^2 \frac{\partial^2}{\partial t^2}\boldsymbol{E} &= 0,
\end{aligned} \tag{2.29}$$

which is simply a wave equation in which light is slowed by a factor $n_1 = \sqrt{1+\chi^{(1)}}$ - the refractive index of the material.

2.3.4 The second-order susceptibility, $\chi^{(2)}$

The second-order susceptibility is the lowest order nonlinearity and is the source of the electro-optic Pockels effect, second harmonic generation (SHG) and spontaneous parametric down conversion (SPDC) - a common source of entangled photon pair generation [25, 50, 51].

Centrosymmetric media, such as silica, have no such nonlinearity and so none of the aforementioned effects are present in the resonators that are studied in this work.

2.3.5 The third-order susceptibility, $\chi^{(3)}$

The third-order susceptibility - the source of the Kerr-effect - is a fourth-rank tensor, with elements $\chi^{(3)}_{\mathrm{i,j,k,l}}$ for which the indices $i, j, k, l \in \{1, 2, 3\}$ represent the three spatial dimensions. In general each of the associated 81 elements are unique, but the spatial symmetries of isotropic media reduce these dramatically to only three independent parameters from which all others can be derived:

$$\chi^{(3)}_{\mathrm{i,j,k,l}} = \chi^{(3)}_{1,1,2,2}\delta_{\mathrm{i,j}}\delta_{\mathrm{k,l}} + \chi^{(3)}_{1,2,1,2}\delta_{\mathrm{i,k}}\delta_{\mathrm{j,l}} + \chi^{(3)}_{1,2,2,1}\delta_{\mathrm{i,l}}\delta_{\mathrm{j,k}}, \tag{2.30}$$

which holds for arbitrary field frequencies [25]. The associated (nonlinear) dipole moment density is:

$$P_i^{(3)}\left(\omega_{\mathrm{a}} + \omega_{\mathrm{b}} + \omega_{\mathrm{c}}\right) = \epsilon_0 \sum_{\mathrm{a,b,c}} \sum_{\mathrm{j,k,l}} \chi^{(3)}_{\mathrm{i,j,k,l}}\left(\omega_{\mathrm{a}} + \omega_{\mathrm{b}} + \omega_{\mathrm{c}}; \omega_{\mathrm{a}}, \omega_{\mathrm{b}}, \omega_{\mathrm{c}}\right) E_{\mathrm{j}}\left(\omega_{\mathrm{a}}\right) E_{\mathrm{l}}\left(\omega_{\mathrm{b}}\right) E_{\mathrm{k}}\left(\omega_{\mathrm{c}}\right), \tag{2.31}$$

in which the indices a,b,c allow for the nonlinear coupling of different frequency components of the light subject to conservation of energy, in a process known as four-wave mixing (FWM).

2.3.6 The intensity-dependent refractive index

A special case of Eq. (2.31) occurs when $\omega_{\mathrm{a}} = \omega_{\mathrm{b}} = -\omega_{\mathrm{c}} = \omega$. Here:

$$\begin{aligned} P^{(3)}_{\mathrm{i}}\left(\omega\right) &= \epsilon_0 \sum_{\mathrm{j,k,l}} \chi^{(3)}_{\mathrm{i,j,k,l}}\left(\omega; \omega, \omega, -\omega\right) E_{\mathrm{j}}\left(\omega\right) E_{\mathrm{l}}\left(\omega\right) E_{\mathrm{k}}\left(-\omega\right), \\ &= 6\epsilon_0 \chi^{(3)}_{1,1,2,2}\left(\boldsymbol{E}\cdot\boldsymbol{E}^*\right) E_{\mathrm{i}} + 3\epsilon_0 \chi^{(3)}_{1,2,2,1}\left(\boldsymbol{E}\cdot\boldsymbol{E}\right) E^*_{\mathrm{i}}, \end{aligned} \tag{2.32}$$

where the latter step comes from the intrinsic permutation symmetry of the susceptibility tensor. This can be expressed as:

$$\boldsymbol{P}^{(3)} = 3\epsilon_0 \chi^{(3)}\left(2\left(\boldsymbol{E}\cdot\boldsymbol{E}^*\right)\boldsymbol{E} + \left(\boldsymbol{E}\cdot\boldsymbol{E}\right)\boldsymbol{E}^*\right), \tag{2.33}$$

which has been simplified by $\chi^{(3)}_{1,1,2,2} = \chi^{(3)}_{1,2,2,1} = \chi^{(3)}$ which holds for materials in which the nonlinearity is dominated by the non-resonant response of bound electrons, as is the case for silica [25, 49]. In the circular polarisation basis, i.e. $\boldsymbol{E} = E_+\boldsymbol{\sigma}_+ + E_-\boldsymbol{\sigma}_-$ where $\boldsymbol{\sigma}_\pm$ are the basis vectors for circular polarised light of opposite handedness (such that $\boldsymbol{\sigma}^*_\pm = \boldsymbol{\sigma}_\mp$, $\boldsymbol{\sigma}_\pm \cdot \boldsymbol{\sigma}_\mp = 1$, $\boldsymbol{\sigma}_\pm \cdot \boldsymbol{\sigma}_\pm = 0$), this becomes [52]:

$$P^{(3)}_\pm = 6\epsilon_0 \chi^{(3)}\left(\left|E_\pm\right|^2 + 2\left|E_\mp\right|^2\right) E_\pm. \tag{2.34}$$

This now has the same apparent form as the linear term in Eq. (2.29) and indeed has the same effect - it leads to a change in the apparent refractive index of the material though with a magnitude that is dependent on the intensity of the field.

This nonlinear refractive index arises from two processes: self-phase modulation (SPM), in which the intensity of a circular polarisation affects the refractive index experienced by the same handedness, and cross-phase modulation (XPM) in which the refractive index experienced by the opposite handedness is affected. The difference in magnitude of these effects - XPM has a factor of two in comparison to SPM - means that these two components can experience different effective refractive indices (with the less intense component experiencing a greater shift due to the greater magnitude of XPM) [25, 53].

This conclusion - that light can be broken down into components that experience different refractive indices - is the underlying phenomenon responsible for the interesting effects I demonstrate in Chapters 3 & 4, hence why it has here been discussed in detail.

2.3.7 Four-wave mixing

The frequency mixing available from Eq. (2.31) allows for the generation of light in different frequency modes (i.e. those with the same transverse spatial structure, but differing longitudinal mode numbers) inside the resonator by FWM. Here, two pump photons are annihilated and simultaneously a pair of photons - termed the signal and idler pair, in which the signal (idler) has a higher (lower) frequency than the pump - are created with frequencies according to the conservation of energy [54].

Figure 2.11 illustrates the two manners in which FWM can occur. *Degenerate* FWM (2.11a) occurs when two pump photons of the same frequency are annihilated, generating photons in modes equidistant about the pump mode in frequency. *Non-Degenerate* FWM (2.11b) occurs when two pump photons of different frequency are annihilated, generating photons in modes equidistant about the *mean* pump photon frequency.

Importantly in both of these situations, the generated photons are centred in frequency about the pump. This is in contrast to the $\chi^{(2)}$ effects of parametric down-conversion or second-harmonic generation in which the frequencies of the modes involved differ significantly. FWM allows all fields to be of a similar frequency (e.g. all in the telecom band) allowing for the easy integration with existing devices - a valuable property for photonic/quantum technologies. The $\chi^{(3)}$ effects of third-order down-conversion or third-harmonic generation also suffer from this large frequency contrast between pump and generated fields and will be disregarded for the remainder of this work for this reason.

For a weak pump, the rate at which signal/idler photons are generated is less than the rate at which photons dissipate from their respective modes. In this situation - called *spontaneous*-FWM - a two-mode squeezed vacuum state is generated [53] for which the detection of a single photon in the signal (idler) mode can be used to herald a single photon in the idler (signal). For higher pump powers, the parametric gain exceeds the losses, and lasing occurs in the signal/idler modes. In this case, the underlying quantum nature of the system leads to quantum correlations between the modes. Both of these circumstances - heralded photon sources and multi-modal quantum correlations - are a useful resource for a wide range of quantum technologies

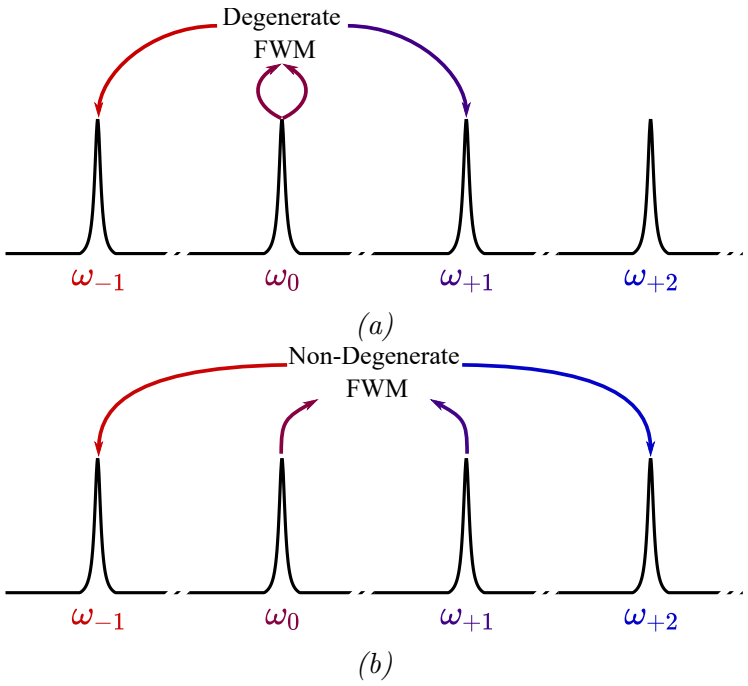

Figure 2.11: Illustration of four-wave mixing (FWM). a) Degenerate FWM. For a suitably intense cavity field in the pumped mode ω_0, two pump photons can annihilate generating a pair of photons, one with a higher (lower) frequency, called the signal (idler), which are separated in frequency from the pump by an integer number of FSR. The frequency selective nature of the cavity, along with conservation of energy ensures that this is effect is only significant for equidistant modes about the pump, $\omega_{\pm N}$. b) Non-degenerate FWM. When two cavity modes have suitably intense fields, a photon from each field can annihilate, generating photons in the modes that correspond to the same total energy (i.e. $\omega_0 + \omega_{+1} = \omega_{-1} + \omega_{+2}$).

[55] and will be discussed in Chapters 5 & 6.

Phase matching

Momentum, along with energy, must be conserved between the annihilated and generated photon pairs. For nonlinear optics, this requirement is more often referred to as phase matching which simply means that there should be a (near) constant phase difference between all beams to maximise the parametric conversion efficiency.

There is an intuitive picture for phase matching for degenerate FWM in an optical resonator: the generated signal and idler photons must be equidistant in frequency about the pump, but there must also be optical modes at both of these frequencies to allow for the generated light to be guided inside the resonator. As shown in Fig. 2.12, this is necessarily true for a resonator with zero dispersion, but the lowering (raising) of the frequency of the signal/idler optical modes relative to the pump mode due to normal (anomalous) dispersion can inhibit this. Such chromatic dispersion is present in all materials and resonator geometries (although perhaps only at higher orders), and this ultimately limits the spectral region for which efficient FWM can occur in optical resonators, hence dispersion engineering has been a subject of substantial research [56].

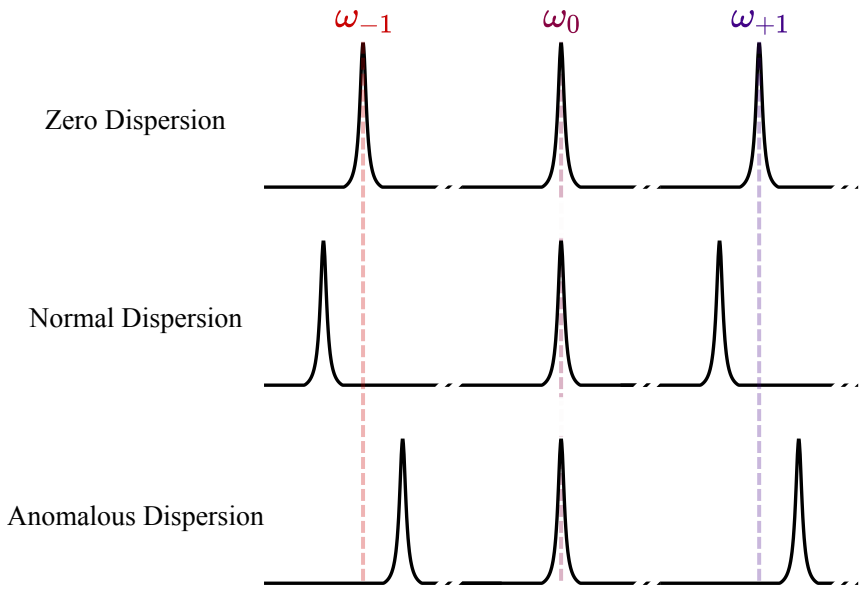

Figure 2.12: Effects of dispersion on the cavity resonances about pump mode. For zero dispersion, adjacent resonances are equidistant in frequency about the pump mode. Normal dispersion shifts these resonances to lower frequencies with respect to the pump mode, whereas anomalous dispersion shifts them to higher frequencies, both breaking the equidistance in frequency from the pump.

Frequency combs and optical solitons

Cascaded FWM, where a new tone then can lead to complex nonlinear dynamics featuring many modes, all equidistant in frequency, that can become mutually phase locked - a phenomena called *frequency combs* [57]. For suitable pump powers and detunings (defined as the difference between the laser and cavity resonance frequencies), this can lead to dissipative Kerr solitons (DKS) - a sequence of narrow bright pulses with a repetition rate equal to the FSR of the cavity [58].

Cross phase modulation between different frequency modes, rather than between different polarisation modes as previously discussed, can balance dispersion in this regime. Those generated sidebands have a greater shift in their refractive index due to XPM from the strong pump, which has the same effective outcome as normal dispersion in Fig. 2.12. This effect can balance out intrinsic anomalous dispersion in the resonator, giving a very wide range in frequency for which phase matching is satisfied.

DKS can manifest when there is a twofold balance - one between nonlinearity and dispersion as described, and another between resonator losses and parametric gain - which lead to a pulse with a squared hyperbolic-secant spectrum.

2.3.8 The Lugiato-Lefever Equation

The Lugiato-Lefever Equation (LLE) was developed to describe the evolution of the field inside a nonlinear cavity that is pumped by a monochromatic coherent field. Initially this work assumed a longitudinally uniform field, with the self-focusing Kerr-effect counterbalancing diffraction, leading to stable, nontrivial transverse spatial structure in the beam [59]. This work was then developed to describe longitudinal (and hence temporal) structure in ring cavities, with diffraction replaced by

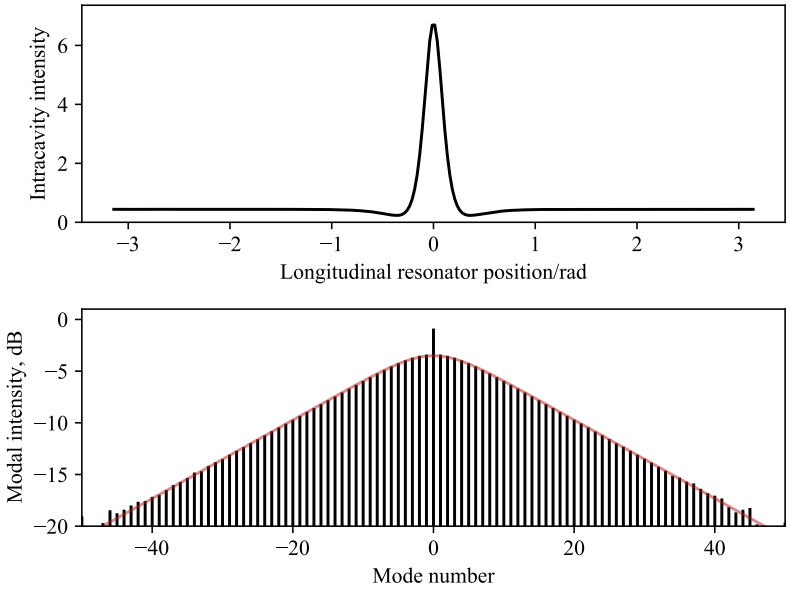

Figure 2.13: Dissipative Kerr Soliton (DKS) profile. A DKS is a bright pulse amongst a dark background when seen in time or as a function of the longitudinal position around the resonator (above). In frequency space (below), there is a strong pump mode which excites high intensities in its nearest neighbours which drops off exponentially as a hyperbolic secant profile (red line).

dispersion in this context [60]. The LLE is given using the following notation in Ref [53]:

$$\frac{\partial E}{\partial t} = -\frac{1}{2}\delta\omega_{\text{tot}}E + i\Delta E + ig_0\left|E\right|^2 E + \frac{i\eta_2}{2}\frac{\partial^2 E}{\partial\theta^2} + \sqrt{\delta\omega_{\text{ext}}}E_{\text{in}}, \tag{2.35}$$

in which E is the cavity field envelope; E_{in} is the input field; $\delta\omega_{\text{tot}}$ and $\delta\omega_{\text{ext}}$ are the linewidths associated with the whole system and external coupling respectively; Δ is the detuning (difference between the laser and cavity frequencies); g_0 gives the strength of the Kerr effect; η_2 is the second-order dispersion of the cavity; t is time; and θ gives the azimuthal angle around the resonator.

Normalising Eq. (2.35) gives a simpler dimensionless model, with the following form being what is meant by the term LLE for the rest of this work unless explicitly stated otherwise:

$$\frac{\partial\psi}{\partial\tau} = -\left(1 + i\alpha\right)\psi + i\left|\psi\right|^2\psi - \frac{i\beta}{2}\frac{\partial^2\psi}{\partial\theta^2} + F, \tag{2.36}$$

where the dimensionless cavity field $\psi\left(\tau,\theta\right) = \sqrt{{2g_0}/{\delta\omega_{\text{tot}}}}E$, dimensionless time $\tau = {t}/{2\tau_{\text{ph}}}$, dimensionless detuning $\alpha = {-2\Delta}/{\delta\omega_{\text{tot}}}$, dimensionless dispersion $\beta = {-2\eta_2}/{\delta\omega_{\text{tot}}}$ and dimensionless input field $F = \sqrt{{8g_0\delta\omega_{\text{ext}}}/{\delta\omega_{\text{tot}}^3}}\sqrt{{P_{\text{in}}}/{\hbar\omega}}$.

Modified versions of the LLE accurately model all effects studied in this work. The interaction of orthogonally polarised light in ring resonators was studied in Ref [61], which showed that the Kerr-effect can lead to a nonlinear coupling of polarisation modes via cross phase modulation. Together with Refs [62, 63], which

develops the LLE for Fabry-Pérot, rather than ring, cavities a model for the interaction of orthogonally polarised light in a fiber Fabry-Pérot resonator can be developed[1]. This model is used, for uniform cavity fields, in Chapter 3 to develop a set of coupled nonlinear equations which accurately predict the spontaneous symmetry breaking of the polarisation of light in a fiber Fabry-Pérot cavity.

In Chapter 4, two lots of Eq. 2.36 are used to describe the nonlinear interaction of counter-propagating light in a ring resonator. Again, the fast dynamics in these equations are ignored by assuming uniform cavity fields, and the nonlinear term is expanded as per Eq. 2.34 to account for the cross phase modulation each mode experiences due to the other.

Finally, Chapter 5 follows the method of Ref [53] to quantise the LLE. This set of equations are linearised and manipulated to explore the entanglement between modal pairs, requiring a numerical solution to the LLE in the process.

Numerical solution of the LLE

The LLE does not have a general analytic solution, but can be solved numerically using a "split-step Fourier" method [64]. Direct integration of Eq. (2.36) is computationally inefficient for the simulation of many modes, but can be simplified by splitting the evolution into two independent steps. The first step, including the dispersive and detuning terms can be solved efficiently in frequency-space after the Fourier transform of ψ, as they both manifest as a complex detuning for each mode in this space. This solution is then inverse-Fourier transformed and updated in time with additions from the nonlinear and pump terms. This algorithm is detailed further in Appendix A.

2.3.9 Modal spectra

As shown in Eq. (2.7), under simplifying assumptions, the spectrum of a high-Q mode should be a Lorentzian line-shape, though these breakdown when nonlinear effects are considered. Fig. 2.14 shows both the theoretically predicted, and experimentally observed, modal spectra. Lorentzian profiles are expected and observed for low input powers - see Fig. 2.14a,b) - at higher powers the spectrum becomes triangular shaped - Fig. 2.14c,d).

The nonlinearities that are not present in the simplified model *are* present in the LLE. Figure 2.14 shows how the LLE precisely matches experiment in describing both the modal spectra and frequency comb generation. The first three rows of the figure show comparisons between theory and experiment in terms of modal spectra for increasing pump power, with the theory plots derived from numerical solutions to the LLE with a changing detuning, and the experimental plots found by monitoring the intracavity intensity whilst sweeping the laser frequency over a cavity resonance. The final row gives a comparison of the comb spectra calculated by the LLE and measured experimentally using an optical spectrum analyser (OSA).

The top row of Fig. 2.14 shows the theoretical and experimentally measured modal spectrum for a WGM resonance at low input power. They both correctly

[1]N.B. The Fabry-Pérot cavities studied in Ref [62, 63] have an additional nonlinear term due to the counter-propagating fields in such a resonator geometry. This term changes the effective detuning of the system (which can be removed with a commensurate redefinition of detuning) but has no qualitative effects and so is disregarded for the rest of this work.

show a Lorentzian like profile, with the experimental version already showing some skew to the right due to thermal effects (see below).

The middle row shows the spectra when the input power is higher. Now, rather than the basic Lorentzian shown above, the LLE predicts a *tilted* profile - this can be explained by the nonlinear refractive index which pushes the resonance condition to the right in terms of detuning from a weakly pumped cavity. Accordingly, the frequency-sweeping laser pushes and follows this resonance, tuning into resonance slowly. Immediately after the laser is on resonance, the dynamics of this system reverses and so the system detunes quickly leading to a sudden drop in cavity intensity. The experimental trace shows a similar, though more dramatic version, of this effect due to the presence of thermal nonlinearities which tend to be orders of magnitude more substantial than the Kerr-effect for such resonators.

The third row shows the spectrum of a mode for which frequency comb generation occurs. Part way through the resonance, there is a characteristic notch - a dip in power - which implies the onset of FWM causing a drop in the intracavity power. This notch is seen in both the theory and experimental plots, which both show qualitative similarity.

The lower row shows the associated cavity spectra during comb generation. Fig. 2.14g) shows two such spectra - calculated as the Fourier transform of the LLE solution $\psi(\tau, \theta)$ - for detunings corresponding to the respective positions in Fig. 2.14. Before the characteristic notch (green), the cavity field is monochromatic as the system is below threshold stimulated FWM. After this notch (red), stimulated FWM occurs, leading to a frequency comb spanning many modes. Fig. 2.14h) shows a similar spectrum measured from a similar cavity field, showing the versatility of the LLE to describe a broad range of effects in Kerr resonators.

2.3.10 Thermal locking of laser to resonator

It is of great importance to be able to maintain a constant and controllable detuning between the laser and cavity in order to explore different dynamical regimes. Thermal and mechanical fluctuations in both the laser and cavity can lead to fluctuations of their lasing and resonance frequencies respectively, and so techniques have been developed to "lock" these with respect to each other.

Active locking requires the pump to have some modulation applied to it, such that a signal can be produced that is proportional to the laser-cavity detuning. The Pound-Drever-Hall technique [65] is the archetype of such optical locking methods which can be augmented to allow for the control of the locked detuning [66]. Such methods require pump modulation, and an extraction of some proportion of the output light from the cavity, both of which can degrade the signal needed for the experiment.

Passive locking is a technique in which cavity nonlinearities keep the resonance frequency of the cavity fixed with respect to the laser with no need for active feedback. Along with the simpler experimental setup associated with these techniques, the pump can be truly monochromatic and no output light need be monitored to maintain the lock, maximising the signal-to-noise ratio for the experimental results.

The thermal effect - due to the thermal expansion of the cavity and thermo-refractive effects in silica - gives a strong nonlinearity that can be used to form a passive lock [67]. Both thermal effects, like the Kerr-effect, act to increase the

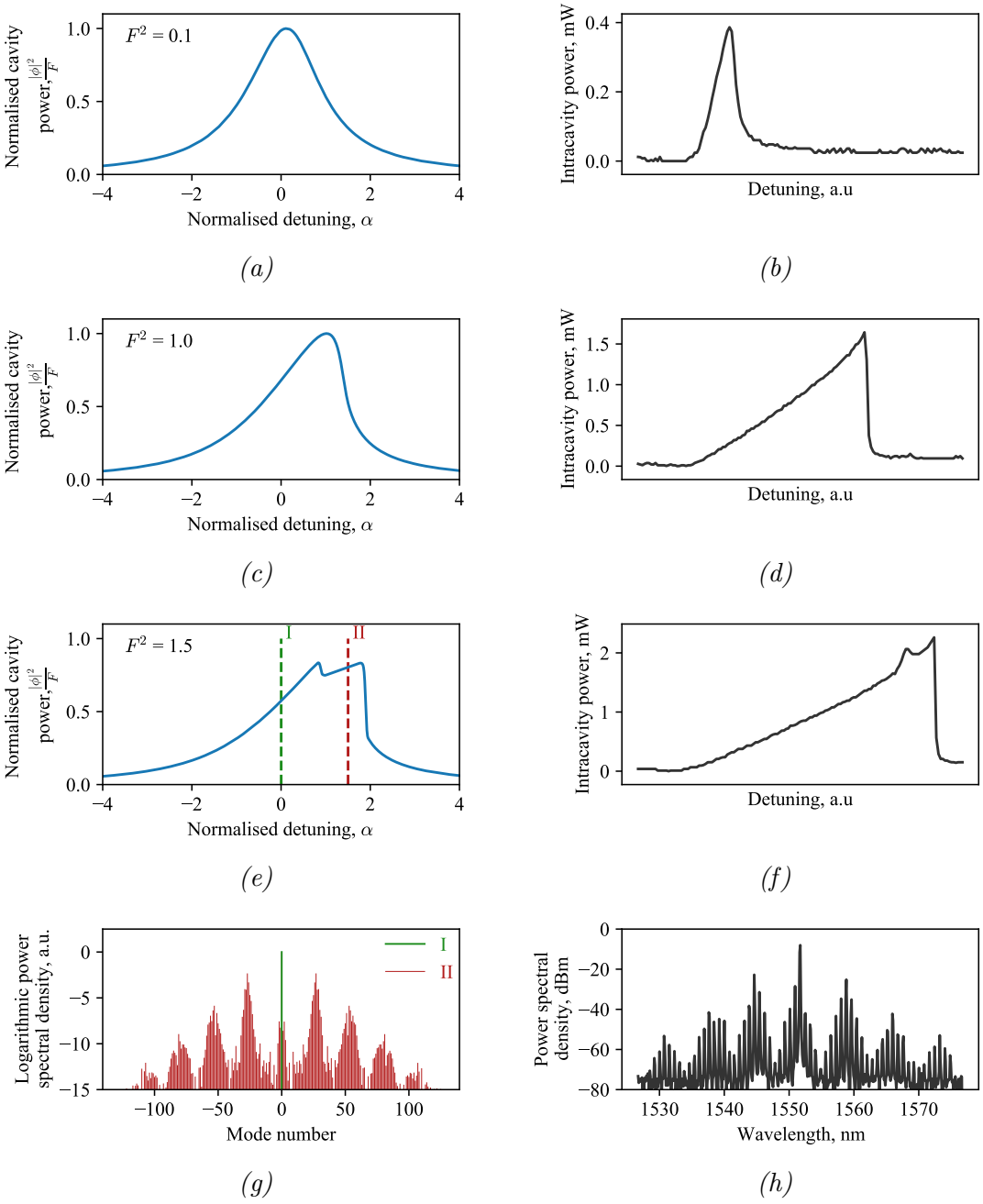

Figure 2.14: Theoretical and experimental modal spectra. a) Solution to the LLE during a frequency sweep across a resonance. b) Experimental measurements of the intracavity power during a frequency sweep across a resonance. c-f) As per a) and b), with increasing pump power. g) Spectra associated with the cavity fields shown in part e), which is monochromatic before the characteristic dip in intracavity power, and becomes a frequency comb thereafter. h) Experimental measurement of a comb qualitatively similar to the theoretical prediction shown in g) II.

effective path length for light inside a resonator and so can be considered in this context as the thermal term in Eq. (2.36). Drifts in either the laser or resonance frequency manifest as an increase (decrease) in detuning, α, reducing (increasing) the intracavity intensity, $|\psi|^2$. When $\alpha > 0$ (i.e. the laser is red-detuned from the cavity), these effects evolve to cancel each other, giving a passive lock. However, there is an associated instability when both of these effects work in tandem (i.e. when $\alpha < 0$ i.e. the laser is blue detuned from the cavity), in which there can be no such locking possible.

Chapter 3

Spontaneous symmetry breaking of the polarisation of light

3.1 Introduction

An entirely symmetric universe would be exceedingly dull. Spatial translation and rotational symmetries would ensure that all the "stuff" that makes up such a universe would be uniformly distributed in an eternal (thanks to time-translation symmetry) blob - no, even blobs have spatial structure - in an eternal void. Luckily, symmetries can break.

Spontaneous symmetry breaking - the evolution of a system for which both the initial state and the equations of motion possess some symmetry into a state which no longer has such symmetry - is an intriguing process that underpins much of modern physics. It is responsible for the description of superconductivity [69], the Higgs mechanism [70] and the phases of matter [71], to name but a few areas.

The prototypical example of symmetry breaking is given by a particle in a nonlinear, sombrero potential, see Fig. 3.1. This system shows rotational symmetry about its central axis, though coupling the particle to some noise source - which could in principle be due to quantum fluctuations - will lead the particle to fall in a certain direction, breaking the symmetry. This picture nicely illustrates the underlying concept behind the polarisation spontaneous symmetry breaking (PSSB) discussed in this chapter: the Kerr-effect leads to a potential that, although symmetric, has an unstable symmetric state for some sets of system parameters. A similarly symmetric input state couples to a source of noise (in principle due to vacuum fluctuations, in practice due to experimental noise) and thus spontaneously breaks the symmetry, "choosing" one of two polarisation states.

Such nonlinear optical interactions that lead to symmetry breaking have been well explored in the literature. An example is time-reversal symmetry breaking in a pulse-pumped ring cavity [72, 73]. In addition, the Kerr interaction plays an important role in the interaction of soliton frequency combs in microresonators [74–78], which can be thought of as having broken time-translation symmetry. In the continuous wave regime, spontaneous symmetry breaking has been observed [79–

This chapter expands on work I wrote as first author in Ref [68]. Passages and figures from this original work conducted by myself may be directly adapted into this chapter where appropriate.

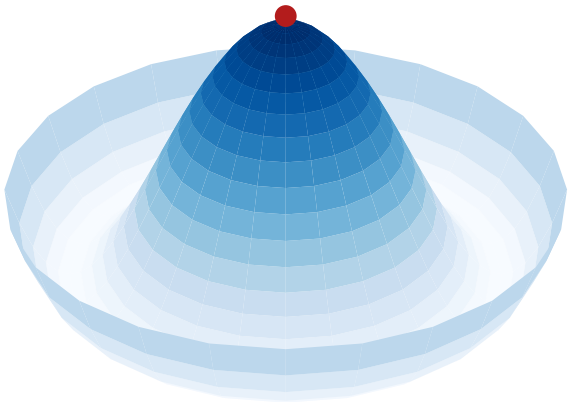

Figure 3.1: A particle in a sombrero, or Mexican hat, potential. The system is rotationally symmetric about the central axis, though we can intuit that coupling to some noise source will lead the particle to fall in a particular direction, thus breaking the symmetry.

81] between counter-propagating light in microresonators with high optical quality factors. In addition, recent work has predicted [49] and shown polarisation symmetry breaking of optical pulses in fiber ring resonators with residual birefringence [82–85] using peak pulse powers of 2.7 W (average power of 110 mW) and multi-color input light [86]. The high finesse and polarisation degenerate cavity presented here enables the observation of polarisation symmetry breaking for continuous wave and monochromatic input light at 7 mW optical power.

Here, an experimental demonstration of symmetry breaking of the polarisation states of continuous wave light in geometrically linear Fabry-Pérot-type cavities is given. This symmetry breaking is demonstrated for linearly polarised input light that is sent into a high Finesse fiber cavity. At low powers this system maintains symmetry such that the polarisation of the cavity field matches that of the input. At a measured threshold power of 7 mW, spontaneous symmetry breaking of the resonator modes splits up the linear polarised light into left and right polarised light, with one handedness being transmitted and the other one reflected. We further demonstrate that the output polarisation can be optically controlled by using a resonator with slight asymmetries due to birefringence. This enables us to continuously change the output polarisation state from linear to elliptical and close to circular polarisation. Together with an additional polariser, the Kerr polarisation symmetry breaking can be used to generate an orthogonal polarisation component with respect to the linear polarised input light.

Such a phenomenon could find application as an all-optical polarisation controller in photonic circuits. Many optical effects only occur for specific polarisation states, and so having active control over a fields polarisation is a necessity for many situations. The most familiar polarisation controllers used in optics laboratories use birefringence to convert an input polarisation state to the intended output. For free-space systems, these include quarter- and half-waveplates which retard the polarisation component that is aligned to the optical axis of the constituent crystal

by a quarter, or half, of a wavelength. Rotating these crystals (and hence their optical axes) can be used to perform an arbitrary polarisation transformation. For fiber-optic systems, a common polarisation controller uses a succession of loops of fiber, the planes of which can each be independently rotated to give stress induced birefringence. Again, proper alignment can lead to arbitrary polarisation control.

Both these systems are sizable, and require manual - and hence slow - control, neither of which allow for the integration into useful photonic devices. Accordingly, achieving fast polarisation control remains an active area of research within the photonics community.

One method for on-chip polarisation *rotation*, rather than control, is in using waveguides with variable cross-section [87, 88]. Here, the adiabatic rotation of the waveguide profile gives a commensurate rotation of the optical mode that traverses it. Accordingly, the polarisation of the output field of such a device will be rotated from that of its input. This is set by the waveguide geometry, which is not modified after fabrication. Thus, though arbitrary rotation angles are possible, one cannot use this method to vary the output polarisation state on-the-fly[1].

Another method for polarisation rotation is to use the Faraday effect. Here, an external magnetic field is used to rotate the polarisation using the magneto-optic effect [89, 90]. Such devices allow for polarisation control but require complex fabrication methods to integrate, control, and shield magnetic fields on a photonic chip.

The electro-optic effect can also be used for polarisation control on-chip [91, 92]. Such devices use the $\chi^{(2)}$ nonlinearity in some materials to produce a controllable refractive index change for different polarisation components. Accordingly, one polarisation mode is retarded with respect to the other, leading to a rotation. Such devices can operate at high speed, but are limited to crystalline materials for which such a nonlinearity is present. On-chip polarisation control using thermal and mechanical actuation has also been demonstrated [93–96], though this can either have complex fabrication processes or operate at low speeds.

The polarisation controller demonstrated in this chapter is all-optical, meaning the control mechanism is also an optical field. Accordingly, this has minimal associated requirements on the fabrication process as any photonic system will naturally be supporting optical fields. Moreover, the nonlinearity that is exploited in this device is the Kerr-effect which is present in all materials and thus can work for any chip design. However, there remains a challenge to incorporate high finesse mirrors on-chip to generate the polarisation degenerate cavities required for operation.

The polarisation interactions discussed here are mathematically analogous to the Kerr interaction between counter-propagating light [49, 79, 80, 97]. Thus, this effect can be similarly used for all-optical information processing and storage of information [98–102]. Integration of this system on-chip would also give enhanced sensing of polarisation effects beyond shot noise limitations.

[1]This is not a drawback of such a system - fixed polarisation rotations are often needed and such waveguide geometries are a promising solution to this problem.

3.2 Theory

3.2.1 Nonlinear coupled equations

The Lugiato-Lefever Equation (LLE) of Eq. (2.36) can have fast dynamics ignored (i.e. assuming a uniform, monochromatic, cavity field) and the nonlinear term can be decomposed into two coupled nonlinear equations for light of opposite handed circular polarisations[2] [81]:

$$\frac{\partial \psi_{\pm}}{\partial \tau} = -\left(1 + i\left(\alpha - |\psi_{\pm}|^2 - 2\,|\psi_{\mp}|^2\right)\right)\psi_{\pm} + \tilde{\psi}_{\pm}, \tag{3.1}$$

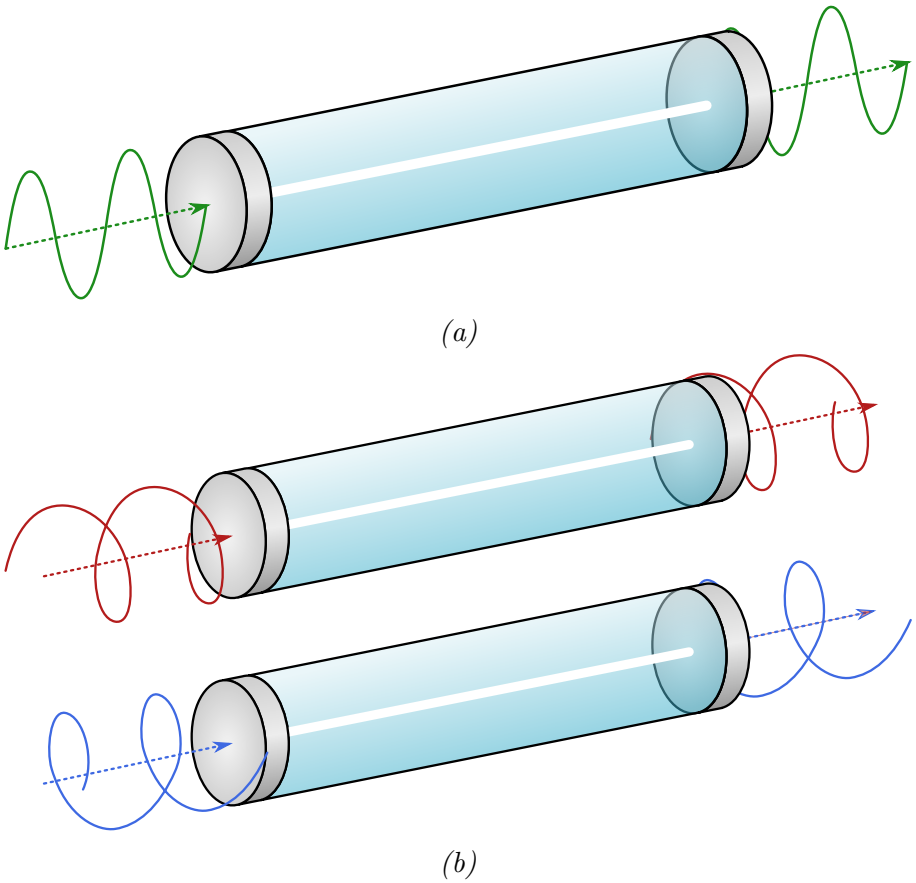

Figure 3.2: Coupling of light into a polarisation degenerate Fabry-Pérot cavity. a) The polarisation degeneracy, due to a lack of birefringence, means that an arbitrary polarisation state can couple into the cavity subject to resonance conditions. b) Any such polarisation state can be decomposed into two circular polarisation components of opposite handedness: ψ_+ (red) and ψ_- (blue).

where ψ_+ (ψ_-) is the clockwise (anti-clockwise) handed circular polarisation component of the normalised cavity field, α is the normalised laser-cavity detuning, and the tilde represents an input field.

[2]This is somewhat simplified - the nonlinear term in Eq. (2.36) doesn't account for the tensor nature of the $\chi^{(3)}$ nonlinearity nor the modification to the detuning due to the counter-propagating fields described in Refs [62, 63], but the decomposition can be performed in the same way as described to yield Eq. (2.34)

These equations are valid for describing the cavity fields in a resonator that exhibits no linear coupling between any polarisation modes. Such cavities require zero birefringence, leading to polarisation degenerate modes such that an arbitrary input polarisation can couple into and through the cavity - see Fig. 3.2 - giving an apparent symmetry of the cavity polarisation with respect to the input (i.e. it should be exactly the same). Let us see how the nonlinear dynamics can break this symmetry following the method descibed in [81].

In steady state, Eq. (3.1) becomes:

$$\psi_{\pm} = \frac{\tilde{\psi}_{\pm}}{1 + i\left(\alpha - |\psi_{\pm}|^2 - 2|\psi_{\mp}|^2\right)}, \tag{3.2}$$

which multiplication by the complex conjugate gives the normalised intensities in the modes:

$$|\psi_{\pm}|^2 = \frac{|\tilde{\psi_{\pm}}|^2}{1 + \left(-\alpha + |\psi_{\pm}|^2 + 2|\psi_{\mp}|^2\right)^2}. \tag{3.3}$$

When the two modes are equally pumped - $\left|\tilde{\psi}_{+}\right| = \left|\tilde{\psi}_{-}\right| = \left|\tilde{\psi}\right|$, corresponding to a linearly polarised input which we define as being the vertical state when these inputs are in phase - this system is symmetric with respect to polarisation as evidenced by the ability to exchange the $\pm$ indices without change to the equations of motion. Now as the modes have identical pumps, Eq. (3.1) can become:

$$\begin{gathered} |\psi_{+}|^2\left(1 + \left(-\alpha + |\psi_{+}|^2 + 2|\psi_{-}|^2\right)^2\right) = |\psi_{-}|^2\left(1 + \left(-\alpha + |\psi_{-}|^2 + 2|\psi_{+}|^2\right)^2\right), \\ \left(|\psi_{+}|^2 - |\psi_{-}|^2\right)\left(|\psi_{+}|^4 + |\psi_{+}|^2|\psi_{-}|^2 + |\psi_{-}|^4 - 2\alpha\left(|\psi_{+}|^2 + |\psi_{-}|^2\right) + \alpha^2 + 1\right) = 0. \end{gathered} \tag{3.4}$$

The first term in this equation - $\left(|\psi_{+}|^2 - |\psi_{-}|^2\right)$ - gives the symmetric solutions to the system: it is zero when both polarisation components have the same intensity and thus the equation is satisfied. Interestingly, the second term can, for certain input powers and detunings, equal zero also satisfying this equation. These describe the symmetry broken states to the system in which $|\phi_{+}|^2 \neq |\phi_{-}|^2$ even though the system and inputs are symmetric with respect to these intensities!

Figure 3.3 shows the solutions to Eq. (3.4), with the black line being the symmetric solution and the ellipses being the symmetry broken states for different detunings. For a given detuning, the symmetric solutions inside of the associated ellipse are unstable. This now describes how the system responds to increasing (equal) input powers for both modes at a fixed detuning: starting at the origin, both modal cavity intensities equally increase by following the black line. If the detuning is above some threshold ($\alpha > \sqrt{3}$ [81]) at some point this black line reaches an ellipse at which point the system spontaneously selects a path - upper left for $|\psi_{-}|^2 > |\psi_{+}|^2$ or lower right for $|\psi_{+}|^2 > |\psi_{-}|^2$ - at random. The system then follows this ellipse with increasing input power before eventually meeting the black line again, after which it both modes again symmetrically increase with input power.

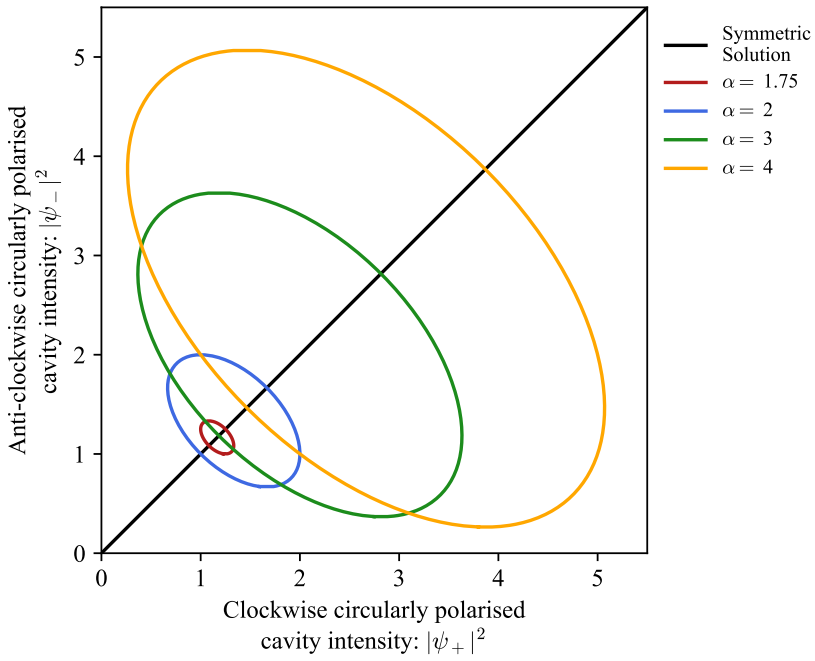

Figure 3.3: Coupled intracavity intensities for symmetrically pumped circular polarisation modes. These lines are solutions to Eq. (3.4), with the black diagonal being the symmetric solution and the ellipses being the symmetry broken solution for different detunings. For a given detuning, this plot is found by varying the input power.

3.2.2 Physical description of symmetry breaking

The two factors which determine how much power couples into a cavity are the input power and the effective detuning. The effective detuning in this system has three contributions, as seen in the denominator of Eq. (3.1): laser-cavity detuning (α), self-phase modulation (SPM, $|\psi_\pm|^2$), and cross-phase modulation (XPM, $2|\psi_\mp|^2$). Accordingly, the cavity intensities are self-referential (SPM) and coupled across modes (XPM). Importantly, the factor of two difference in magnitude between XPM and SPM means that two modes with different cavity intensity will have different effective detunings i.e. a nonlinear splitting of the otherwise degenerate resonances.

The intensity dependent refractive index in dielectrics - both SPM and XPM - acts to increase the refractive index with intensity. This acts to reduce the resonance frequencies with increasing cavity intensity, with XPM having twice the magnitude of effect of SPM. Accordingly, when a laser frequency is swept from above to below a cavity resonance (at speeds much slower than the cavity dynamics), light progressively couples into the cavity and the associated resonance frequency is pushed away from the laser. As the laser frequency finally reaches the (now shifted) resonance frequency, the situation is reversed: less light couples into the cavity, whose resonance condition now returns back towards its original value. Together these phenomena lead to a triangular response of the intracavity power for both polarisation modes with respect to the laser-cavity detuning, as shown in Fig. 3.4.a).

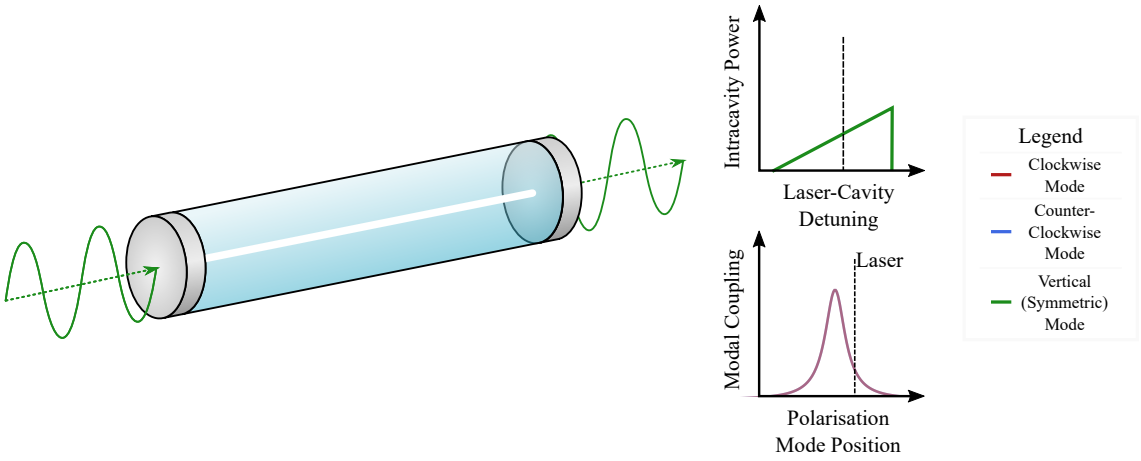

(a) Symmetric state (sub-symmetry breaking threshold)

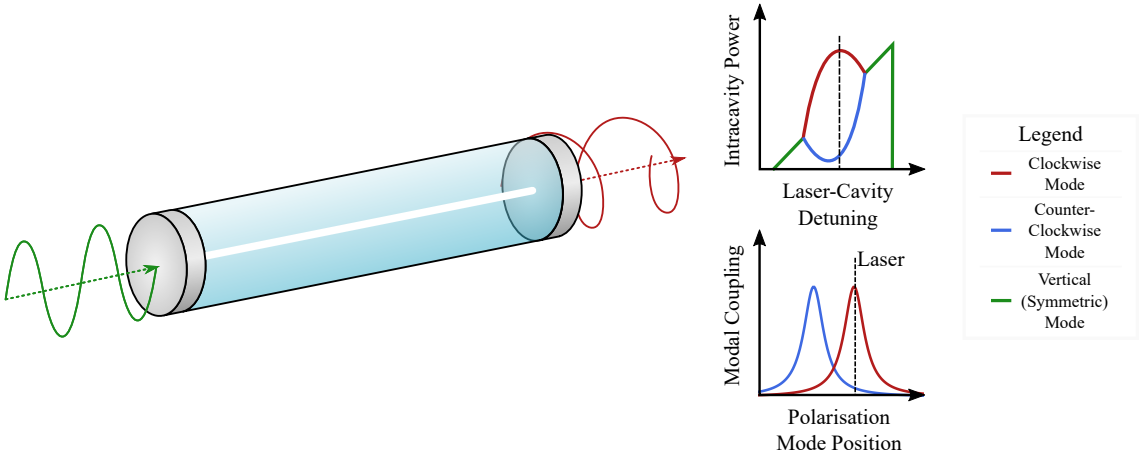

(b) Right-handed polarisation symmetry broken state

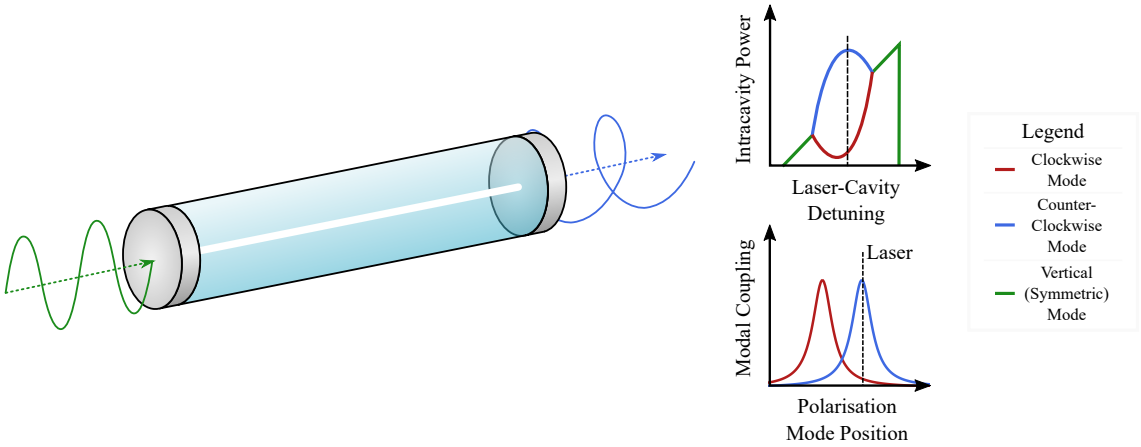

(c) Left-handed polarisation symmetry broken state

Figure 3.4: Physical description of polarisation symmetry breaking. Each subfigure shows a representation of the input fields to, and output fields from, a polarisation degenerate F-P cavity. Also shown is the intracavity intensity response for both modes as the laser is swept across a resonance, showing a Kerr-triangle below threshold and a symmetry broken "bubble" above threshold. The effective positions of both modes with respect to the input laser are then shown for a certain laser-cavity detuning, showing how one mode preferentially couples in the symmetry broken state.

The symmetry breaking phenomena can be explained by a competition between both modes due to the difference in magnitudes of SPM and XPM. The intensity of one mode will push its own resonance frequency by some amount, but will push that of the other mode by twice the amount. For suitable powers and detunings, this can then lead to a reduction in the intensity of the secondary mode, thus bringing the primary mode closer into resonance. This leads to a frequency splitting of the two otherwise degenerate polarisation modes, with one preferentially coupling into the cavity and dominating the other, see Fig. 3.4.b,c).

This is the physical principle for which the symmetry breaking phenomena happens: both circular polarisation modes are in competition, each trying to push the other from resonance to bring themselves closer in the process. This competition is typically self-stable, with both fields coupling in equally, but becomes unstable for certain input powers and detunings. In this situation, any noise that leads to some small domination of one mode will become amplified leading to the symmetry broken state, with the dominant mode being random due to the stochastic nature of the underlying noise process.

3.2.3 Polarisation state of the symmetry broken cavity field

The Poincaré sphere is a useful tool for visualising a polarisation state. Linear polarisation states exist on the equator of the sphere, with their orientation set by their angular position and the opposite handed circular polarisation states are on the poles. The remainder of the sphere surface denotes elliptical polarisation states. The Poincaré sphere is shown in Fig. 3.5, and one can see how any state can be defined by two angular parameters: ψ and χ, which refer to the orientation and ellipticity of the state respectively. To avoid confusion from ψ referring to both electric fields, as in the equations above, and as the orientation angle, the polarisation orientation will be given by ϕ such that $2\phi = 2\psi + \pi$ and $\phi = 0$ referring to vertically oriented polarised light.

Now, the polarisation state of the system can be referred to as $|\psi\rangle$ which can be decomposed into the circular polarisation basis ($|+\rangle$: right-handed, $|-\rangle$: left-handed):

$$\begin{aligned} |\psi\rangle &= \psi_+ |+\rangle + \psi_- |-\rangle , \\ &= \sqrt{|\psi_+|^2 + |\psi_-|^2} e^{i\phi_{\text{global}}} \left(\cos\left(\frac{\pi}{4} - \chi\right) |+\rangle + \sin\left(\frac{\pi}{4} - \chi\right) e^{i\phi} |-\rangle \right), \end{aligned} \tag{3.5}$$

which shows that the polarisation parameters can be calculated from knowledge about the field amplitudes $\psi_\pm$. There is also a global phase ϕ_{global}, which can be ignored with no loss of generality.

Finding χ

From Eq. (3.5) we have:

$$\sin\left(\frac{\pi}{4} - \chi\right) = \frac{|\psi_-|}{\sqrt{|\psi_+|^2 + |\psi_-|^2}}, \tag{3.6a}$$

$$\cos\left(\frac{\pi}{4} - \chi\right) = \frac{|\psi_+|}{\sqrt{|\psi_+|^2 + |\psi_-|^2}}, \tag{3.6b}$$

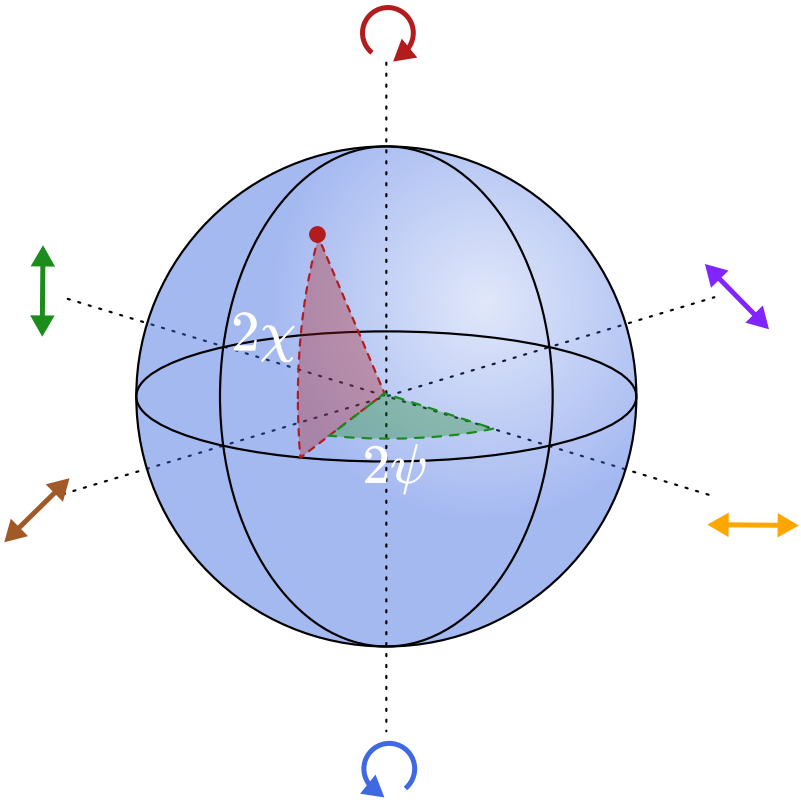

Figure 3.5: The Poincaré sphere. Any purely polarised state can be represented as a point on the surface of this sphere, described by an orientation angle ψ, and ellipticity angle χ. N.B. to avoid confusion between this angle and the electric field states, both denoted ψ, instead the orientation angle will subsequently be given by ϕ and be relative to the vertical rather than horizontal polarisation state.

$$\tan\left(\frac{\pi}{4}-\chi\right)=\frac{|\psi_-|}{|\psi_+|}, \tag{3.6c}$$

which using the identities $\tan(-\theta) = -\tan(\theta)$, $\tan\left(\theta \pm \frac{\pi}{4}\right) = \frac{\tan(\theta)\pm 1}{1\mp\tan(\theta)}$, and $\tan(2\theta) = \frac{2\tan(\theta)}{1-\tan^2(\theta)}$ gives:

$$2\chi = \arctan\left(\frac{1}{2}\left(\frac{|\psi_+|}{|\psi_-|}-\frac{|\psi_-|}{|\psi_+|}\right)\right), \tag{3.7}$$

which is zero whenever $|\psi_+| = |\psi_-|$ i.e. the cavity polarisation ellipticity is only nonzero in the symmetry broken state.

Finding ϕ

Multiplying the top and bottom of Eq. (3.2) by the complex conjugate of its denominator gives the following expression for the steady state fields inside the resonator:

$$\psi_\pm = \frac{\tilde{\psi_\pm}}{1+\left(-\alpha+|\psi_\pm|^2+2|\psi_\mp|^2\right)^2}\left(1-i\left(\alpha-|\psi_\pm|^2-2|\psi_\mp|^2\right)\right). \tag{3.8}$$

Taking the phase of the inputs to be zero, which only affects the global phase of the cavity fields and does not affect ϕ, the fractional term of Eq. (3.8) is purely

real, and so the argument becomes:

$$\angle\psi_{\pm} = \arctan\left(-\alpha + |\psi_{\pm}|^2 + 2\,|\psi_{\mp}|^2\right). \tag{3.9}$$

Now the global phase is simply $\angle\psi_+$, and 2ϕ is the phase difference between the modes:

$$\begin{aligned} 2\phi &= \angle\psi_- - \angle\psi_+, \\ &= \arctan\left(-\alpha + |\psi_-|^2 + 2\,|\psi_+|^2\right) - \arctan\left(-\alpha + |\psi_+|^2 + 2\,|\psi_-|^2\right), \\ 2\phi &= \arctan\left(\frac{|\psi_+|^2 - |\psi_-|^2}{1 + \left(-\alpha + |\psi_+|^2 + 2\,|\psi_-|^2\right)\left(-\alpha + |\psi_-|^2 + 2\,|\psi_+|^2\right)}\right), \end{aligned} \tag{3.10}$$

which again is zero for the symmetric solution $|\psi_+| = |\psi_-|$.

Accessible region of the Poincaré sphere

Equations (3.7) & (3.10) can be used with the solutions of Eq. (3.4) to determine the accessible region of the Poincaré sphere. For the symmetric solutions both χ and ϕ are zero, meaning that the cavity polarisation state is equal to that of the input (defined as being vertically polarised). Only when the symmetry has broken - when there has been a split in the resonance condition for both circular polarisation modes - is there a difference. This is because both the *intensity* and *phase* of a cavity field in comparison to the associated input are affected by the effective input-cavity detuning. When the otherwise degenerate modes split, both circular polarisation modes couple in at different intensities (leading to the cavity field developing an ellipticity χ) and different phases (shifting the orientation of the vertical input polarisation by an amount ϕ).

Figure 3.6 shows the accessible region on a (flattened) Poincaré sphere, with the colour representing the detuning (upper panel), and input power (middle panel) required to reach this state. For interest, the associated total cavity power is also shown in the lower panel. Unsurprisingly, polarisation states far from the origin - and thus significantly different to the input polarisation - require higher cavity intensities.

It seems that, for limitless input powers and detunings, half of the Poincaré sphere is accessible: specifically in both the upper-right and lower-left quadrants. The particular quadrant that is accessed is determined by the symmetry breaking direction: upper-right when $|\psi_+| > |\psi_-|$, lower-left when $|\psi_+| < |\psi_-|$.

3.2.4 Birefringence

The nonlinear coupled equations described in Section 3.2.1 show the same detuning for both polarisation modes. This means that they are valid for modes $\psi_{\pm}$ that are - in the absence of the nonlinear splitting - frequency degenerate.

In general however, this isn't the case: a single mode fiber cavity will show *two* distinct polarisation modes of different frequencies due to the difference in the refractive index for these polarisation states. This effect is caused by birefringence: either through fabrication asymmetries in the fiber and mirrors, or bending/stresses.

Birefringence is a linear optical phenomenon and arises from off-diagonal terms in the $\chi^{(1)}$ tensor. This linear coupling can be characterised by the following set of normalised equations [103]:

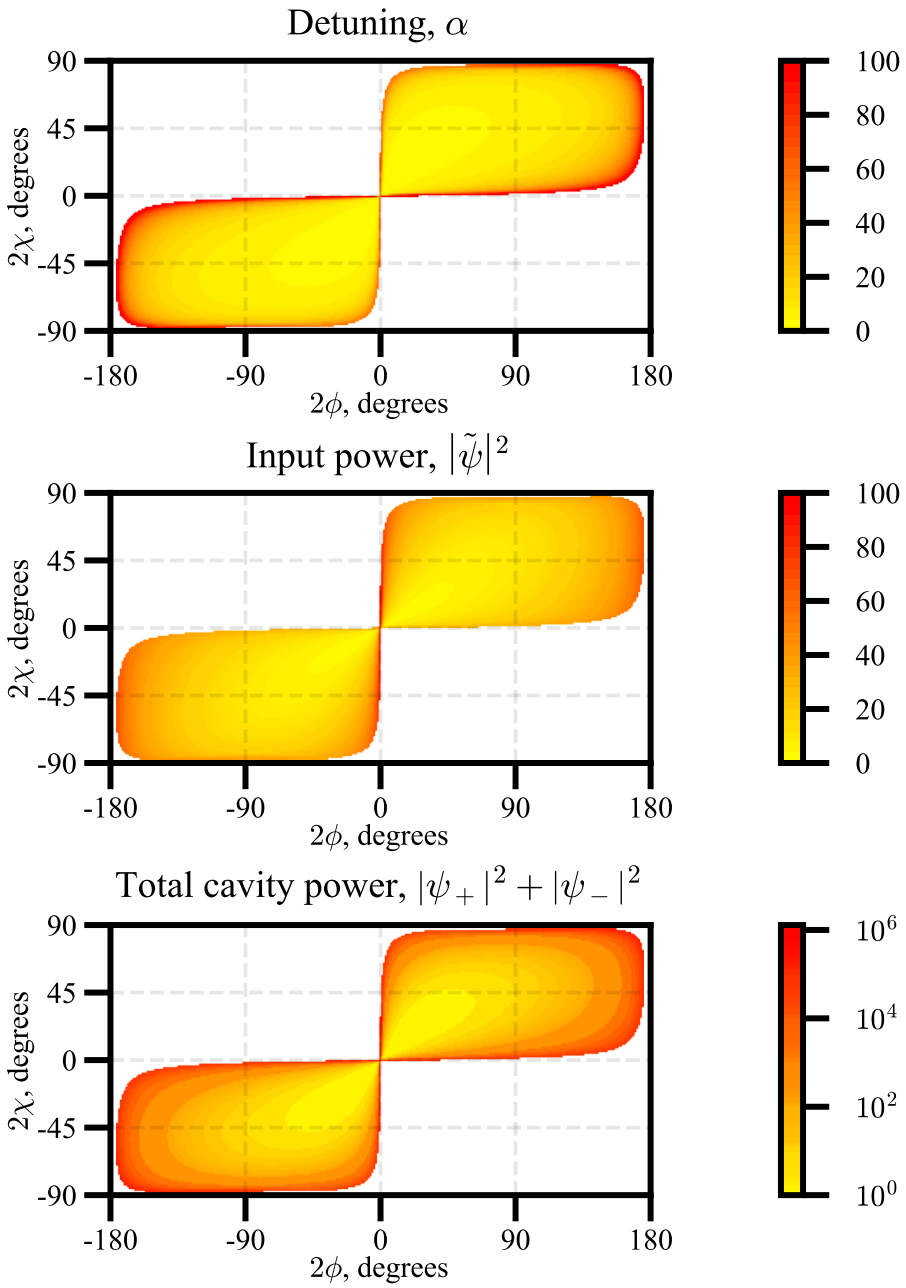

Figure 3.6: Accessible region of the Poincaré sphere. The accessible regions are shown in colours that represent the required detuning (upper-panel) and input power (middle-panel) required to access this polarisation state. Also shown is the associated cavity power (lower-panel, logarithmic scale) associated with these states.

$$\frac{\partial \psi_+}{\partial \tau} = -(1 + i\alpha)\,\psi_+ + i\kappa\psi_- + \tilde{\psi}_+, \tag{3.11a}$$

$$\frac{\partial \psi_-}{\partial \tau} = -(1 + i\alpha)\,\psi_- + i\kappa^\star\psi_+ + \tilde{\psi}_-, \tag{3.11b}$$

which are of the same form as Eq. (3.1), albeit with the nonlinear coupling replaced by linear coupling characterised by a strength κ.

Figure 3.7 shows the solution of Eq. (3.11), in terms of coupled cavity intensities, for different values of κ (though with the imaginary part fixed at $\Im(\kappa) = -3$). When $\Re(\kappa) \gg \Im(\kappa)$, two distinct resonant peaks are observed (Fig. 3.7 I). These peaks correspond to modes for which the two circular polarisation components are in-phase (ψ_v) and out of-phase (ψ_h), where v and h denote the vertically- and horizontally-polarised modes:

$$\psi_{v,h} = \frac{1}{\sqrt{2}} (\psi_+ \pm \psi_-) . \tag{3.12}$$

In this polarisation basis, there is no mutual coupling between the modes, but they have different associated detunings. This is more reminiscent of the idea of birefringence - the different modal detunings resulting from the different resonance frequencies associated with modes of mismatched refractive index. We can think of birefringence in two different ways: in terms of a polarisation basis where the components travel at different speeds, and there is no mutual coupling, *or* a different basis in which both components travel at the same speed but are mutually coupled.

In order to access the frequency degeneracy required for the observation of symmetry breaking, the linear coupling must be removed. As κ is complex valued, this is a 2-dimensional problem - both the real and imaginary parts must be reduced to zero. Simply adjusting the real part of κ - as in the upper panels of Fig. (3.7) - leads to an avoided crossing rather than degeneracy. Panel II shows the closest approach of the avoided crossing, with two peaks corresponding to two hybrid modes in the $\psi_{v,h}$ basis that are still separated in frequency. The process to control the real- and imaginary-parts of the coupling separately, in order to set both to zero and achieve polarisation degenerate modes is described in section 3.4.4.

3.3 Experimental Methods

This section details the experimental work that was done to demonstrate Kerr-polarisation control. It starts with a description of the main elements of the resonator, which allow for the realisation of high-Q polarisation degenerate modes, before showing how this is incorporated into a wider experimental setup.

3.3.1 Fiber Bragg Mirrors

The fiber Bragg mirrors used in this work were fabricated by a collaborator. Although this process was not undertook as part of this thesis, it is worthy of a brief description for a complete understanding of the work.

Bragg mirrors use alternating layers of (typically) two materials with differing refractive index to achieve a highly reflective surface. At each interface between the materials there is a partial reflection and partial transmission of incident light due to the differing refractive indices. When the layers are of precisely the correct thickness (quarter wavelength is typical) interference effects occur between the set of reflected and transmitted waves such that the vast majority (far exceeding 99%) of the light is coherently reflected from the structure.

The following passage gives a detailed description of the fabrication process as given by a co-author in Ref [68]:

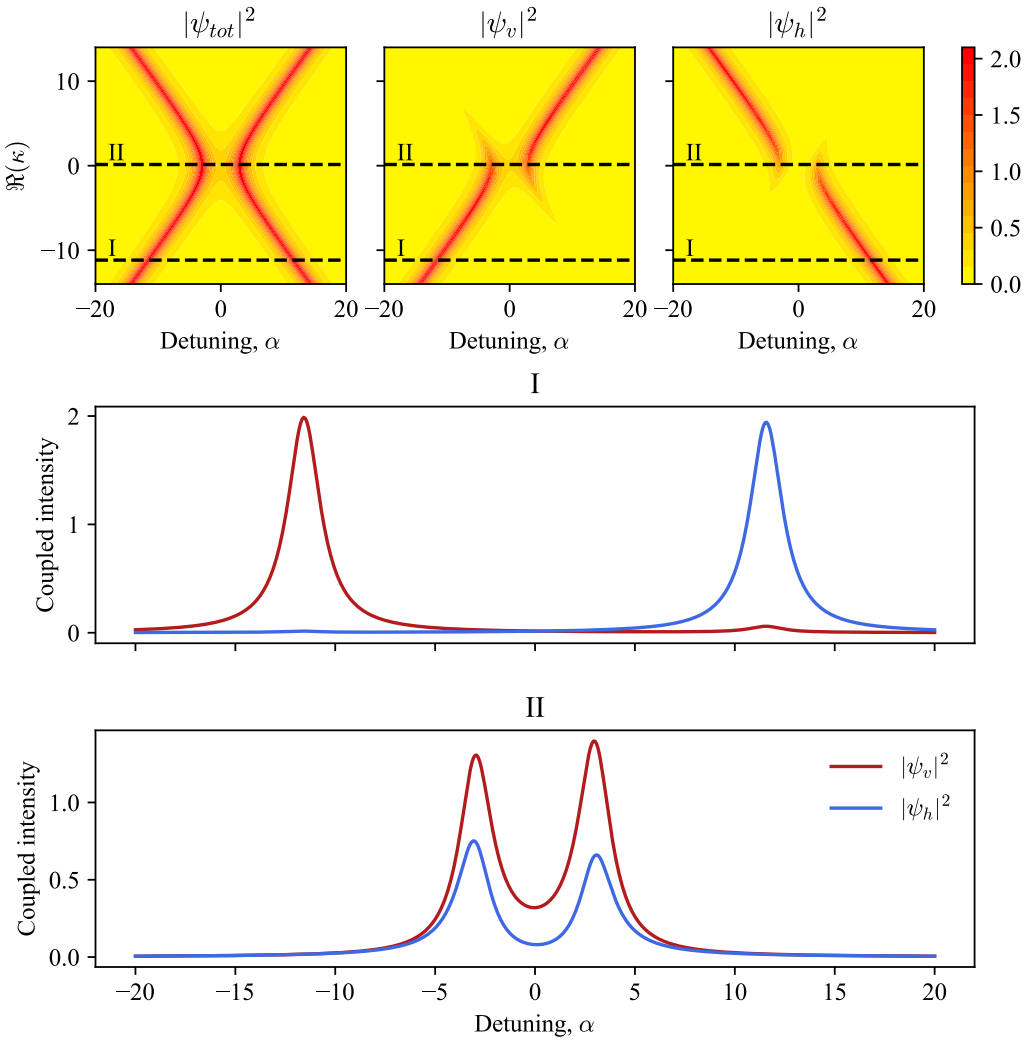

Figure 3.7: Avoided crossing behaviour of linearly coupled modes. When the real part of the coupling coefficient κ is swept across zero, but there is a constant imaginary part (here $\Im(\kappa) = -3$) an avoided crossing is seen. I) When the magnitude of $\Re(\kappa)$ is high two distinct peaks are seen, corresponding to the $\psi_{v,h}$ modes. II) When the real part is zero, residual coupling from $\Im(\kappa)$ inhibits these modes from overlapping in frequency, instead leading to hybrid modes in the $\psi_{v,h}$ basis.

The Bragg mirrors are produced with an reactive ion beam sputtering (IBS) thin-film deposition process (Navigator 1100, CEC GmbH) using Xenon as a sputtering gas. The IBS technology stands out by its ability to deposit layers with exceptionally low scattering loss and low residual absorption. Tantalum pentoxide (Ta_2O_5, $n_H = 2.124$ at $\lambda_c \approx 1550$ nm) and silicon dioxide (SiO_2, $n_L = 1.479$ at $\lambda_c \approx 1550$ nm) are used as high-refractive index and low-refractive index materials, respectively. The oxides are formed by oxidation of the metallic Ta (5N purity) and Si (9N purity) released from the sputtering targets with a deposition rate of about 0.1 nm/s. Before deposition, the vacuum chamber is evacuated down to a level in the range of $1 \times$

10^{-7} mbar. *During the deposition the vacuum pressure doesn't exceed* 2×10^{-3} mbar *and the holder of the fiber tips was heated and temperature controlled to* 60 ℃. *No post-processing or annealing is applied to the samples after the deposition. The automated coating process is precisely controlled by broadband optical monitoring. The layerstack is build up by starting with a half-wave layer of* SiO_2 *and then 9 quarter-wave layers of* Ta_2O_5 *interleaved with 8 quarter-wave layers of* SiO_2 *and then closed with a half-wave layer of* SiO_2. *In this way the coating starts with a layer that closely matches the refractive index of the core of the fiber on which it is coated and with the one it is in contact and the half wave thickness minimises the influence of the interface from core to coating since it is placed at a node of the standing wave formed by the incoming and reflected wave (see Fig. 3.8).*

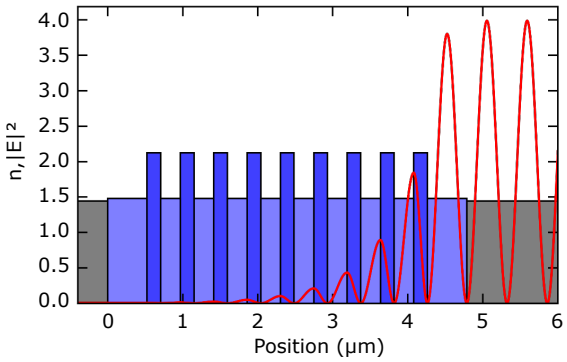

Figure 3.8: Design of the layer stack of the Bragg mirror. The height of the bars indicates the refractive index n of the silica fiber core (gray), coated SiO_2 *(light blue) and coated* Ta_2O_5 *(blue). The red line shows the electric field intensity* $|E|^2$ *formed by the normalised incoming wave coming from the right side and the reflected wave.*

3.3.2 Polarisation Degenerate Modes

Fundamentally, the polarisation controller here described relies on the Kerr-induced frequency splitting of otherwise degenerate (circular) polarisation modes. Birefringence manifests due to the linear coupling between two orthogonal polarisation components of the field, and leads to polarisation states with different associated refractive indices. Accordingly, in a resonator, there will be two polarisation modes with the same longitudinal mode number, but differing resonance frequencies: linear coupling leads to resonance splitting. If the magnitude of this resonance splitting is too great, the system does not behave symmetrically with respect to input polarisation and so the nonlinear effects are obscured.

In order to observe symmetry breaking, it was found experimentally that the differences between the resonance frequencies for the orthogonal circularly polarised modes ($\omega_\pm$) due to birefringence must be less than $\approx 5\%$ of their linewidths ($\delta\omega_+ \approx \delta\omega_- \approx \delta\omega$).

$$|\omega_+ - \omega_-| < 0.05\ \delta\omega, \tag{3.13}$$

which can be written in terms of the average resonance frequency ω_0 and the cavity

Q-factor:

$$\begin{aligned} |\omega_+ - \omega_-| &< 0.05\frac{\omega_0}{Q} \\ \frac{|\omega_+ - \omega_-|}{\omega_0} &< \frac{0.05}{Q}. \end{aligned} \tag{3.14}$$

Since the resonance frequencies are inversely proportional to their respective refractive indices (and both modes were confirmed to have the same longitudinal mode number), this becomes:

$$\begin{aligned} n_0\left|\frac{1}{n_+} - \frac{1}{n_-}\right| &< \frac{0.05}{Q}, \\ n_0\frac{|n_- - n_+|}{n_+ n_-} &< \frac{0.05}{Q}, \\ \frac{\delta n}{n_0} &< \frac{0.05}{Q}, \end{aligned} \tag{3.15}$$

where $\delta n = |n_+ - n_-|$ is the difference between the refractive indices for the orthogonal circularly polarised modes, and n_0 is their average. The last step of this derivation is valid for small values of δn, which is the case for high-Q cavities. In our case, the Q-factor of 4.9×10^8 leads to the requirement of $\frac{\delta n}{n_0} < 10^{-10}$.

In principle, the fiber and mirrors that constitute the cavity should be axisymmetric and thus show no birefringence. However, the narrow linewidths of the cavity resonances and their associated strict birefringence limitations mean that small amounts of birefringence (e.g. due to stresses or minor fabrication imperfections) are enough to prohibit sufficient polarisation degeneracy. This was solved by putting a polarisation controller inside of a fiber cavity.

This may seem somewhat counter-intuitive, using a polarisation controller to construct...a polarisation controller, but its not. These manual polarisation controllers induce birefringence by changing the applied stresses inside of a fiber thus it is possible to use one to cancel any of the resonator's intrinsic birefringence. All polarisation controllers are then left unchanged for the demonstration of all-optical polarisation control.

3.4 Experimental setup

A schematic of the experiment is shown in Fig. 3.9 which can be split into three parts:

- The fiber cavity (red shaded area).
- Preparation of linearly polarised input light (left of the cavity).
- Monitoring of the cavity polarisation state (right of the cavity).

3.4.1 Fiber cavity

The cavity is made of a 2-m-long single-mode fiber set inside a manual polarisation controller. The ends of the fiber are connected to fiber Bragg mirrors creating

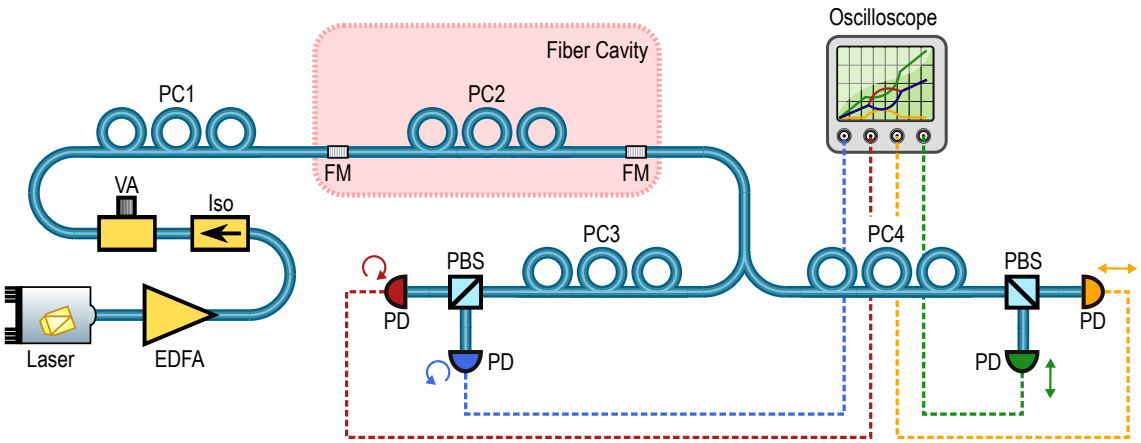

Figure 3.9: Experimental Schematic. A high-finesse Fabry-Pérot fiber cavity is realised by connecting an optical fiber on both ends to fibers with dielectric Bragg mirror stacks (fiber mirror, FM). To attain degenerate polarisation modes, a polarisation controller (PC2) is placed within the cavity, which is used to cancel any birefringence in the fiber and mirrors. Light is sent into the cavity from a tunable diode laser via an erbium-doped fiber amplifier (EDFA) with an isolator (Iso) to prevent back reflections. A variable attenuator (VA) is then used to control the power of the input light and its polarisation is set by polarisation controller PC1. The output of the cavity is split by a 50:50 fiber coupler and each branch is directed to photo-diodes (PD) via PC3 and PC4 and polarisation beam splitters (PBS). These final PCs are used to map the cavity's polarisation states to the PBS such that the PDs each monitor a distinct polarisation mode of the resonator. Schematic figure adapted from Ref [68].

a high-finesse cavity ($F \approx 140$) with very narrow linewidths ($\delta\nu \approx 0.40$ MHz, $Q \approx 4.9 \times 10^8$). Even though the finesse is already high, these parameters could be further improved by directly depositing the mirrors on both ends of the fiber to form a cavity, minimising losses at the connector.

3.4.2 Preparation of linearly polarised input light

In the experiment, light from a tunable diode laser is amplified by an erbium-doped fiber amplifier (EDFA), before being sent through an isolator to minimise unwanted effects from back reflections of the fiber cavity. The output polarisation of the EDFA changes with power due to thermal effects, so the power input to the cavity is instead controlled using a variable attenuator which maintains polarisation across the required power range. Finally, the input polarisation is set to linear by a polarisation controller (see section 3.4.4) before entering the cavity. This polarisation state is henceforth defined to be the vertical polarisation direction.

3.4.3 Monitoring the cavity polarisation state

The last two sections describe how a polarisation degenerate cavity is set up with a vertically polarised input (section 3.4.4 will detail how this was achieved), but we wish to see how the polarisation state of the cavity field develops. To achieve this, photodiodes are used to monitor the outputs of a polarisation beam splitter (PBS). However, this does not immediately work - this will monitor the polarisation

components in the PBS's basis rather than any basis corresponding to the cavities polarisation state (bends and stresses in the fiber after the cavity will rotate these polarisation states as they travel through the fiber). To account for this, a polarisation controller is used before the PBS to map the required cavity polarisation bases onto the PBS basis such that the intensity of the outputs gives a measure of the associated intensity of the cavity polarisation components.

This is done twice - a beam splitter divides the output field such that the clockwise/anti-clockwise circular basis and vertical/horizontal linear basis can be monitored simultaneously.

3.4.4 Polarisation controller alignment

The following approach was used to adjust the polarisation states during the measurements. In reference to Fig. 3.9, first, the polarisation controllers PC1 (input) and PC2 (intracavity) are aligned. For the alignment, the laser is swept across the resonances. This is done at sufficiently low optical power to observe the resonances as Lorentzian lines without nonlinear or thermal broadening of the modes. In general, birefringence inside the cavity leads to two polarisation modes with different associated resonance frequencies, which manifests as two distinct peaks in the photodiode output during a laser frequency sweep. By adjusting PC2, residual birefringence in the fiber cavity is compensated and moves the resonance frequencies of the two polarisation modes closer together, while it is simultaneously ensured (by adjusting PC1), that light couples equally into both polarisation modes. Adjustment of a single degree of freedom of the polarisation controller leads to an avoided crossing as described in section 3.2.4 and so the process is iterated using both degrees of freedom of the controller until the polarisation modes are close enough to be considered degenerate (i.e. the difference in the resonance frequencies is negligible in comparison with their linewidths). In addition, it is confirmed that the two polarisation modes have the same longitudinal mode number by examining the mode overlap across multiple resonance pairs within the tuning range of the laser (Toptica CTL1550 external cavity diode laser [ECDL] - range from 1510 nm to 1630 nm).

In the next step, PC1 and PC3 are adjusted in order to detect the left- and right-circular polarised output light. The laser output power is set sufficiently high, such that symmetry breaking will occur for linearly polarised input light. PC3 is adjusted until the signals from the photodiodes for left- and right-circularly polarised light are as symmetric as possible. There is then an iterative process in which PC1 is adjusted, followed by a corresponding adjustment of PC3 to keep the signals as symmetric as possible. As PC1 nears the correct state - such that its output is linearly polarised - the onset of symmetry breaking is apparent from the PD signals. Fine tuning of PC1 and PC3 is then used to optimise the system until the biggest possible symmetry breaking "bubble" is observed.

Finally, PC4 is adjusted in order to detect the horizontal and vertical polarisation states. For this, the linear input polarisation state is defined as being vertical. At input powers below the symmetry breaking threshold, the output light is expected to be vertically polarised and no horizontally polarised light exits the resonator. Accordingly, the input power is reduced with a variable attenuator that does not affect the polarisation state. PC4 is iteratively adjusted until the signal on the horizontal photodiode vanishes. This has now mapped the cavity vertical and horizontal

polarisation states onto the second PBS, such that the PDs monitor these cavity components. The experiment is performed immediately after adjusting the polarisation controllers to minimise polarisation drifts induced by temperature changes in the laboratory.

3.5 Results

The most telling demonstration of symmetry breaking is with a frequency sweep across a resonance for different input powers (with the input polarisation set to vertical, as described in the previous section). This shows how the system behaves symmetrically at low input powers, but above some threshold there is a region - which has been affectionately dubbed the "bubble" due to its visual appearance in these traces - of symmetry breaking. This was achieved in practice by simply sweeping the output frequency of the laser via piezo control of its external cavity and can be modelled theoretically by parameterising Eq. (3.2) in terms of detuning (α) for a given input power.

Figure 3.10 shows these experimental results along with equivalent theoretical predictions, which qualitatively agree. It can be seen that for low input power, the system responds symmetrically: both the circular polarisation states (CW: red, CCW: blue) equally couple through the cavity throughout the frequency sweep which in the vertical-horizontal basis is seen as the light being purely vertical - with no horizontal component - throughout.

At higher input powers - specifically above ≈ 7 mW - we see symmetry breaking by the emergence of a bubble (middle column of Fig. 3.10). This bubble occupies a region of detuning in which one circular polarisation component has a higher intensity than the other. In the linear basis, this bubble manifests as a dip in the otherwise smooth increase of the intensity of the vertical polarisation, with an associated "generation" of horizontally polarised light (N.B. this is not truly generation of light in this polarisation, rather the suppression of one component in the circular basis, which appears as a spontaneous generation of horizontally polarised light). The depth and breadth of this bubble increases with increasing input power, with associated increases in the relative intensity of the horizontally polarised light.

The main difference between the theoretical and experimental results is the lack of tilting of the experimental lineshapes. The theory shows resonances that are tilted to the right, giving an almost triangular lineshape, which was previously explained as being due to the intensity dependent refractive index pushing the resonance to the right with increasing coupled power. The fact that this is not seen in experiment is due to a competing (likely thermal) nonlinearity which opposes this effect and can been seen in other fiber cavity experiments [86].

The maximum input power was limited by parasitic nonlinear effects, which limited the region of parameter space that was investigated. At higher powers, high frequency oscillations were seen in the traces, which was assumed to come from four-wave mixing (FWM), stimulated Raman scattering (SRS) or stimulated Brillouin scattering (SBS). Accordingly, some of the field was sent to an optical spectrum analyser (OSA) for analysis, shown in Fig. 3.11. Traces were taken at low, and high (but sub-oscillation threshold) powers to determine the response of the OSA and show similar shapes. However when the cavity was in its oscillatory state, a

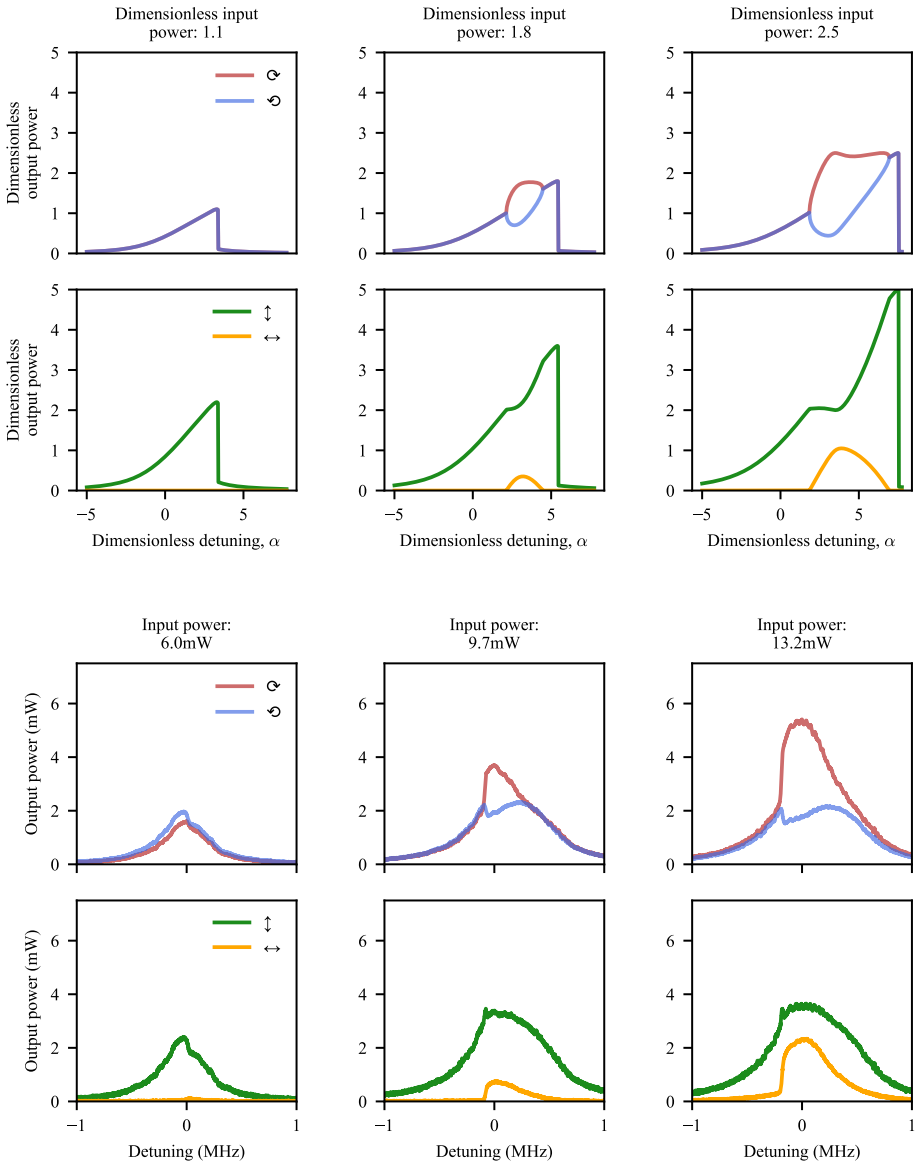

Figure 3.10: Theoretical and experimental traces of a frequency sweep across a resonance for different input powers. The upper half shows the solutions to Eq. (3.2) in both the circular (CW: red, CCW: blue) and linear (vertical: green, horizontal: yellow) bases. The lower half shows the measured traces for such frequency sweeps in these bases, with input powers roughly equivalent to those normalised values associated with the panels above. Qualitatively, these plots broadly agree, with the main difference being the lack of tilting of the resonances due to the Kerr effect, which is likely due to a thermal nonlinearity countering these effects.

peak between $10-20$ GHz *below* the pump frequency is seen with associated peak at *higher* frequency. FWM processes would be symmetric about the pump, having peaks both below *and* above it in frequency, and SRS has a gain band terahertz away from the pump. SBS however has a gain around $10-15$ GHz in fiber [104] so it appears as if this parasitic nonlinearity arises from Stokes Brillouin scattering. The length of this cavity gives it a small FSR (≈ 55 MHz) giving a high likelihood

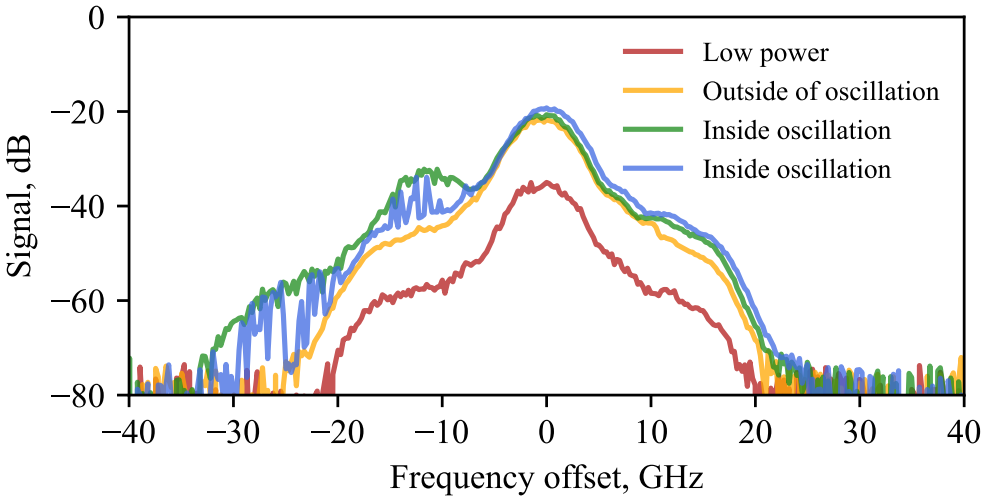

Figure 3.11: Optical spectrum analyser traces of the cavity field when oscillations in the experimental traces both are, and are not, present. The oscillations appear to be due to Stokes scattering into modes separated from the pump by $10-20$ GHz*, indicative of Brillouin scattering.*

of a cavity mode being present in the Brillouin gain region. This is exacerbated by the relatively high bandwidth of the Brillouin effect in fiber (up to 100 MHz [104]), making it difficult to mitigate in such an experiment.

3.5.1 All-optical Polarisation Control

The symmetry breaking effect here described can be used to make an all optical polarisation controller. The concept is as follows: light enters a cavity as described above that has a very small level of birefringence. This breaks the symmetry of the system, giving a preferred handedness of the cavity for a given detuning such that it behaves deterministically with no spontaneous "choice" of the output state.

In this regime, the handedness of the output light is determined by the splitting of the resonance frequencies for both circular polarisation components, which in turn depends on the input intensity. Fig. 3.12 gives a schematic for such a device, along with the results from an experimental demonstration at different input powers.

3.6 Conclusion

This chapter presents an all-optical polarisation controller based on the spontaneous symmetry breaking of degenerate polarisation modes in a fiber Fabry-Pérot cavity. A threshold power for symmetry breaking of 7 mW was observed, leading to a

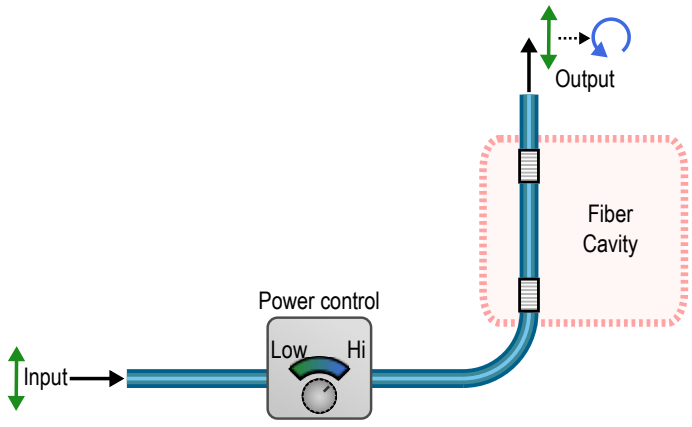

(a)

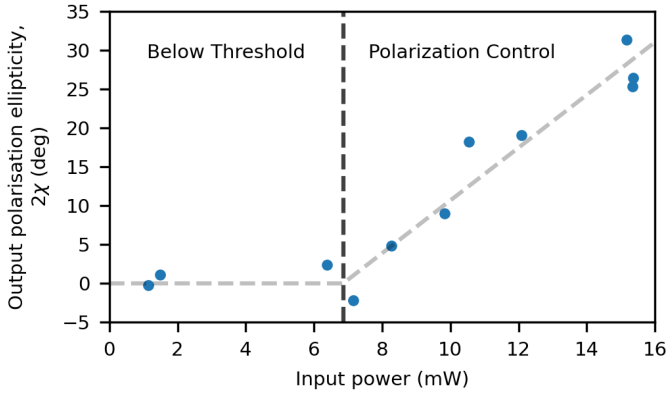

(b)

Figure 3.12: All optical polarisation control. a) Schematic of the concept. Linearly polarised input light is incident to a fiber cavity such that its input intensity determines the ellipticity of the output field. b) Experimental demonstration of all-optical polarisation control. Below some threshold power (≈ 7 mW) there is no symmetry breaking and so the output light remains vertically polarised. Above threshold, the ellipticity of the polarisation is determined by the input power.

maximum ellipticity of the output polarisation of 30°. The polarisation controller could find application in photonic circuits for which fabrication methods for current such controllers are not suitable, and more generally the symmetry breaking effect could be used in information processing and sensing applications.

3.7 Outlook

The equivalence between the symmetry breaking here described and that between counter-propagating light in WGM resonators implies that there is substantial further work that can be completed with these cavities. This work can be furthered in three main areas:

- **Information processing**. Chapter 4 follows the work completed in Ref [105] which utilises the Kerr induced splitting of degenerate counter-propagating modes of a WGM resonator to perform Boolean logical operations. Together with Ref [99], which uses the same effect to demonstrate optical memories,

this work shows how information processing is possible with the information carrier being the propagation direction of light. This work could be replicated in the polarisation degenerate cavities here discussed, with the information carrier now being the polarisation state of light.

- **Nonlinear enhanced sensing**. Ref [106] shows how the Kerr induced splitting can enhance the Sagnac effect[3], giving orders of magnitude improvement to the measurement of rotation - a promising route to the development of on-chip optical gyroscopes. Similar enhancements are feasible with the measurement of polarisation states, rather than propagation directions, for e.g. the measurement of the chirality of chemical/biological samples.

- **Chaotic polarisation state preparation**. This chapter has focused on steady-state solutions to the coupled nonlinear system, however Refs [81, 97] have shown that, for certain input parameters, self-switching and chaotic dynamics are possible. Chaotic systems show promise for use as random number generators [109] which are required for trustworthy data encryption and stochastic modelling [110–113]. The polarisation degenerate cavity discussed here could be explored in a chaotic regime similar to that of Ref [97], finding application as a random number generator for data security and simulation.

[3]The Sagnac effect is a relativistic optical phenomena in which two beams counter-propagating inside a rotating ring-cavity have a differential phase accumulation during one round-trip. Such a system was first used as a method for measuring rotation in Ref [107] and is now a common type of high-performance gyroscopes [108].

Chapter 4

Logic Gates based on the Kerr interaction of counter-propagating light in microresonators

4.1 Introduction

Fiber optic technology has underpinned the development of internet communications over the last few decades allowing the transmission of vast amounts of information with reduced latency. However, there are fears that internet latency and bandwidth limitations will slow progress in developing real-time applications, particularly for what is often referred to as the internet of things. Accordingly, methods to increase internet speeds are of great interest and one proposed solution is to reduce the latency associated with optic-to-electronic conversion at network nodes by keeping the signal in the optical domain [114, 115]. A photonic processor will instead be used to route the incoming signal to the correct output port [116], utilising optical logic gates in the process.

So why don't we simply use photonics processors? Indeed why don't we use optics as the information carrier in computing? Why are consumer electronics ubiquitous, but consumer photonics are unheard of? Simply: it's hard to process information using light. In general, information processing is a nonlinear process and so the physical system that underpins it must demonstrate nonlinearity. The advent of the transistor in the late 1940's as a nonlinear electronic element was an important milestone in the development of the electronics industry, however its photonic counterparts have been more difficult to develop due to the reluctance of light to interact with itself in a nonlinear manner.

Progress in photonic chip fabrication capabilities has led to a resurgence in interest in optical computing [117]. In particular, the ability to reliably and repeatedly fabricate nonlinear optical components on-chip with modest operation powers suggests that optical computing may be nearing real-world application. Such devices could broadly operate in three separate domains: as a counterpart to the archetypal

This chapter expands on work I wrote as first author in Ref [105]. Passages and figures from this original work conducted by myself may be directly adapted into this chapter where appropriate.

digital computer [118], in analog form (which has particular interest for machine learning applications) [119–121], and for quantum computation [30, 31, 122].

An important problem that can be solved with digital optical computing, which like its electronic counterpart uses an architecture of (classical) logic gates, is the on-chip routing of light [123, 124]. Much of the internet, along with high-power computing services, is hosted in large data centres with a vast array of distributed processors and memories [125]. Optical interconnects are used to transfer information within this expansive network as electronic transmission cables would operate too slowly and have prohibitive power requirements [126–129]. This communications network consists of many nodes at which an input optical signal is analysed in the electronic domain to determine which node it should be sent to next. Such optical-to-electronic (and electronic-to-optical) conversion requires power and leads to latency, which is a particular issue for distributed computing systems [130]. Instead, a set of optical logic gates could be used to facilitate this routing, improving the performance of distributed networks and computing [114–116, 131].

Whispering gallery mode (WGM) resonators [132] are a promising candidate for optical logic gate architectures as their high Q-factors and small mode volumes [133] allow for the required nonlinear optical phenomena for only modest input powers [36, 134]. Furthermore, such devices can be integrated on-chip using CMOS technology and made from a wide range of materials, ensuring scalability [135–137]. Optical logic gates have been previously demonstrated in WGM resonators, but with associated issues that would prevent easy integration into optical networks. These issues include: requiring multiple operation frequencies [138–146], needing electronic control [147–151] or requiring pulsed inputs [152].

Another possible architecture for all-optical switching is the Mach-Zender interferometer (MZI), which is studied extensively in Ref [153]. Here, an input signal is split into two spatial modes at a $50:50$ beamsplitter (BS), both propagating along their respective arms, before being recombined at a second $50:50$ BS. The nature of the BS interaction is that input signals that are completely in phase will both exit from one output port, while those that are in anti-phase will exit the other. Thus, having a control field in one arm of the interferometer can be used to control which port the signal exits from. A low intensity control field means that both arms lead to the same phase accumulation and exit one port. A high intensity control field modifies the phase accumulated in one arm via cross phase modulation (XPM) and thus the signal exits the other port. This was completed in fiber in Ref [153] and is especially useful in switching quantum signals for which loss is a major issue [154]. This method would be more difficult to apply to the on-chip routing of optical signals. Without the benefit of a resonator, the input powers and optical path lengths required are far greater to achieve the nonlinear phase modulation (also the frequency selective nature of cavities mean that the phase modulation required can be far below the value of π required for full switching in an MZI). Along with it being difficult to integrate long waveguides and high power lasers onto a chip, another issue is that both MZI arms need to be phase locked to each other which is difficult when they also have to be long. In contrast, a WGM resonator can be utilised in a purely intensity dependent manner, without the need to worry about phase locking.

In this chapter, an all-optical, universal logic gate is presented in which all signals operate at the same frequency in the telecom band. Being universal means that, with a sufficient number of these devices working in a suitable fashion, *any*

Boolean operation can be achieved. Furthermore, the fact that it has single frequency, continuous-wave operation and only requires passive optical elements makes this a uncomplicated and scalable device.

4.2 Concept

Chapter 3 detailed how orthogonally polarised states of light can mutually interact via the Kerr effect. In particular, cross-phase modulation (XPM) allows the resonance frequency of one mode to be dependent on the intensity of light in the partner mode. It will be shown in section 4.2.1 that counter-propagating modes in a WGM resonator also interact in this way, leading to a similar symmetry breaking effect as previously described [79].

Figure 4.1 shows how this effect can be used to demonstrate all-optical logic. Two fields are coupled into a WGM resonator, in opposite directions, using an input waveguide. Logical information - classical bits - are encoded onto these fields using their respective intensities: high intensity for logical state HIGH (1), low intensity for LOW (0). N.B. ket notation will be used to show that an optical field has *classical* information encoded into it: $|1\rangle$ implies a field with HIGH intensity corresponding to a *Boolean* value of 1. This chapter will contain no references to quantum information/states.

When input A is HIGH and input B is LOW - Fig. 4.1b) - the counter-clockwise (CCW) field is on resonance. Accordingly, the field couples efficiently into and through the resonator to a second, output, waveguide. In this situation, the output field (from the upper-left port) is HIGH.

However, when input B is also HIGH, this output is suppressed - Fig. 4.1c). In this situation, light couples into the clockwise (CW) mode, building up in intensity and modulating the refractive index of the CCW mode. The input field is no longer resonant, and so does not efficiently couple to the output port, which is now in logical state LOW. In order for this situation to work, the HIGH state associated with input B must be more intense than the corresponding HIGH state for input A. If not, this system can undergo the symmetry breaking that was observed in Ref. [79] (the counter-propagating equivalent to the polarisation symmetry breaking described in Chapter 3). This would lead to a randomness in the output of the logic gate, which would inhibit its intended application. Having the intensity of the HIGH state of input B to be greater than that of A forces the system to adopt the correct output in this situation, ensuring the correct logical operation.

Trivially, the output is LOW when input A is LOW as there is no incident light to couple into the CCW mode. Accordingly, the output is HIGH if and only if A is HIGH and B is LOW - equivalent to the $A \cdot \tilde{B}$ gate. This gate is universal (see section 4.2.2) and thus an arbitrary Boolean operation can be performed using only copies of this gate suitably cascaded. Moreover, low back-scattering in WGM resonators makes the counter-propagating modes degenerate meaning that all fields have the same frequency and can thus come from the same source - a useful property for scalable devices.

Another interesting property of this gate is that no information is destroyed. The prototypical logic gate has two input ports and only one output, thus the computation is irreversible with the destruction of 1 bit of information. According to Landauer's principle, this comes with a thermodynamic cost which will heat

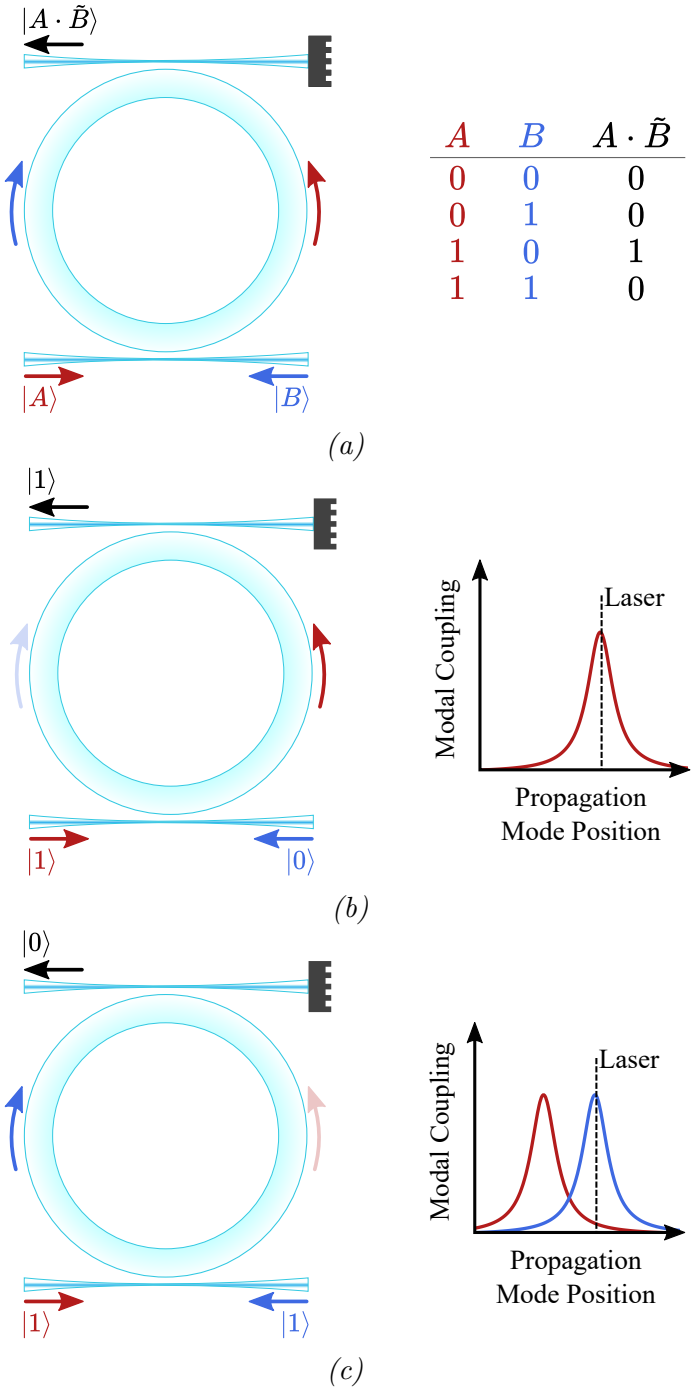

A	B	$A \cdot \tilde{B}$
0	0	0
0	1	0
1	0	1
1	1	0

Figure 4.1: Schematic for the concept of an all-optical logic gate. a) Inputs A and B enter a WGM cavity in opposite directions via an input waveguide. The cavity field couples to a second (output) waveguide such that the output is only HIGH *when input A is* HIGH *and input B is* LOW *- the $A \cdot \tilde{B}$ gate. b) When A is* HIGH *and B is* LOW *light couples through the cavity making the output* HIGH*. c) When input B is also* HIGH*, the Kerr effect modulates the resonance frequency of the counter-clockwise mode such that the output is* LOW*. N.B. Ket notation is used to denote the logical state of different parts of the system, but these states strictly define classical (Boolean) information.*

the circuit [155]. Instead, for the logic gate presented here, all of the system's information leaves the four ports of the input and output waveguides. Thus, there is no intrinsic heating with such a system as all unused outputs can be directed away from the circuit[1].

4.2.1 XPM of counter-propagating light

Section 2.3.6 detailed how the orthogonal circular polarisation bases exhibit nonlinear coupling via XPM. In particular, it was shown that the magnitude of this effect was twice that of SPM - this difference in magnitude being necessary for symmetry breaking. The same is the case for counter-propagating light in a WGM resonator, though the underlying theory is slightly different. The mode of a WGM resonator has a well defined polarisation, so Eq. (2.33), which gives the 3$^{\text{rd}}$ order electric dipole moment density, can be written more simply as:

$$P^{(3)} = \epsilon_0 \chi^{(3)} E^3, \tag{4.1}$$

for an applied field E. This field is now made of two counter-propagating components $E_{\text{(c)cw}}$ for the (counter-)clockwise directions, so the total field is:

$$E = E_{\text{cw}} e^{i(kz+\omega t)} + E_{\text{ccw}} e^{i(-kz+\omega t)} + c.c, \tag{4.2}$$

for CW propagation direction z.

Accordingly, Eq. (4.1) has 64 terms, though many of these include high order terms in both k and ω which is beyond the scope of this work. The remaining terms are:

$$\begin{aligned} P^{(3)} = 3\epsilon_0 \chi^{(3)} \big(&\left[|E_{\text{cw}}|^2 + 2\,|E_{\text{ccw}}|^2 \right] E_{\text{cw}} e^{i(kz+\omega t)} + \\ &\left[|E_{\text{ccw}}|^2 + 2\,|E_{\text{cw}}|^2 \right] E_{\text{ccw}} e^{i(-kz+\omega t)} \big) + c.c. \end{aligned} \tag{4.3}$$

This shows the same nonlinear coupling between counter-propagating modes in a WGM as was discussed in the previous Chapter for polarisation modes - the reason why symmetry breaking is observed in both.

4.2.2 Universality of the $A \cdot \tilde{B}$ gate

The universality of a logic gate - its ability to implement any Boolean operation without requiring the use of another type of gate - is a valuable property. The lack of reliance on other devices allows scalable production and straightforward operation. However - the famous universal gates are the NAND and NOR gates, is the $A \cdot \tilde{B}$ gate also universal?

There is a useful property of universal logic gates: if multiple copies of one type of logic gate can be arranged to mimic the operation of another *universal* logic gate, that gate too is universal. This method can show the universality of the $A \cdot \tilde{B}$ gate.

First, it is important to note that a constant input of logic value 1 to the A port of the $A \cdot \tilde{B}$ gate just gives the $\tilde{B}$ gate (the NOT gate).

Second, putting this output into the B port of a second $A \cdot \tilde{B}$ gate simply gives the AND gate - the original B input has been inverted twice.

[1]It should be noted that material absorption will still lead to heating.

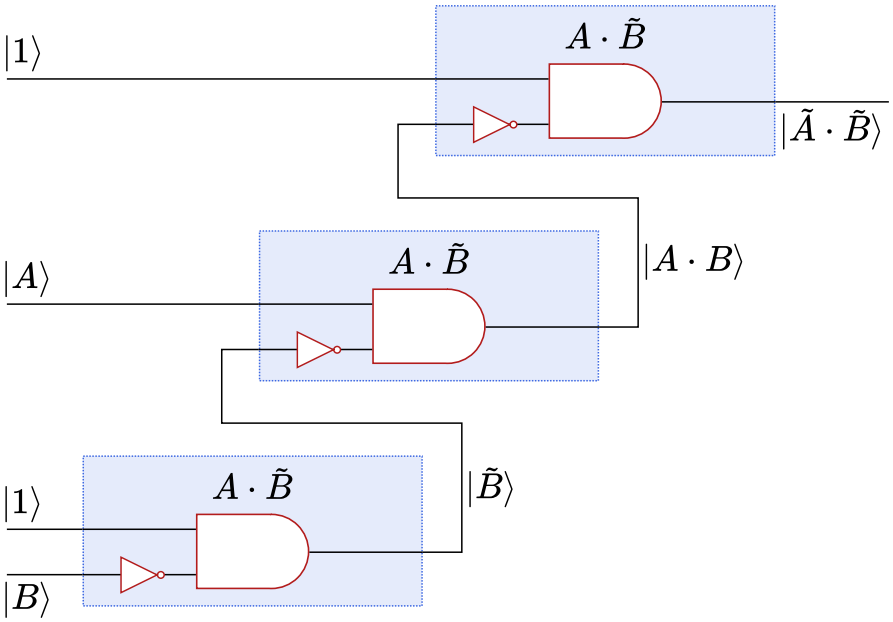

Figure 4.2: Proof that the $A \cdot \tilde{B}$ gate is universal. Using only 3 $A \cdot \tilde{B}$ gates (blue rectangles), it is possible to make the universal NAND gate, thus proving that $A \cdot \tilde{B}$ too is universal. This proof relies on the fact that a constant logical 1 input to the A port of the gate turns it into a NOT gate.

Finally, this output can itself be inverted by a further $A \cdot \tilde{B}$ gate - using a logic 1 in the A port to give the NOT gate previously described. These three $A \cdot \tilde{B}$ gates, with two additional constant logic 1 inputs, mimic the NAND gate, proving the universality of $A \cdot \tilde{B}$. Fig. 4.2 gives a circuit diagram of this proof.

4.3 Experimental Methods

This section details the experimental work that was done to demonstrate optical logic gates. It starts with a description of how a resonator with low intrinsic backscattering was chosen to avoid resonance splitting, how an EOM overdrive was used to get the correct input waveforms before a detailed description of the experimental setup and methods used.

4.3.1 Backscattering

The operation of the logic gate requires both counter-propagating modes to be frequency degenerate at low powers, such that the only splitting of these resonances arises from a difference in the input powers. This idea is analogous to that described in Section 3.2.4, where the low-power splitting of resonances was explained to be a consequence of the linear coupling between modes. For polarisation, this coupling is due to birefringence (non-diagonal elements of the $\chi^{(1)}$ tensor), but for counter-propagating modes it arises from *backscattering*.

Backscattering occurs due to the presence of Rayleigh scatters within the optical mode. Some proportion of this scattered field is guided in the counter-propagating mode of the resonator thereby linearly coupling the two modes [156]. The scattering can be caused by defects in the resonator material or geometry, and the presence

of the tapered fiber in the evanescent field of the optical mode. The resonator and tapered fiber position were chosen such that, at low power, the counter-propagating modes were frequency degenerate, with the low intrinsic backscattering in rod resonators making this a relatively painless process.

4.3.2 EOM Overdrive

The logical state of the inputs is encoded into their respective intensities, with fiber-coupled EOMs (Thorlabs LN81S-FC) used to independently modulate these values. These modulators utilise a Mach-Zender interferometer made up of Lithium Niobate ($LiNbO_3$) waveguides. Electrical signals are input to electrodes spanning these waveguides, which leads to a relative phase mismatch between both arms of the interferometer via the strong Pockels effect in $LiNbO_3$. This phase mismatch leads to an interference at the interferometer output such that the output intensity is a function of the electrical input.

An ideal demonstration of optical logic would employ inputs that quickly switch between the HIGH and LOW input states in a square-wave like fashion. This allows the highest switching speed of the logic gate to be realised, and so showing its strongest performance.

Charging phenomena, e.g. due to the capacitance across the electrodes, leads to a finite rise time for the EOMs. This manifests as damped response in the output optical fields intensity in comparison to the input electric signal. This was accounted for as best as possible in the experiment by overdriving the input signal - an input square wave is instead replaced by an input that overshoots the intended voltage, decreasing to this value exponentially in time such that the output intensity better approximates a square wave. This initial overshoot acts to speed up the charging phenomena to get to the steady state value quicker.

4.3.3 Relative input powers

As previously discussed in Section 4.2, correct logical operation is ensured when both input states are HIGH by having the intensity of input B in this situation be greater than that of input A. The aforementioned use of EOMs to independently control the intensities of both inputs was used to ensure this: both inputs were modulated by the same amount, with A going from near zero power in the LOW state up to this maximum value for the HIGH state, whereas input B had some positive offset in both situations. Experimentally, this is simply a DC difference between the electrical signals to both EOMs respectively

The input powers, $\tilde{p}$, in both propagating directions are given in terms of the modulation amplitude and offset as:

$$\tilde{p}_{\mathrm{ccw}} = P_m A, \tag{4.4a}$$

$$\tilde{p}_{\mathrm{cw}} = P_m \left(B + \zeta\right), \tag{4.4b}$$

where $A, B \in \{0, 1\}$ are the logical inputs, P_m is the dimensionless input modulation amplitude and $\zeta \in (0, 1)$ is the modulation offset as a proportion of P_m.

The EOMs set the absolute power limitation on the experiment. They are rated up to 100 mW input power, with an expected insertion loss of -4 dB. They were however used up to a maximal output power of 50 mW before the author became too nervous about potential damage to the device.

4.3.4 Hysteresis

Alongside symmetry breaking, another nonlinear phenomena that can inhibit the correct logical operation is hysteresis. Hysteresis is the dependence of a system on not only its instantaneous inputs, but also on the history of the system itself. In some sense, such a system has developed a memory - and indeed this system has been shown acting as an optical memory during the completion of this thesis in Ref [99].

A logic gate should be sensitive only to its current input state, with no regard for its own history. The issue that could manifest from hysteresis is that correct state changes are inhibited. In this system, such hysteresis can be imagined in the following example: input A is HIGH and B is LOW such that the cavity field develops a strong dominance in the CCW direction. When input B is increased to the HIGH state, the CW direction *should* now dominate. However one can imagine that the original dominance of the CCW direction is so strong that input B cannot couple in regardless of how intensely it is pumped. Such a system would remain CCW dominant even when both inputs are HIGH, counter to the truth table in Fig. 4.1.

To ensure experimentally that this is not the case, the inputs were modulated such that each state change should be seen. Not only were each of the four rows of the truth table investigated, each of the twelve possible transfers between them were tested also. Hysteresis was deemed to be negligible when the output intensity was correct (based on the current inputs) regardless of the previous state.

4.3.5 Experimental setup

A schematic for the experimental setup is given in Fig. 4.3. Light from an ECDL at 1550 nm is split into two branches which each serve as the inputs A and B respectively. An EOM is used in each branch - as described in section 4.3.2 - to give the correct waveforms for these inputs. The nonlinear crystal inside the EOM is polarised and so includes a built-in polariser and is coupled to an aligned polarisation maintaining (PM) fiber. Accordingly, to maximise throughput through the EOM, the input polarisation must be matched to that of the PM fiber. This is achieved using a fiber polarisation controller before the EOM.

After the EOM is a further polarisation controller, which is used to match the input polarisation to that of the resonant mode under investigation. In order to reduce the drifts in polarisation state that can arise from fiber bending, they are taped to the optical table to minimise movements. An optical isolator follows from this polarisation controller to ensure that the counter-propagating light does not enter the EOM/ECDL.

The light is then sent to a tapered fiber, via a $99:1$ beamsplitter. The beamsplitter allows for the majority of the light to be sent to the resonator via the tapered fiber. A small amount of light is sent to photodiodes to monitor the intensity input to, and transmitted through, the tapered fiber which can be used to discern whether the input is resonant with the cavity.

The tapered fiber is mounted onto an aluminium bracket for structural robustness. This bracket is then fixed onto a three-axis translation stage (Thorlabs NanoMax) which allow for sub-micron positioning of the tapered fiber. With the laser frequency sweeping, this tapered fiber is brought close to the WGM resonator with the help of a set of microscopes. Dips in the transmission through the taper

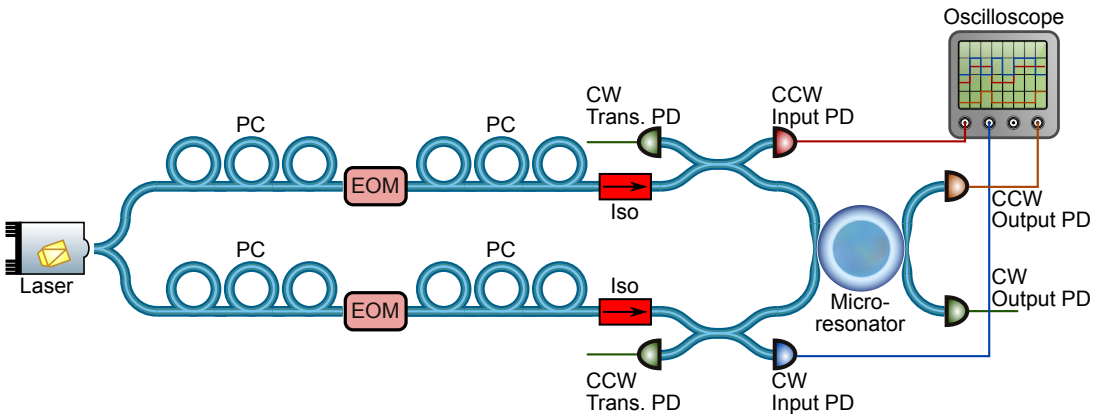

Figure 4.3: Experimental setup. A laser beam is split into two branches, corresponding to inputs A and B. Each input is independently amplitude modulated by a Mach-Zender electro-optic-modulator (EOM) and has its polarisation matched to that of the resonant mode using a polarisation controller (PC). They are then coupled in opposite directions into a fused silica microrod resonator via a tapered fibre, with directional couplers and photodiodes used to monitor the power input into and transmitted through the tapered fibre in both directions. A second tapered fibre is used to couple out the resonator field, and is attached to photodiodes to monitor the output.

indicate near-correct positioning of the taper as light is now coupling into the resonator. This position is then optimised: with the two directions in the plane of the optical mode controlling the degree of overlap between the evanescent fields of the resonator mode and tapered fiber. The final direction - along the tapered fiber axis - is used to maximise phase matching between both the tapered fiber and the resonator (the tapered fiber wave vector is a function of the taper width, which changes along this axis).

A second tapered fiber is coupled into the opposite side of the resonator. This is done by first simply swapping the taper that is connected to the rest of the setup and using the same method as for the first fiber. There are now two tapers connected to the resonator: an input and output. The coupling rates associated with both act as a source of (extrinsic) loss in the cavity and hence degrade the Q-factor. The output taper is positioned such that it is under-coupled, maintaining a high Q-factor of the cavity at the expense of the intensity of out-coupled light. This output taper is connected to photodiodes such that the output of the logic gate can be monitored.

4.3.6 Tuning into resonance

Logical operation requires the laser frequency to be locked to the resonator such that frequency drifts of either do not inhibit the correct logical operation. This was achieved using a passive thermal lock (see section 2.3.10) for which relative motion of the frequencies of the laser and resonant mode are countered by heating/cooling of the resonator.

Tuning into the resonance is done in the following process:

1. The modulation amplitude of the square-wave inputs to the EOMs are set to zero. Accordingly, the intensities of the inputs to the resonator in both

directions are constant in time. Moreover, these intensities are the same as the average value for a random binary sequence input i.e. setting $A = B = 0.5$ into Eq. (4.4). This last step reduces the effects of any thermal instabilities in the tuning process by maintaining the same average input power.

2. The laser frequency is scanned using piezo control. This allows the investigation of what resonances look like on an oscilloscope, which helps to find those with appreciable nonlinear effects.

3. A suitable resonance is selected. This is chosen as one in which there is a region in the resonator that has, for a range of detunings, a high suppression of the input A (due to the XPM from input B).

4. The amplitude of the laser frequency sweep is reduced to zero, using the DC offset of the piezo control to maintain the laser inside resonance. This is done such that the laser is on the thermally stable side of the resonance, thus mutually locking their frequencies.

5. The modulation amplitude input to the EOMs is increased to give the correct output. Even though the average power should remain the same during this procedure, this is done gradually to ensure there are no shocks to the system that could break the frequency lock.

6. Correct logical operation is confirmed. The output should be high only when input A is high and B is low. However this will not be optimised as the detuning between the laser and resonator is not ideal...

7. The DC offset to the laser piezo is adjusted to maximise the suppression of the output LOW state by optimising the detuning. The data is continually saved during this process to subsequently find the optimum suppression.

4.4 Results

The optimal experimental realisation of optical logic is given in Fig. 4.4. The upper panel shows the input waveforms (A: red, B: blue), with the lower panel showing the output. The inputs powers were modulated between $0-35$ mW for input A and $15-50$ mW for B ($P_m = 35$ mW, $\zeta \approx 0.4$).The input binary sequence can be seen to include every possible change of input state, with the output only being HIGH when A is HIGH and B is LOW - proving the correct demonstration of $A \cdot \tilde{B}$ logic.

4.4.1 Low state suppression

When both inputs are high, there is a residual output due to the incomplete suppression of input A (this can be seen in the output trace roughly between $0.5-1.0$ ms). The intensity associated with this state is suppressed by -11 dB in comparison to the (steady-state) HIGH value, the maximum value of suppression that was found experimentally.

This suppression is an important parameter for the realisation of cascaded logic - the output can be subsequently amplified and fed into further logic gates, with a high suppression ensuring that a LOW state input into a subsequent logic gate

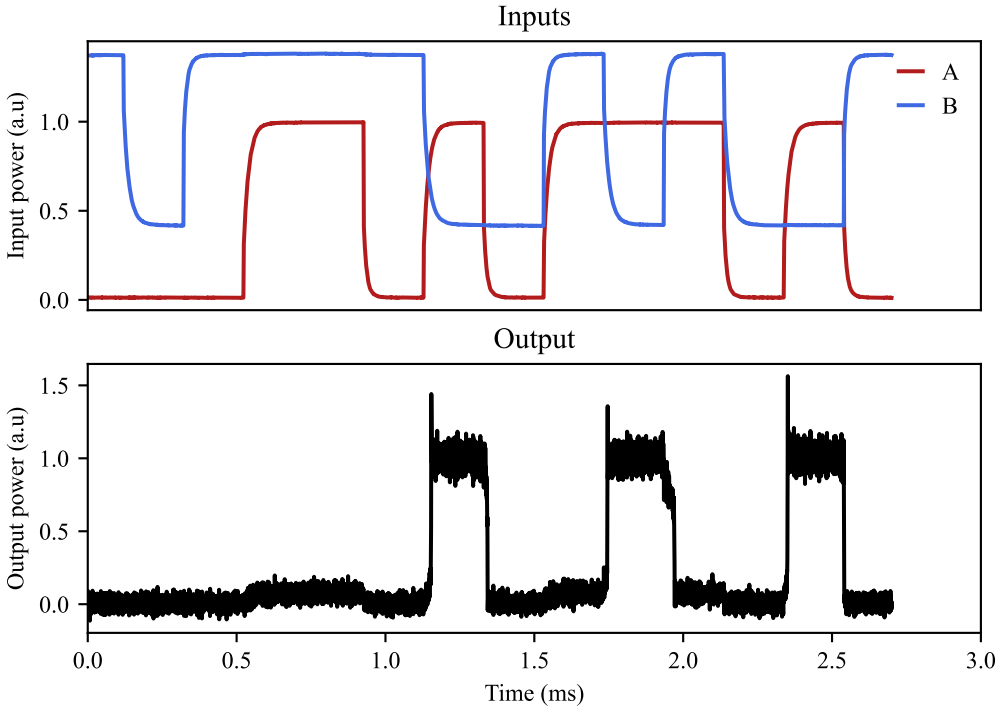

Figure 4.4: Demonstration of the all-optical logic gate. The upper panel shows the measured powers input into the tapered fibres in both directions. Inputs A and B are both amplitude modulated by the same amount, but with B having a positive offset in order to suppress the output when both inputs are HIGH*. The lower panel shows the measured output field, which can be seen to be* HIGH *only when input A is* HIGH *and input B is* LOW*, showing the correct operation of an* $A \cdot \tilde{B}$ *gate. When both inputs are* HIGH *the output is not fully suppressed, which can be seen by the slight increase between* 0.5 *and* 1 ms*. This residual power and the proper output power together characterise the suitability of the logic gate to be cascaded, with a low residual power and a high signal power being optimal.*

does indeed have a low intensity. Accordingly, the maximum possible values are investigated theoretically in section 4.5.

4.4.2 Output power

For cascaded logic, with subsequent gates that are identical to the first, the output power from the gate should be equal to that of the original inputs. This would require perfect throughput efficiency between the input and output ports, which is impossible with a lossy resonator.

Instead, there will be some loss associated with this device, which can be minimised by strongly over-coupling both the input and output waveguides. However this over-coupling, which acts as increased losses inside of the resonator, will degrade the Q-factor and hence require stronger input powers to achieve the same amount of nonlinear suppression.

Instead, cascaded logical operation can be achieved by using an amplifier after each logic gate, to keep the input powers to subsequent gates the same. This

amplification could be performed by, for example, an erbium doped amplifier, or a semiconductor optical amplifier (SOA), both of which have been demonstrated on-chip [157, 158]. There would then be a compromise made between the input power requirements and throughput efficiencies available (setting the demands on the subsequent amplifier input powers) which would determine the ideal coupling rates for the input and output waveguides.

4.4.3 Operation speed

Another important parameter for any logic gate is its speed of operation. This device is ultimately limited by the cavity lifetime, though this demonstration is limited by the rise time of the EOMs (which was minimised using the method given in section 4.3.2). The slowest switching speed of ≈ 0.05 ms (20 kbps) is limited by the rise time for input B at ≈ 1.95 ms[2].

With ideal input switching, the device would still be limited by the resonator lifetime to a possible bitrate of ≈ 1 Mbps. This is still significantly lower performance than that required for most telecomms applications, but the use of chip-integrated silicon nitride resonators (the higher associated nonlinearity allow for a lower Q-factor/response times) could allow for the required Gbps operation at milliwatt input powers [99].

4.5 Maximum low state suppression

The experimental demonstration of -11 dB seemed optimal for the power limit of 50 mW per input, though this had not been confirmed theoretically. This was done using a time-step simulation of Eq. (3.1), with input powers modulated as per Eq. (4.4).

This leaves three free parameters to optimise the suppression: the modulation amplitude (P_m), the modulation offset (ζ) and detuning between the laser and cavity (α). The detuning can be fixed in terms of the other two by maximising the cavity intensity associated with input B, meaning the optimisation of the suppression is now a two dimensional problem.

Figure 4.5 shows the results of this simulation for different values of the modulation amplitude and offset. The main panel shows a colourmap of the suppression (in dB) for these different parameters, with stronger suppression being associated with higher modulation amplitude/offsets. This trend - which is expected: higher intensities leading to greater nonlinear splitting - does not persist with arbitrarily high powers. The white-space in this panel is indicative of the inhibition of correct logical operation due to hysteresis.

The action of hysteresis is shown in the right panels of Fig. 4.5. These are the results of a time-step simulation for logical inputs with a binary sequence as given in the upper two plots. The remaining three plots: I), II), and III), give the (normalised) output intensity for these logical inputs with a modulation offset $\zeta = 0.4$ and different modulation amplitudes, with the corresponding points shown in the main panel.

[2]N.B. The actual demonstrated value of ≈ 5 kbps is lower than this value though this is simply to make the demonstration of optical logic clearer for the reader.

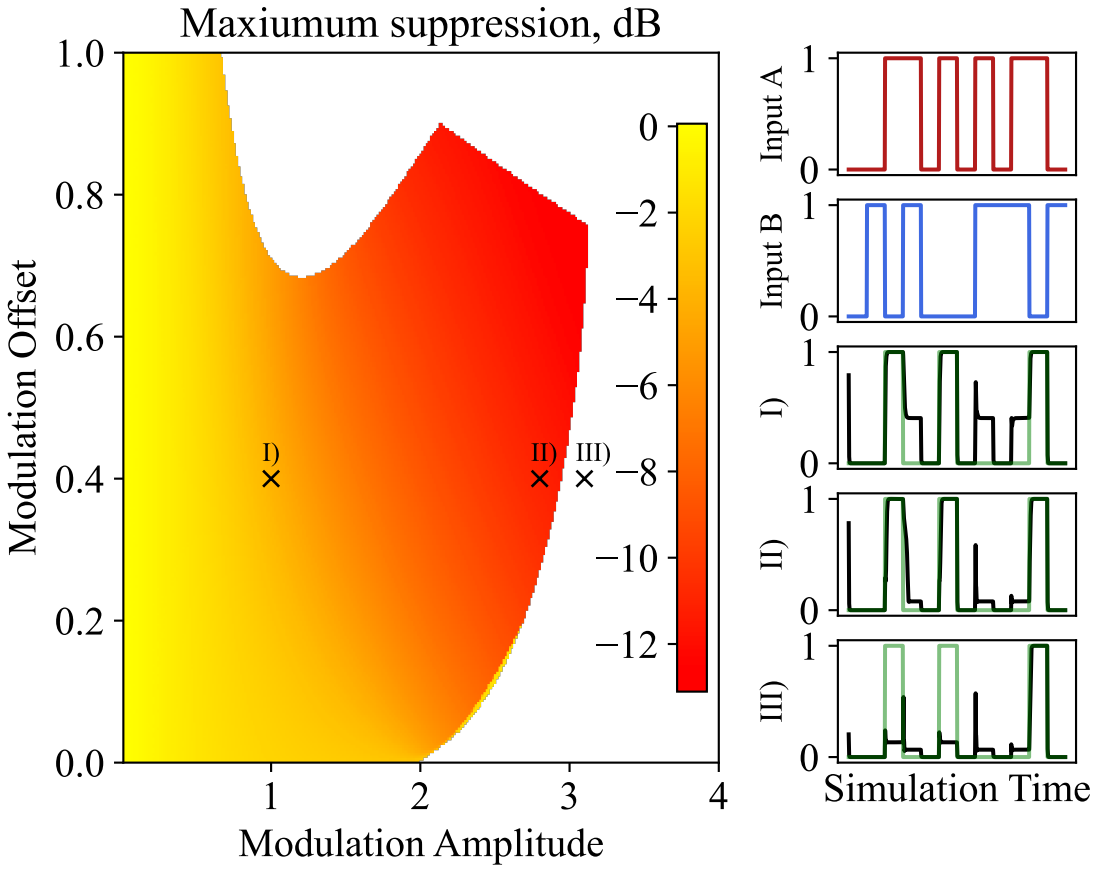

Figure 4.5: Maximum available suppression. Main panel: suppression of LOW *output state for different dimensionless modulation amplitudes and offsets in* dB*. Low values indicate suitability for cascaded operation, which is improved for higher input modulation amplitudes and offsets up to a maximum of* -13 dB *at* $P_m \approx 3.1$, $\zeta \approx 0.75$*. The whitespace shows the regions for which the inability to correctly access all states inhibits the operation of the logic gate. Upper right panels: inputs A and B for the timestep simulation presented below. (I)-(III) Simulated output for different modulation amplitudes at a modulation offset of* $\zeta = 0.4$*. For low amplitude (I) the output is only suppressed to roughly* 3 dB *of its maximum value. This suppression improves with a higher modulation amplitude (II), but eventually the system stops behaving suitably (III): for sufficiently large input powers there are instances where the output state should be* HIGH *but it cannot reach this state because of hysteresis in the system.*

Panel I) shows the correct logical operation, but with low suppression. The output intensity is always similarly high when A is HIGH and B is LOW, but the output is still relatively intense when both inputs are HIGH. Panel II) also shows correct operation, though with better suppression associated with this higher modulation amplitude. Panel III) however no longer operates correctly as a logic gate. The first two occasions for which the output should be HIGH (perfect operation shown by a green line) are not.

This shows that the performance of such a device has two competing reactions from increasing the intensity input to the cavity. On the one hand, the higher asso-

ciated nonlinearity leads to a greater suppression that will be helpful for cascaded logical applications, though increasing this eventually leads to a hysteresis that inhibits the correct operation. Such compromises would need to be made when integrating such a device into a wider photonic circuit and could be avoided by having a circuit that does not have a full duty-cycle (i.e. both inputs return to zero between each logical operation) to get arbitrarily high suppression with no hysteresis, though this would entail its own operational complexity.

4.6 Conclusion

This chapter presents an all-optical, universal logic-gate based on the nonlinear resonance splitting of degenerate counter-propagating modes in a WGM resonator. Near optimal relative LOW state suppression of -11dB was achieved. Operational speeds were limited to 20 kbps by auxiliary experimental equipment, with the device predicted to be able to operate up to 1 Mbps. In principle, such a system could be integrated onto a photonic chip to operate at Gbps speeds with sub-mW input power, finding application in the on-chip routing of optical signals in telecoms and data-centres.

4.7 Outlook

This chapter has detailed the first demonstration of universal optical logic based on the interaction of counter-propagating light in microresonators, however to be genuinely useful (e.g. in telecomms/data centre applications) further developments are required:

- **Cascaded logical operation.** Real-world applications require many logic gates working in parallel and series to make useful devices. This would require a high degree of repeatability in fabrication, or active control mechanisms to tune the resonance frequency of each device, to ensure that there is a common frequency that is appropriate for all logic gates. The issues associated with throughput efficiency and post-gate amplification would also need to be addressed to ensure that there is sufficient input power to subsequent logic gates.

- **Chip integration.** The current performance characteristics of the device - operating speed and power requirements - are insufficient for use in most applications. The Gbps, sub-mW performance expected from photonic chip integration [99] would make this concept a viable technology. Chip integration could eventually allow for the fabrication of complex circuits consisting of many such devices all working in concert

- **Explore different information carriers.** The state of the logic gate presented in this chapter is provided by the propagation direction of the field inside the resonator. One can imagine using the same concept - of using cross-phase modulation to shift resonance frequencies - for different components of an optical field. Indeed, such a system was explored in Ref [141] for fields with different frequencies, with the logical state set by the dominant frequency.

One could also imagine expanding the work of Chapter 3 to encode the logical information in the intensity of a circular polarisation component of the field. E.g. a logical HIGH value could be represented by a clockwise handed polarised field of high intensity (LOW otherwise). Sending such a field to an output port via a polarisation degenerate Fabry-Pérot cavity, as in Chapter 3, would lead to a HIGH output. This process would be hindered by the presence of a secondary high intensity input field of anti-clockwise handed polarisation due to cross-phase modulation shifting the resonance frequency. The output field would now have a suppressed clockwise polarised component - the logical LOW state. Thus, again the system would act as an $A \cdot \tilde{B}$ gate

Chapter 5

Multi-partite continuous-variable entanglement in a Kerr-frequency comb

5.1 Introduction

Fundamentally, optical fields are quantum mechanical in nature. In contrast to the simplest quantum system, the spin, which exists in a binary state on a two-dimensional Hilbert space, optical fields are described by continuous variables in an infinite dimensional Hilbert space. Similarly to classical information theory, quantum information can be encoded in discrete systems, with the quantum equivalent of the *bit* being the *qubit*, and in continuous systems, with the quantum equivalent of such a signal often called a *qumode*.

Photonic systems are a promising architecture for the generation and manipulation of both discrete and continuous variable quantum information [30]. In comparison to other quantum information architectures, photonic systems can be transported with low losses either in free space or optical fiber. These advantages, along with the the ability to use linear optical elements to perform arbitrary unitary operations [159, 160], make photonics an exciting platform for the three main areas of quantum technology: computation, (secure) communication, and sensing.

In particular, nonlinear optics provides a way to turn the classical coherent states that are output from a laser into "squeezed" states. Quantum optical states can be described by their associated amplitude and phase (and equivalently as quadrature variables), which are conjugate variables and thus obey Heisenberg's uncertainty relation. For coherent states, the uncertainty in both of these operators is equal, but squeezed states will sacrifice uncertainty in one operator for improved knowledge of the other. Squeezed states are examples of Gaussian states but, in general, the Kerr-effect leads to the generation of non-Gaussian states [161]. Under certain approximations (see section 5.2.3), degenerate, spontaneous, four wave mixing can be treated as a form of two-mode squeezing - generating a non-classical state of light

This chapter describes unpublished work-in-progress which is intended to be developed into a journal article. Accordingly, rather than giving a comprehensive literature review, the aim is to highlight the key literature that contextualises the work here presented.

[53, 162–164]. Importantly, for Gaussian states, multi-modal *squeezing* is equivalent to multi-modal *entanglement* [165].

The quantum nature of frequency combs has been well studied in the literature, specifically for $\chi^{(2)}$ cavities. In particular, synchronously pumped optical parametric oscillators (SPOPOs) have been were predicted to show multi-modal squeezing in Refs [166, 167]. Such a system consists of a cavity which includes a $\chi^{(2)}$ nonlinear crystal that is pumped by a train of pulses that are temporally separated by the cavity round-trip time [168, 169]. The pump intensity is set such that spontaneous optical parametric down-conversion leads to the generation of quantum correlations in the OPO frequency modes. This was first experimentally confirmed in Ref [170] with the observation of intensity (photon number) squeezing for a set of at least two frequency modes. Ref [171] developed on this work, using an OPO to generate a 60 modal multi-partite entangled state, the largest such state that had been generated at the time of publication in 2014. Such systems have been shown to be a sufficient resource state for universal quantum computation, making them an interesting area of research [172, 173].

These demonstrations were done in large, free-space cavities whose small FSR make addressing different frequency modes individually difficult. Ref [174] solves this problem, utilising crystalline WGM resonators. Such systems are also easier to fabricate repeatedly, and their small footprint and ability to be integrated on-chip make them a promising candidate for future quantum optic technologies.

Still, the frequency doubling/halving nature of the $\chi^{(2)}$ nonlinearity means that it couples light of vastly different wavelength. The $\chi^{(3)}$ nonlinearity allows for all modes to be of similar wavelength, for example in the telecoms band - a useful property for generating states that could be integrated into existing telecoms systems (e.g. for distributed quantum computing). Thus, is it possible to use the multi-modal nature of Kerr frequency combs, along with their ability to be integrated with existing telecoms systems, to produce multi-mode squeezed states? This chapter aims to answer this question[1].

This chapter will develop the system of equations that describes Kerr comb formation - the LLE - into a quantum model which can then be linearised to see how quantum fluctuations in each mode are entangled. Such a model was developed in Ref [53], though in this work mutual entanglement between modes was not investigated, rather the degree of quadrature squeezing between such modes was explored. A useful metric for understanding the degree of entanglement in a bipartite system is the *logarithmic negativity* [176–178], which is particularly interesting as it gives an entanglement monotone - i.e. higher levels of entanglement manifest as larger values of the logarithmic negativity. This metric has been applied to the case of modal pairs of the Kerr frequency combs in the sub-threshold, multi- and single-soliton regime in Ref [179], and has been used with experimental data from a single-soliton state in Ref [180]. This chapter expands this work to include higher-order dispersive effects, and includes the experimentally accessible regimes in which there is sub-unity conversion efficiency.

[1]In this context, multi-mode squeezed states refers to a system which consists of multiple subsystems, multiple pairs of which simultaneously show bi-partite entanglement. Such a system could share quantum information - via mutual entanglement - between each mode in a large scale network for quantum communications [175].

5.2 Theory

This derivation follows closely the notation and method shown in Ref [53] to find the coupled modal dynamics that are then treated using the method developed in Refs [176–178] to find the degree of entanglement between modes.

5.2.1 Modal expansion of the LLE

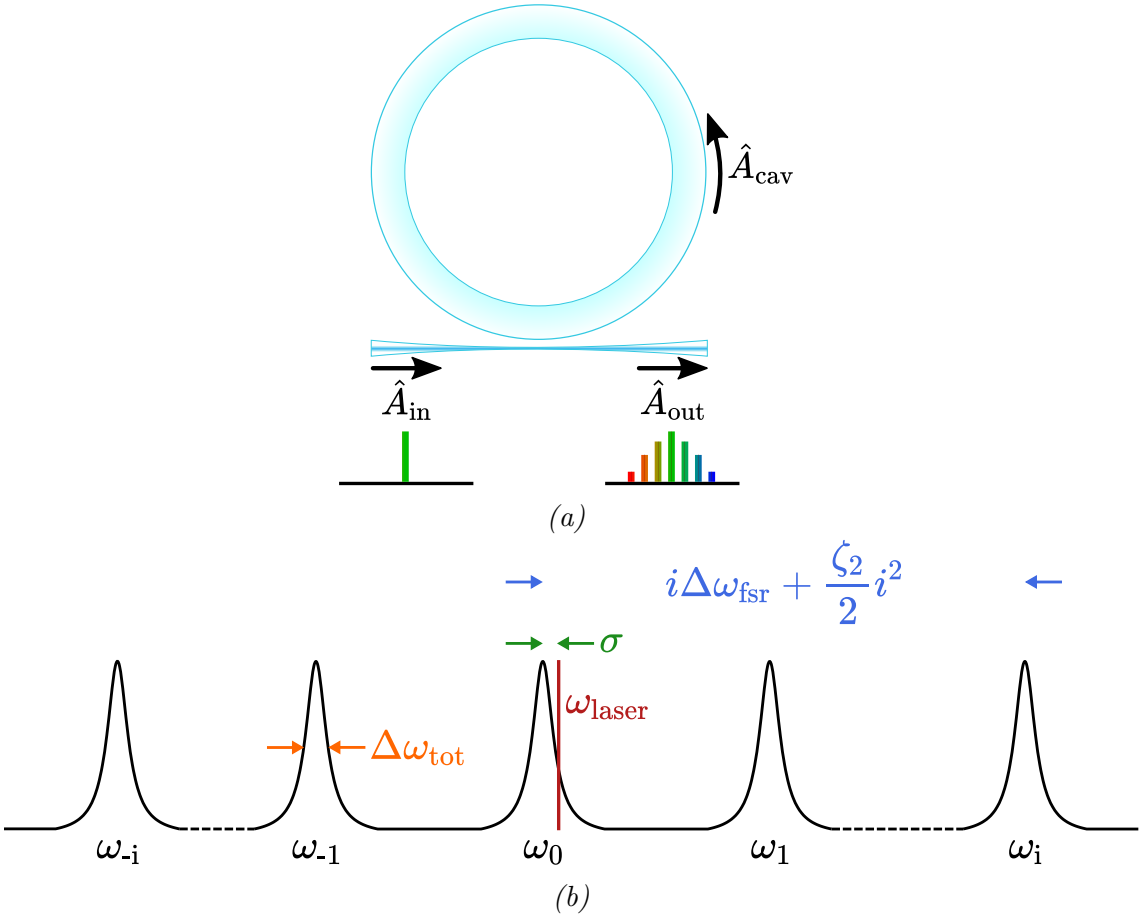

Figure 5.1: Four-wave mixing in a WGM resonator. a) A monochromatic input field couples into a resonator in which its intensity builds up above the FWM threshold. Accordingly, the output light is made up of multiple frequency modes. b) The input field frequency (ω_{laser}) is detuned from the pumped mode frequency (ω_0, linewidth $\Delta\omega_{tot}$) by an amount σ. This leads to light being generated in modes separated by an integer number of FSR away from the pump, with an efficiency determined by the FWM coupling strength, detuning and dispersion.

The Lugiato-Lefever Equation - Eq. (2.35) - describes the evolution of an electric field inside of a ring resonator that exhibits a Kerr nonlinearity as shown in Fig. 5.1a). A monochromatic input field couples into the resonator where its intensity builds up to above the stimulated four-wave mixing threshold. Although four-wave mixing has extremely high bandwidths in dielectrics [181], the resonator modes act to select the possible frequencies that can be efficiently generated by this process giving an output field consisting of discrete frequency modes corresponding to those separated by an

integer number of free-spectral ranges from the pump. This situation is shown in Fig. 5.1b): a continuous-wave (cw) laser couples into a cavity mode with a detuning of $\sigma = \omega_{\text{laser}} - \omega_0$. There exist cavity modes of the same transverse structure as the pumped mode, differing in longitudinal mode number l (with l taken to be zero for the pump). The resonance frequency of these modes can then be found as a Taylor series:

$$\omega_l = \omega_0 + \sum_{n=1}^{n_{\max}} \frac{\zeta_n}{n!} l^n, \tag{5.1}$$

which is typically truncated at $n_{\max} = 2$ [182]. The first term in the expansion, ζ_1, is simply the free-spectral range of the cavity: $\Delta\omega_{\text{fsr}}$. The second term, ζ_2, is the group-velocity dispersion (termed normal when $\zeta_2 < 0$, anomalous when $\zeta_2 > 0$). It has been shown [53, 60] that the electric field envelope $\mathcal{A}$ governed by the following equation:

$$\frac{\partial \mathcal{A}}{\partial t} = \left(-\kappa_{\text{tot}} + i\sigma\right)\mathcal{A} + ig_0\left|\mathcal{A}\right|^2 + i\frac{\zeta_2}{2}\frac{\partial^2 \mathcal{A}}{\partial \theta^2} + \sqrt{2\kappa_{\text{t}}}\mathcal{A}_{\text{in}}, \tag{5.2}$$

and can be expanded in terms of its modes:

$$\frac{\partial \mathcal{A}_l}{\partial t} = \left(-\kappa_{\text{tot}} + i\left[\sigma - \frac{\zeta_2}{2}l^2\right]\right)\mathcal{A}_l + \delta\left(l\right)\sqrt{2\kappa_{\text{t}}}\mathcal{A}_{\text{in}} + ig_0\sum_{m,n,p}\delta\left(m - n + p - l\right)\mathcal{A}_m\mathcal{A}_n^\star\mathcal{A}_p, \tag{5.3}$$

which is equivalent to the spatiotemporal LLE given in Eq. (2.35). Note that the electric field envelope $\mathcal{A}$ has now been normalised such that $\left|\mathcal{A}\right|^2$ gives the number of photons occupying the cavity. The modal expansion gives an associated field envelope for each mode, $\mathcal{A}_j$, where $\left|\mathcal{A}_j\right|^2$ is the number of photons in mode j, and the Kerr-effect in this picture is a mixing of these fields. The solution of the LLE is detailed in Appendix A.

5.2.2 Quantisation of the LLE

Canonical quantisation of this system then gives a way to infer the quantum properties of the associated states:

- Replace field amplitudes (and their conjugates) with annihilation (creation) operators: $\mathcal{A}_j \rightarrow \hat{a}_j$ ($\mathcal{A}_j^\star \rightarrow \hat{a}_j^\dagger$), subject to the usual commutation relations ($\left[\hat{a}_i, \hat{a}_j^\dagger\right] = \delta_{i,j}$, $\left[\hat{a}_i, \hat{a}_j\right] = \left[\hat{a}_i^\dagger, \hat{a}_j^\dagger\right] = 0$) [183].

- Treat all coupling ports and noise sources as having a vacuum fluctution operator $\hat{V}_{s,j}$ where subscript s specifies the origin of the fluctuation, and j the frequency mode for which it acts [184]. These fluctuations are zero-mean, temporally uncorrelated and obey the commutation relations $\left[\hat{V}_{s,i}\left(t\right), \hat{V}_{s',j}^\dagger\left(t'\right)\right] = \delta_{s,s'}\delta_{i,j}\delta\left(t - t'\right)$, $\left[\hat{V}_{s,i}\left(t\right), \hat{V}_{s',j}\left(t'\right)\right] = \left[\hat{V}_{s,i}^\dagger\left(t\right), \hat{V}_{s',j}^\dagger\left(t'\right)\right] = 0$.

Under canonical quantisation Eq. (5.3) becomes:

$$\dot{\hat{a}}_l = \left(-\kappa_{\text{tot}} + i\left[\sigma - \frac{\zeta_2}{2}l^2\right]\right)\hat{a}_l + \delta(l)\sqrt{2\kappa_{\text{t}}}\mathcal{A}_{\text{in}}\hat{\mathbb{1}} + \sqrt{2\kappa_{\text{t}}}\hat{V}_{\text{t},j} + \sqrt{2\kappa_{\text{i}}}\hat{V}_{\text{i},j} + ig_0\sum_{m,n,p}\delta(m-n+p-l)\,\hat{a}_n^\dagger\hat{a}_m\hat{a}_p, \tag{5.4}$$

where we can see that there are two sources of loss: subscript i denotes intrinsic losses, with t indicating resonator-waveguide coupling losses. These each have an associated loss rate κ_s which leads to the total loss rate $\kappa_{\text{tot}} = \kappa_{\text{i}} + \kappa_{\text{t}}$ which is half the value of the full-width at half-maximum (FWHM) linewidth shown in Fig. 5.1b). All loss rates are taken to be the same for each mode. It is worth noting that Eq. (5.4) has the form of a Langevin equation which is often seen in cavity quantum optics [185].

Remark: Eq. (5.4) gives an intuitive way to think about the nature of the Kerr nonlinearity. The associated Hamiltonian is $\hat{H}_{\text{Kerr}} = -\frac{1}{2}g_0\sum_{m,n,p,q}\delta(m-n+p-q)\,\hat{a}_m^\dagger\hat{a}_n^\dagger\hat{a}_p\hat{a}_q$ which shows that the Kerr effect is simply the simultaneous annihilation, and creation, of two pairs of photons in different modes subject to energy conservation (from the δ function constraint). In general this leads to the coherent generation of photon pairs in different frequency modes, leading to complex quantum correlations.

Specifically, when the field indices are such that only one or two-modes are involved, we get the Hamiltonians for *self*- and *cross*-phase modulation (SPM, XPM) respectively: $\hat{H}_{\text{SPM}} = -\frac{1}{2}g_0\sum_m \hat{a}_m^\dagger\hat{a}_m^\dagger\hat{a}_m\hat{a}_m$, $\hat{H}_{\text{XPM}} = -g_0\sum_{m,n}\hat{a}_m^\dagger\hat{a}_n^\dagger\hat{a}_n\hat{a}_m$ (where $m \neq n$). These lead to the simultaneous annihilation and creation of photons in the same mode with a phase delay set by the nonlinear coupling strength and the intensity of the same (for SPM) or counterpart (for XPM) mode: an intensity-dependent refractive index arises. The SPM Hamiltonian has two such annihilation/creation events for mode m, whereas for XPM there is only one such event but *four* possible index combinations that can lead to it. Accordingly the magnitude of XPM is twice that of SPM (all intensities being equal) - this is another explanation of the physical principle that was required for the phenomena explained in Chapters 3 and 4.

5.2.3 Linearisation of the quantum model

Equation (5.4) is a multipartite nonlinear equation and thus computationally difficult to solve, but the system can be linearised by assuming that the modes compose of a classical field perturbed by a small quantum fluctuation: $\hat{a}_l = \mathcal{A}_l + \delta\hat{a}_l$. Inserting this into Eq. (5.4) and ignoring terms in $\delta\hat{a}_l$ which are higher than first order gives two equations: Eq. (5.3b) for the classical fields and the following linear equation for the quantum fluctuations:

$$\delta\dot{\hat{a}}_l = -\left(\kappa_{\text{tot}} - i\left(\sigma - \frac{1}{2}\zeta_2 l^2\right)\right)\delta\hat{a}_l + \sum_s\sqrt{2\kappa_s}\hat{V}_{s,l} + ig_0\sum_{m,n,p}\delta(m-n+p-l)\left(A_mA_p\delta\hat{a}_n^\dagger + A_n^\star A_p\delta\hat{a}_m + A_n^\star A_m\delta\hat{a}_p\right), \tag{5.5}$$

This linearisation step was first developed in Ref [163] as a method to tame the nonlinear dynamics of the system. In general, the Kerr-effect leads to non-Gaussian states which can be difficult to analyse though this linearisation step (i.e. ignoring higher order terms in $\delta\hat{a}_l$) approximates all states as Gaussian. This linearisation step is invalid when the system is proximal to critical points (in this case, when a

modal pair is near their lasing threshold) and in the absence of thermal fluctuations [162, 163]. Accordingly, in order to satisfy the Gaussian approximation, all input states will be Gaussian (coherent for the pump, vacuum for all other modes) and the classical dynamics will be confirmed to be stable and not close to any critical points.

We will now limit the modes under consideration to those that are maximally distant in mode number from the pump by some integer K, such that $l, m, n, p \in \{-K, -K+1, \dots K\}$. The specific value of K is chosen such that the photon occupancy of the highest order mode is negligible, i.e. $|\mathcal{A}_K|^2 \ll 1$. We can now rewrite Eq. (5.5) as (N.B. some slight index changing for convenience):

$$\delta\dot{\hat{a}}_j = \sum_{i=-K}^{K} R_{j,i}\delta\hat{a}_i + S_{j,i}\delta\hat{a}_i^\dagger + \sum_s \sqrt{2\kappa_s}\hat{V}_{s,j}, \tag{5.6}$$

where $R_{j,i}$ is given by:

$$R_{j,i} = -\left(\kappa_{\text{tot}} - i\left(\sigma - \frac{1}{2}\zeta_2 j^2\right)\right)\delta\left(j-i\right) + 2ig_0\sum_{m,n}\delta\left(m-n+i-j\right)A_m A_n^\star, \tag{5.7}$$

and $S_{j,i}$ is given by:

$$S_{j,i} = ig_0\sum_{m,n}\delta\left(m+n-i-j\right)A_m A_n. \tag{5.8}$$

This can be written succinctly as a matrix equation:

$$\delta\dot{\hat{\boldsymbol{a}}} = \boldsymbol{R}\delta\hat{\boldsymbol{a}} + \boldsymbol{S}\delta\hat{\boldsymbol{a}}^\dagger + \sum_s \sqrt{2\kappa_s}\hat{\boldsymbol{V}}_s, \tag{5.9}$$

with $\delta\hat{\boldsymbol{a}} = [\delta\hat{a}_{\text{K}} \dots \delta\hat{a}_{\text{-K}}]^T$, $\hat{\boldsymbol{V}}_s = \left[\hat{V}_{s,\text{K}} \dots \hat{V}_{s,\text{-K}}\right]^T$, and matrices $\boldsymbol{R}$, $\boldsymbol{S}$ having elements defined in Eqs. (5.6b,c). Together with the Hermitian conjugate of this equation, we can contain all of the quantum dynamics of the system in a single equation:

$$\begin{bmatrix}\delta\dot{\hat{\boldsymbol{a}}}\\ \delta\dot{\hat{\boldsymbol{a}}}^\dagger\end{bmatrix} = \begin{bmatrix}\boldsymbol{R}, & \boldsymbol{S}\\ \boldsymbol{S}^\star, & \boldsymbol{R}^\star\end{bmatrix}\begin{bmatrix}\delta\hat{\boldsymbol{a}}\\ \delta\hat{\boldsymbol{a}}^\dagger\end{bmatrix} + \sum_s \sqrt{2\kappa_s}\begin{bmatrix}\hat{\boldsymbol{V}}_s\\ \hat{\boldsymbol{V}}_s^\dagger\end{bmatrix}, \tag{5.10}$$

transforming this equation into the quadrature basis simplifies the dynamics by having purely real matrices. These quadrature operators are vectorised $\delta\hat{\boldsymbol{X}} = \left[\delta\hat{X}_{\text{K}} \dots \delta\hat{X}_{\text{-K}}\right]^T$, $\delta\hat{\boldsymbol{Y}} = \left[\delta\hat{Y}_{\text{K}} \dots \delta\hat{Y}_{\text{-K}}\right]^T$, where each modal quadrature follows the usual definition $\delta\hat{X}_j = \frac{1}{\sqrt{2}}\left(\delta\hat{a}_j + \delta\hat{a}_j^\dagger\right)$, $\delta\hat{Y}_j = \frac{i}{\sqrt{2}}\left(-\delta\hat{a}_j + \delta\hat{a}_j^\dagger\right)$ such that:

$$
\begin{aligned}
\begin{bmatrix}\delta\hat{\boldsymbol{X}}\\ \delta\hat{\boldsymbol{Y}}\end{bmatrix} &= \frac{1}{\sqrt{2}}\begin{bmatrix}\mathbb{1}, & \mathbb{1}\\ -i\mathbb{1}, & i\mathbb{1}\end{bmatrix}\begin{bmatrix}\delta\hat{\boldsymbol{a}}\\ \delta\hat{\boldsymbol{a}}^{\dagger}\end{bmatrix},\\
\begin{bmatrix}\delta\dot{\hat{\boldsymbol{X}}}\\ \delta\dot{\hat{\boldsymbol{Y}}}\end{bmatrix} &= \frac{1}{\sqrt{2}}\begin{bmatrix}\mathbb{1}, & \mathbb{1}\\ -i\mathbb{1}, & i\mathbb{1}\end{bmatrix}\begin{bmatrix}\boldsymbol{R}, & \boldsymbol{S}\\ \boldsymbol{S}^{\star}, & \boldsymbol{R}^{\star}\end{bmatrix}\begin{bmatrix}\delta\hat{\boldsymbol{a}}\\ \delta\hat{\boldsymbol{a}}^{\dagger}\end{bmatrix} + \sum_{s}\sqrt{\kappa_s}\begin{bmatrix}\mathbb{1}, & \mathbb{1}\\ -i\mathbb{1}, & i\mathbb{1}\end{bmatrix}\begin{bmatrix}\hat{\boldsymbol{V}}_s\\ \hat{\boldsymbol{V}}_s^{\dagger}\end{bmatrix},\\
&= \frac{1}{2}\begin{bmatrix}\mathbb{1}, & \mathbb{1}\\ -i\mathbb{1}, & i\mathbb{1}\end{bmatrix}\begin{bmatrix}\boldsymbol{R}, & \boldsymbol{S}\\ \boldsymbol{S}^{\star}, & \boldsymbol{R}^{\star}\end{bmatrix}\begin{bmatrix}\mathbb{1}, & i\mathbb{1}\\ \mathbb{1}, & -i\mathbb{1}\end{bmatrix}\begin{bmatrix}\delta\hat{\boldsymbol{X}}\\ \delta\hat{\boldsymbol{Y}}\end{bmatrix} + \sum_{s}\sqrt{\kappa_s}\begin{bmatrix}\mathbb{1}, & \mathbb{1}\\ -i\mathbb{1}, & i\mathbb{1}\end{bmatrix}\begin{bmatrix}\hat{\boldsymbol{V}}_s\\ \hat{\boldsymbol{V}}_s^{\dagger}\end{bmatrix},\\
\begin{bmatrix}\delta\dot{\hat{\boldsymbol{X}}}\\ \delta\dot{\hat{\boldsymbol{Y}}}\end{bmatrix} &= \begin{bmatrix}\Re(\boldsymbol{R})+\Re(\boldsymbol{S}), & -\Im(\boldsymbol{R})+\Im(\boldsymbol{S})\\ \Im(\boldsymbol{R})+\Im(\boldsymbol{S}), & \Re(\boldsymbol{R})-\Re(\boldsymbol{S})\end{bmatrix}\begin{bmatrix}\delta\hat{\boldsymbol{X}}\\ \delta\hat{\boldsymbol{Y}}\end{bmatrix} + \sum_{s}\sqrt{\kappa_s}\begin{bmatrix}\hat{\boldsymbol{V}}_s+\hat{\boldsymbol{V}}_s^{\dagger}\\ i\left(-\hat{\boldsymbol{V}}_s+\hat{\boldsymbol{V}}_s^{\dagger}\right)\end{bmatrix},
\end{aligned}
\tag{5.11}
$$

with $\mathbb{1}$ as the $(2K+1)$ dimensional identity operator. This is a quantum Langevin equation of the form:

$$\dot{\overrightarrow{u}} = \boldsymbol{A}\overrightarrow{u} + \overrightarrow{n}(t). \tag{5.12}$$

5.2.4 Finding the steady state correlation matrix

Equation (5.12) has a solution at time t:

$$\overrightarrow{u}(t) = \boldsymbol{M}(t)\overrightarrow{u}(0) + \int_{s=0}^{t} ds\boldsymbol{M}(s)\overrightarrow{n}(t-s), \tag{5.13}$$

where $\boldsymbol{M}(t) = \exp \boldsymbol{A}t$. This system is assumed to be stable (i.e. $\boldsymbol{A}$ has eigenvalues with negative real parts such that $\boldsymbol{M}(\infty) = 0$) as a consequence of the stability of the numerically solved LLE. The elements of the steady-state correlation matrix, $\boldsymbol{V}$, are given by:

$$V_{i,j} = \frac{\langle u_i(\infty)u_j(\infty) + u_j(\infty)u_i(\infty)\rangle}{2}. \tag{5.14}$$

The uncorrelated nature of the noise, alongside system stability, sets the steady-state as:

$$u_i(\infty) = \sum_k \int_{s=0}^{\infty} dsM_{i,k}(s)n_k(t-s), \tag{5.15}$$

so the correlation matrix elements are:

$$V_{i,j} = \sum_{k,l}\int_{s=0}^{\infty}\int_{s'=0}^{\infty} dsds'M_{i,k}(s)M_{j,l}(s')\Phi_{k,l}(s-s'), \tag{5.16}$$

where the noise correlation function is:

$$
\begin{aligned}
\Phi_{k,l}(s-s') &= \frac{\langle n_k(s)n_l(s') + n_l(s)n_k(s')\rangle}{2},\\
&= \delta(s-s')\delta(k-l)\sum_s \kappa_s,\\
&= \delta(s-s')\delta(k-l)\kappa_{\text{tot}},\\
&= \delta(s-s')D_{k,l},
\end{aligned}
\tag{5.17}
$$

due to the delta correlations of the noise in time and modes. Accordingly Eq. (5.16) becomes:

$$\boldsymbol{V} = \int_{s=0}^{\infty} ds \boldsymbol{M}(s) \boldsymbol{D} \boldsymbol{M}^{T}(s), \tag{5.18}$$

with

$$\boldsymbol{D} = \kappa_{\text{tot}} \mathbb{1}, \tag{5.19}$$

Equation (5.18) is the continuous-time case of the Lyapunov equation which is equivalent to (due to the system stability):

$$\boldsymbol{A}\boldsymbol{V} + \boldsymbol{V}\boldsymbol{A}^{T} = -\boldsymbol{D}, \tag{5.20}$$

which is a linear equation with an efficient solution for the correlation matrix $\boldsymbol{V}$ [186].

5.2.5 Logarithmic negativity

Following from the work of Lee et al. in 2000 [187] in 2002, Vidal and Werner presented a computable measure of entanglement called negativity $\mathcal{N}$ [178]. This parameter, along with the similarly defined *logarithmic* negativity $E_{\mathcal{N}}$, find useful application because they are entanglement monotones (and thus give a useful metric for the degree of entanglement in a composite system) and can be used with mixed states. They are defined as follows:

$$\mathcal{N}(\rho) = \frac{\left\|\rho^{T_A}\right\|_1 - 1}{2}, \tag{5.21a}$$

$$E_{\mathcal{N}}(\rho) = \log_2 \left\|\rho^{T_A}\right\|_1, \tag{5.21b}$$

where ρ is a bipartite density matrix of systems A and B, ρ^{T_A} is the partial transpose of this state over system A, and $\|\rho\|_1 = \text{Tr}\sqrt{\rho\rho^{\dagger}}$ is the trace norm of a system. N.B. The system over which the partial transpose is completed does not affect these parameters as $\rho^{T_B} = \left(\rho^{T_A}\right)^T$ and the trace norm is invariant under transpose.

Gaussian states

The effect of Eq. (5.10) is to give a multi-mode squeezed vacuum, an example of a Gaussian state. Accordingly, the specific method to compute the logarithmic negativity associated with Gaussian states is required and was developed by Kim et al. in 2002 [188].

Bipartite Gaussian states can be fully characterised by their first two moments. Only the second moments contain the information of the entanglement in the system, as the first can be reduced to zero using local displacements. Under these transformations, the resulting second moment $\boldsymbol{v}$ is simply the system covariance matrix [178] which can be given in general as:

$$\boldsymbol{v} = \begin{bmatrix} \boldsymbol{\mathcal{A}}, & \boldsymbol{\mathcal{C}} \\ \boldsymbol{\mathcal{C}}^{T}, & \boldsymbol{\mathcal{B}}, \end{bmatrix} \tag{5.22}$$

where $\boldsymbol{\mathcal{A}}$ and $\boldsymbol{\mathcal{B}}$ describe the variance of the systems A and B respectively, and $\boldsymbol{C}$ captures their covariance.

Calculating the trace norm of a system ρ with such a correlation matrix is easier after symplectic diagonalisation, a linear transformation that describes the system in terms of two single-mode thermal-like oscillators. The logarithmic negativity is then a function of one of the eigenvalues of this symplectic spectrum and is given in terms of the sub-matrices of Eq. (5.22) as [178, 189]:

$$E_{\mathcal{N}}(\rho) = \max\left[0, -\ln 2\eta\right], \tag{5.23}$$

where the parameter η is given by:

$$\eta = 2^{-\frac{1}{2}}\left[\Sigma(\boldsymbol{v}) - \left[\Sigma(\boldsymbol{v})^2 - 4\det\boldsymbol{v}\right]^{\frac{1}{2}}\right]^{\frac{1}{2}}, \tag{5.24}$$

and the function Σ is given by:

$$\Sigma(\boldsymbol{v}) = \det\boldsymbol{\mathcal{A}} + \det\boldsymbol{\mathcal{B}} - 2\det\boldsymbol{\mathcal{C}}. \tag{5.25}$$

5.2.6 Bipartite entanglement matrix

The previous section describes how to compute the logarithmic negativity of a *bipartite* Gaussian state. However, Kerr-frequency combs consist of many modes – how shall entanglement be calculated for such a system?

It is possible to develop a multipartite version of Eq. (5.23), but a more interesting metric is that of bipartite entanglement between each mode pair; one can imagine creating a Kerr-comb and demultiplexing each frequency mode, giving each to a different party. Giving Alice mode i and Bob j of the total system, $\rho_{\mathbf{K}}$, their reduced system and associated covariance matrix is:

$$\rho_{\boldsymbol{K}} \to \rho_{i,j} = \mathrm{Tr}_{\{i,j\}^c}\,\rho_{\mathbf{K}}, \tag{5.26a}$$

$$\boldsymbol{V} \to \boldsymbol{v}^{i,j}, \tag{5.26b}$$

where the subscript on the trace means to trace over all subsystems except i and j, $\boldsymbol{v}^{i,j}$ is a sub-matrix of $\boldsymbol{V}$ corresponding to the modes i and j. Being of the same form as Eq. (5.22), the associated bipartite logarithmic negativity $E_{\mathcal{N}}^{i,j}$ can be calculated [178, 190]. These values can then be set as the elements of a $(2K+1)\times(2K+1)$ matrix $\boldsymbol{E}$ - the bipartite entanglement matrix.

Procedure for calculation

1. *Choose the resonator parameters.* Choose the coupling rates to the environment (intrinsic losses: κ_i, and output waveguide coupling: κ_t), the detuning (σ), second-order dispersion (ζ) and input field strength ($\mathcal{A}_{\mathrm{in}}$). Set the maximum number of modes to simulate, K, such that the extremal modes are found to have negligible field strengths, thus ensuring that the solution has not been artificially truncated. N.B. These resonator parameters can be converted to their dimensionless equivalents given in Eq. (2.36) with only minor adjustments to the rest of this procedure.

2. *Solve for the classical fields $\mathcal{A}_l$.* Using the procedure given in Appendix A, the classical equations of motion - the LLE - can be solved.

3. *Calculate $\boldsymbol{R}$ and $\boldsymbol{S}$.* The coupling matrices for the system of annihilation and creation operators can be calculated using Eq. (5.6b,c).

4. *Calculate $\boldsymbol{A}$.* Convert $\boldsymbol{R}$ and $\boldsymbol{S}$ into the real matrix $\boldsymbol{A}$ using Eq. (5.11). This is the coupling matrix between the (vectorised) quadrature operators.

5. *Calculate the system covariance matrix $\boldsymbol{V}$.* This is done via the solution of the Lyapunov equation in Eq. (5.20). An algorithmic solution given in [186] (which is implemented in Python in the linear algebra part of the package SciPy using `solve_discrete_lyapunov`).

6. *Calculate the bipartite entanglement matrix, $\boldsymbol{E}$.* For each pair of modes (i, j), find the 4×4 sub-matrix $\boldsymbol{v}^{i,j}$ - the bipartite covariance matrix for these modes. Solve for the logarithmic negativity between these modes using Eq. (5.23), which is then set as the corresponding element of $\boldsymbol{E}$.

5.3 Results

The following discusses the entanglement matrices associated with various regimes of the Kerr-frequency comb: sub-threshold, Turing rolls, soliton crystals, single soliton, and a single soliton with a dispersive wave. Each of these figures is made of three panels, with the upper two panels showing the magnitudes of the classical fields - found from solving the LLE. The uppermost panel shows the intensity in each of the resonator modes, with the second showing the spatial intensity distribution inside the resonator. Below these are graphical representations of the entanglement matrix, with the logarithmic negativity given by the colour of each element of the matrix.

5.3.1 Below threshold comb

Figures 5.2 and 5.3 show the solution for a sub-threshold Kerr comb. Being sub-threshold, both only have a single mode - the pumped mode - lasing, and so the intensity is uniformly distributed around the resonator. As the classical field is made up of a single mode[2] only the anti-diagonal elements of the entanglement matrix can be non-zero. This is due to the fact that only the $\pm l$ modes can be coupled to each other when there is a single non-zero element of the classical fields, namely A_0.

The degree of entanglement - the logarithmic negativity - between the modes is non-trivial and follows some distribution based on mode number. In both figures, starting from the central mode pair and moving outwards, the degree of entanglement increases to some maximum before then progressively reducing. In Fig. 5.2 this maximum is found very quickly at modes ± 3; whereas the increase is more gradual in Fig. 5.3, reaching its maximum for modes ± 19. The is difference between the two systems arises because of their differing dispersion, β. This changes the effective detuning for each of the mode pairs, with those with minimal effective detuning (and

[2]N.B. Fig. 5.2 shows some intensity on the other modes but this is just a numerical artefact from the noise added to the numerical LLE solver - see Appendix A

hence the strongest phase matching for the process) having the strongest levels of entanglement. Phase matching is a function of the pump detuning (α), dispersion (β), and the strength of the Kerr-effect which shifts signal/idler mode frequencies via cross-phase modulation. Their values were chosen somewhat arbitrarily to demonstrate how entanglement is dependent on them. Such sub-threshold dynamics are the most accessible experimentally and are discussed further in Chapter 6.

5.3.2 Turing rolls

Figure 5.4 shows the solution for a system that is above threshold in a state termed "Turing rolls". The upper panel shows that sidebands have been generated in the ± 19 modes, which have then cascaded to create sidebands in the ± 38 and ± 57 mode pairs. Interestingly, the primary modes that start lasing (± 19) are the same as those which have the strongest entanglement in Fig. 5.3; the difference between these plots is just the associated detunings with the phase matching for these modes now such that FWM is efficient enough to lead to lasing.

The lasing in these modes allows for further elements of the entanglement matrix to be non-zero, shown by the lines that are parallel to the main anti-diagonal. However this comes at the expense of the total magnitudes of logarithmic negativity, with these new coupling processes washing out some of the original entanglement. Qualitatively this makes sense: when there is multimodal coupling, the others must be traced over to determine the entanglement between a single pair. This acts to decohere the state, leaving it less entangled than if only the two-modes in question were coupled.

5.3.3 Soliton crystal

Soliton crystals are an example of an interesting state in nonlinear optics, in which multiple solitons are locked via their mutual interaction [191]. Such a state is shown in Fig. 5.5, in which each mode is lasing with a rather complex intensity distribution. This corresponds to multiple, here three, equidistant pulses in the intracavity intensity distribution.

The entanglement matrix associated with such a state is seen to be more complex, with each lasing mode giving rise to an anti-diagonal set of entangled pairs. Again this increased coupling has reduced the magnitude of entanglement between any single pair.

5.3.4 Single soliton

Figure 5.6 shows the results for a single soliton. The modal envelope of such a state follows a $\mathrm{sech}^2(l)$ profile (for mode number l), with the intensity of higher order modes diminishing. Temporally, this corresponds to a single pulse inside the resonator.

The associated entanglement matrix is interesting, showing regions in which all modal pairs are mutually entangled, but again with a correspondingly low magnitude of the effect.

5.3.5 Dispersive wave

All of the work here presented has been for resonators that demonstrate at most second order dispersion. However, the higher order terms of Eq. (5.1) can be taken into account and lead to solitons with a so-called dispersive wave [192]. Such a state is shown in Fig 5.7, and parameterised by β_3 in the LLE. The main difference between this and the single soliton state of Fig. 5.6 is the extra peak for the ≈ -25 mode. The higher order dispersion has made this mode well phase matched and so it has a higher associated intensity.

This has had some interesting effects on the entanglement matrix. Firstly, it has broken the symmetry such that there is a strong anti-diagonal line in the upper-right half of the figure. This has also led to fewer modes being entangled as they need to be well phase matched to two strong fields of rather different mode numbers, which leads to a greater maximum associated entanglement.

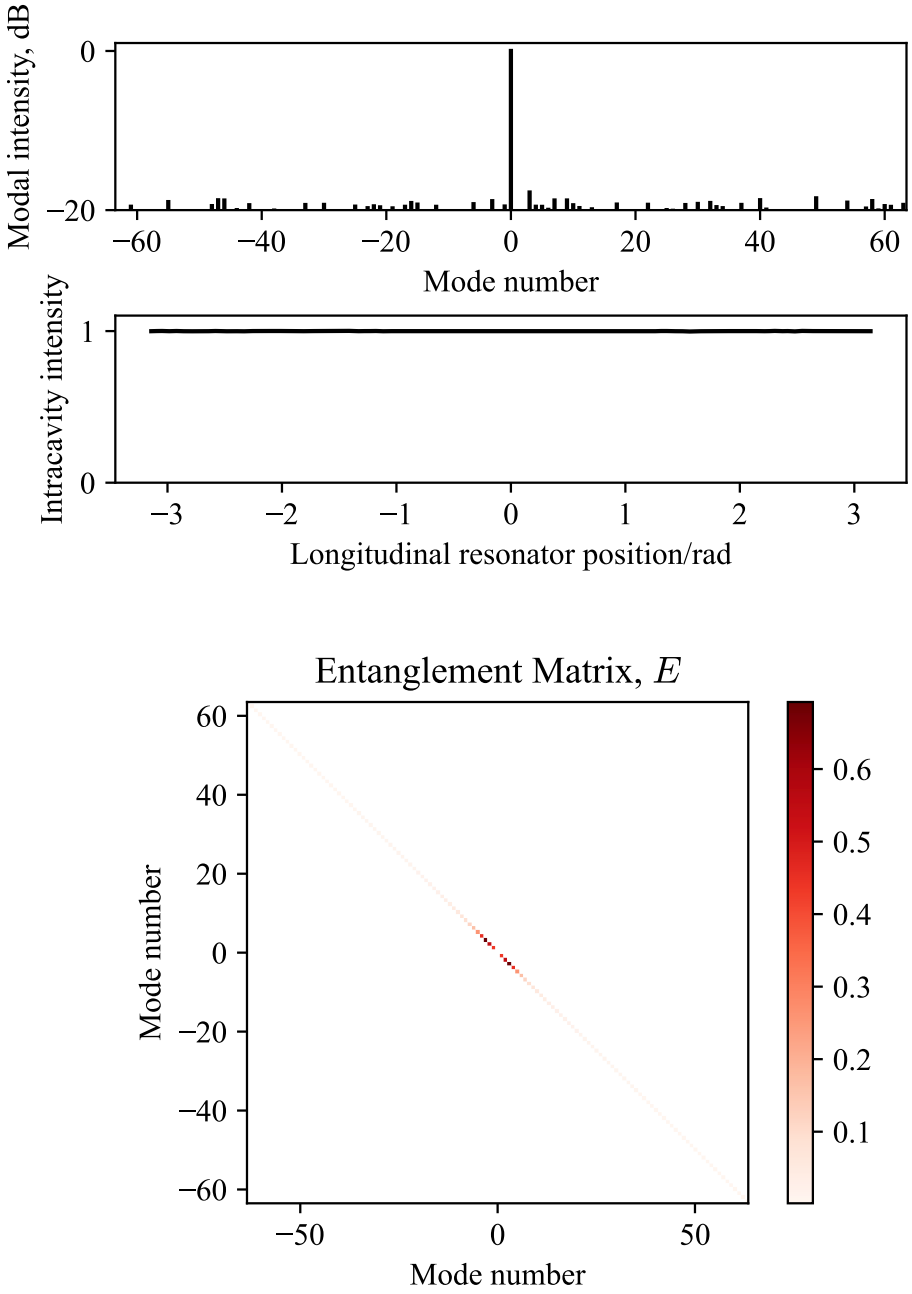

Figure 5.2: Classical and quantum properties of a sub-threshold Kerr frequency comb. The input parameters to the normalised LLE are $\alpha = 0.25$, $\beta = -0.4$ and $F = 1.25$. Only pairs of modes equidistant from the pump are entangled, with the combined effect of detuning, dispersion and nonlinearity making the innermost most entangled.

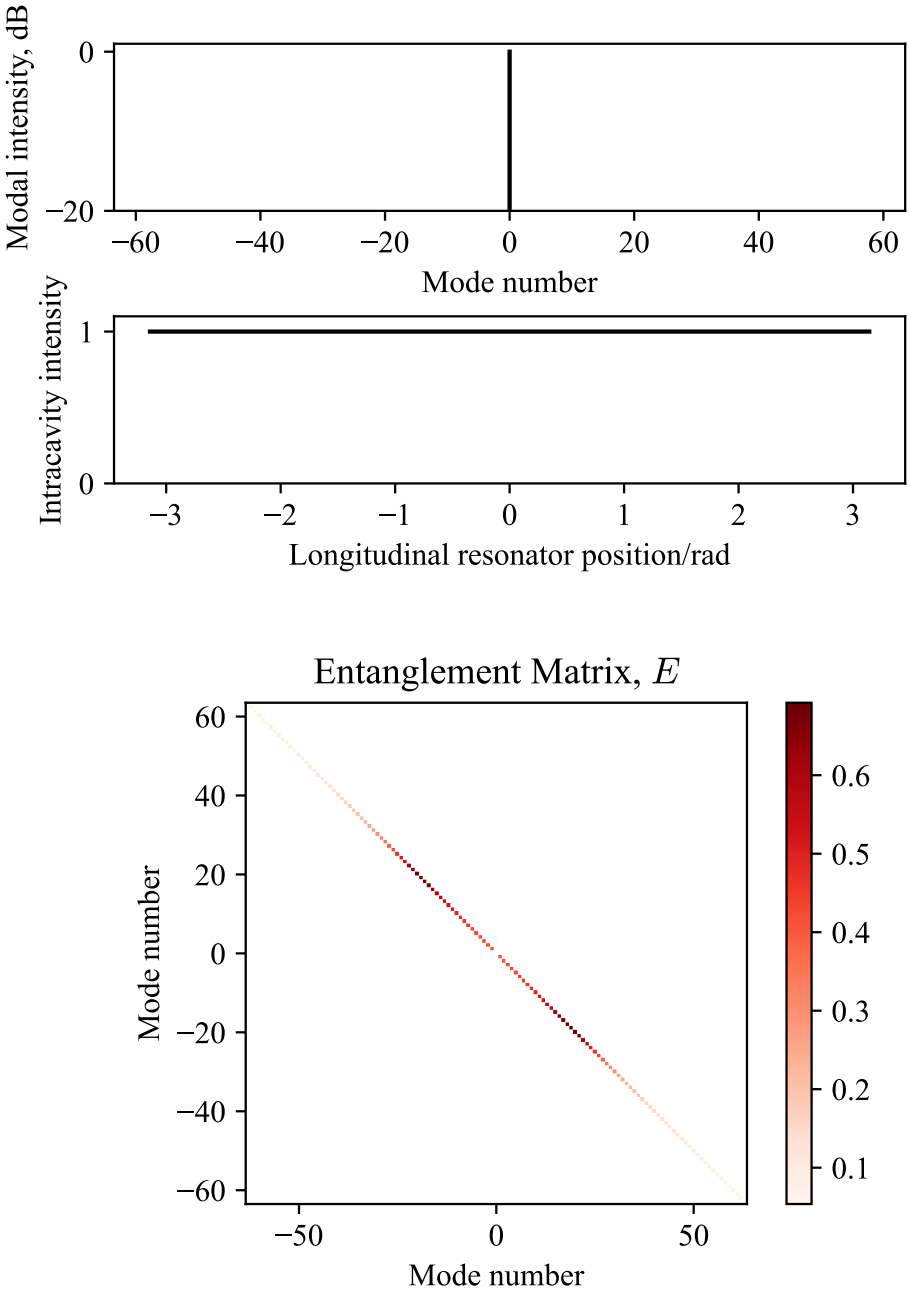

Figure 5.3: Classical and quantum properties of a sub-threshold Kerr frequency comb. The input parameters to the normalised LLE are $\alpha = 0.25$, $\beta = -0.01$ and $F = 1.25$. This system is still sub-threshold, ensuring only equidistant mode pairs are entangled, however cavity dispersion ensures that modes ± 19 share the highest degree of entanglement.

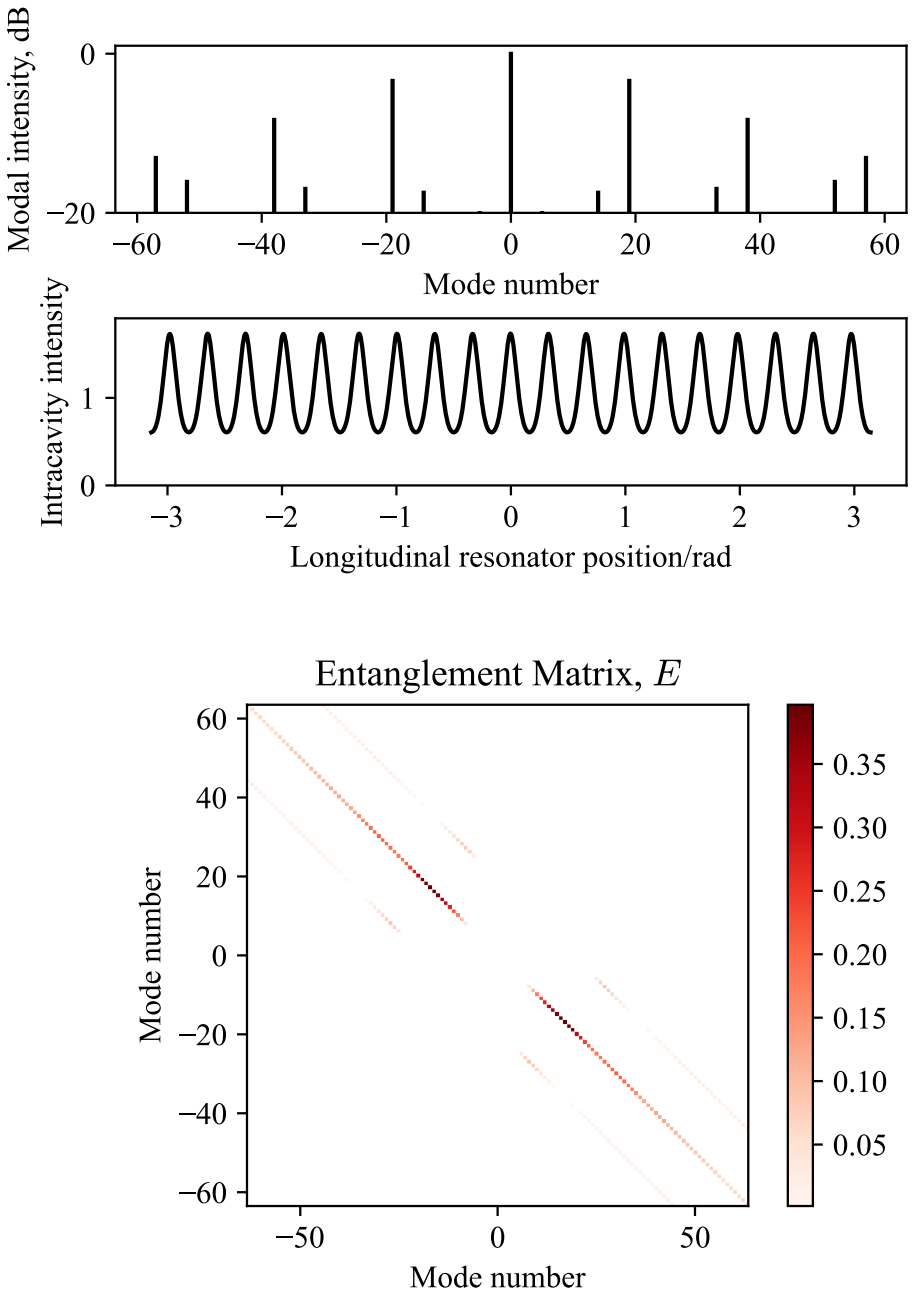

Figure 5.4: Classical and quantum properties of an above-threshold Kerr frequency comb. The input parameters to the normalised LLE are $\alpha = 0.45$, $\beta = -0.01$ and $F = 1.25$. The presence of sidebands in this system leads to further pairs of modes that are mutually entangled. However this comes at expense of the maximum amount of entanglement available between mode pairs.

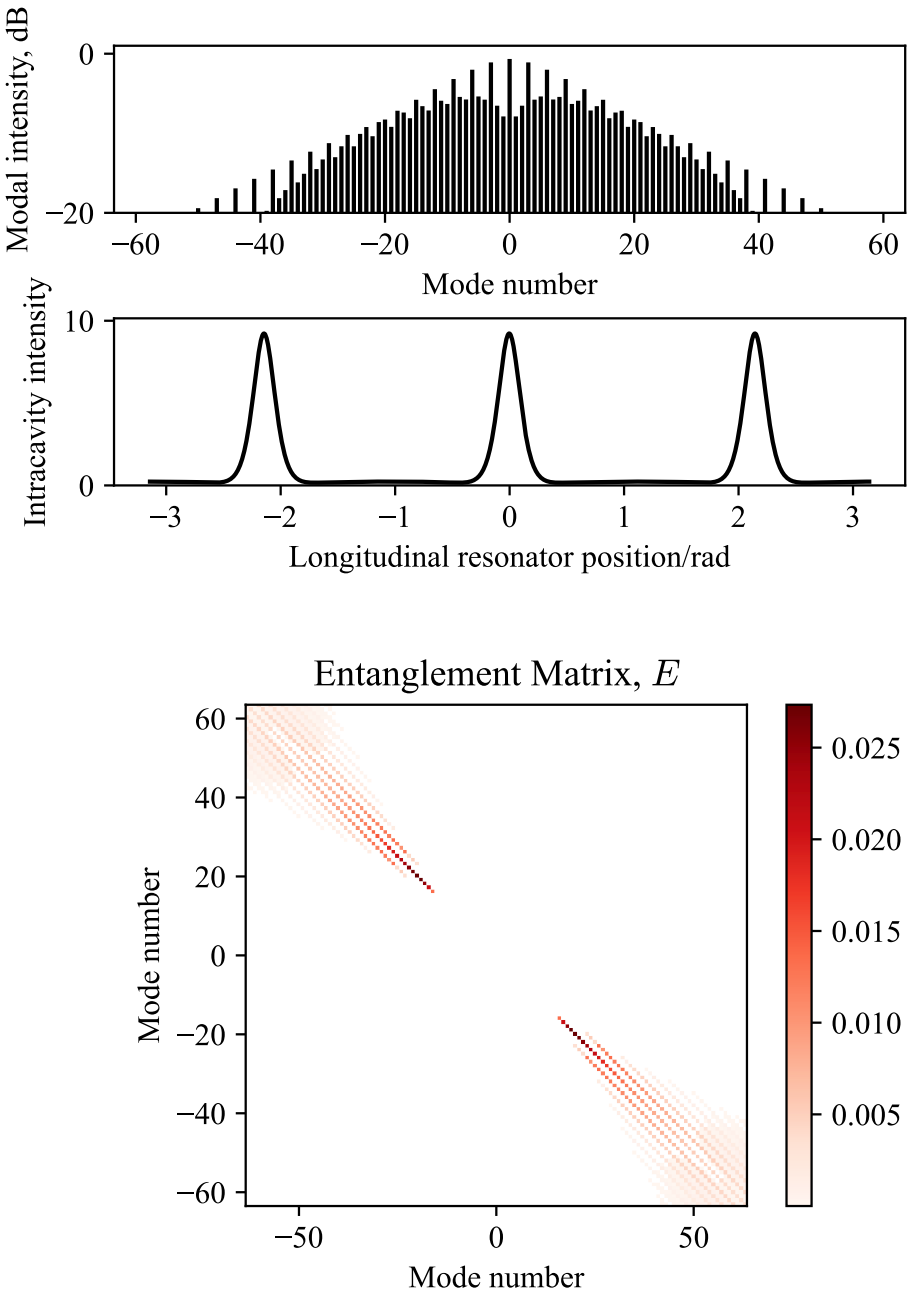

Figure 5.5: Classical and quantum properties of an soliton crystal state. The input parameters to the normalised LLE are $\alpha = 4.24$, $\beta = -0.15$ and $F = 2.01$. This system has many lasing sidebands with an interesting intensity profile due to their mutual locking. Again, this adds further mode pairs to the entanglement matrix whilst diminishing the degree of entanglement between any of them.

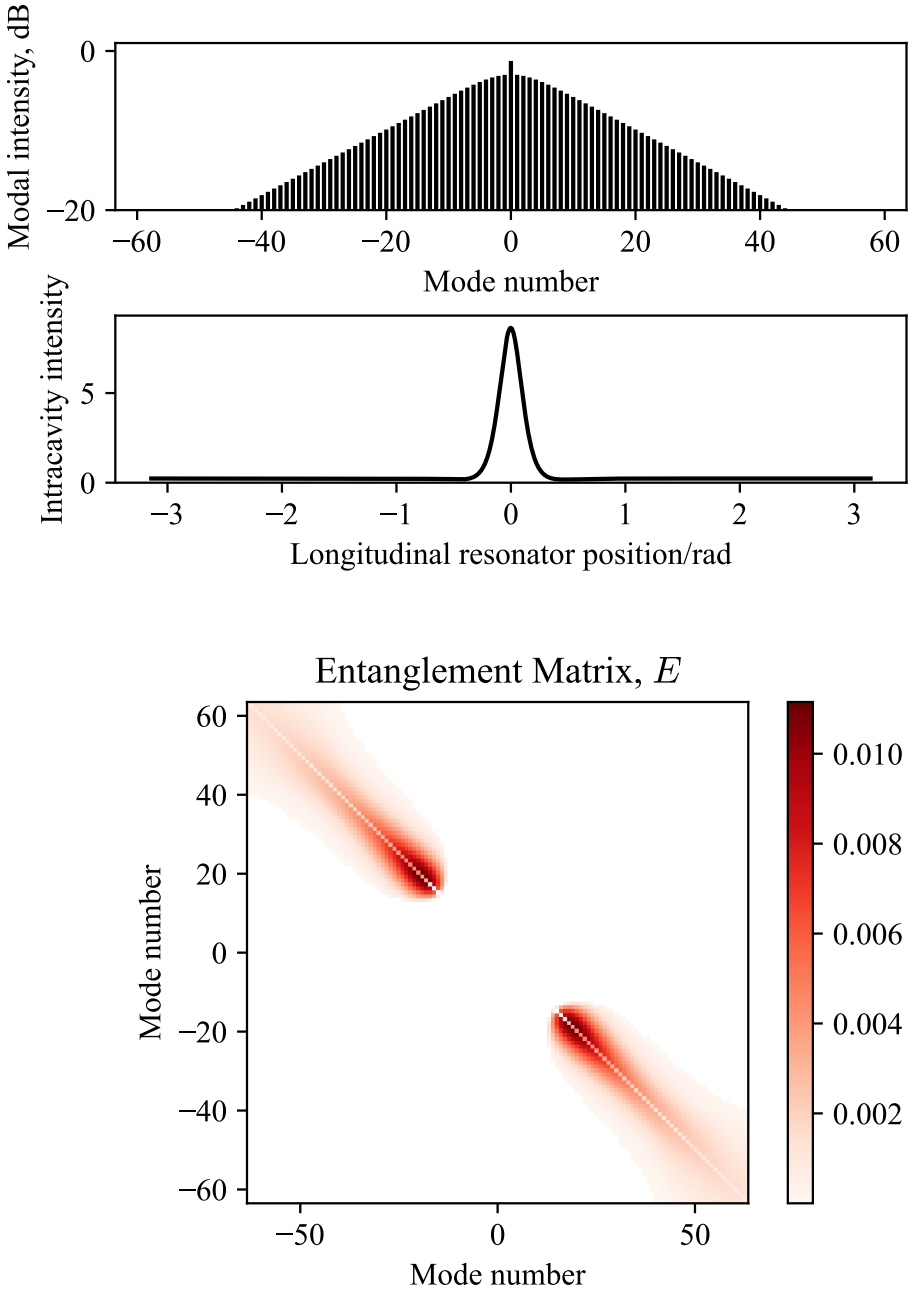

Figure 5.6: Classical and quantum properties of a single soliton state. The input parameters to the normalised LLE are $\alpha = 4.06$, $\beta = -0.15$ and $F = 1.91$. This system has many modes mutually entangled, though with a rather diminished magnitude in each.

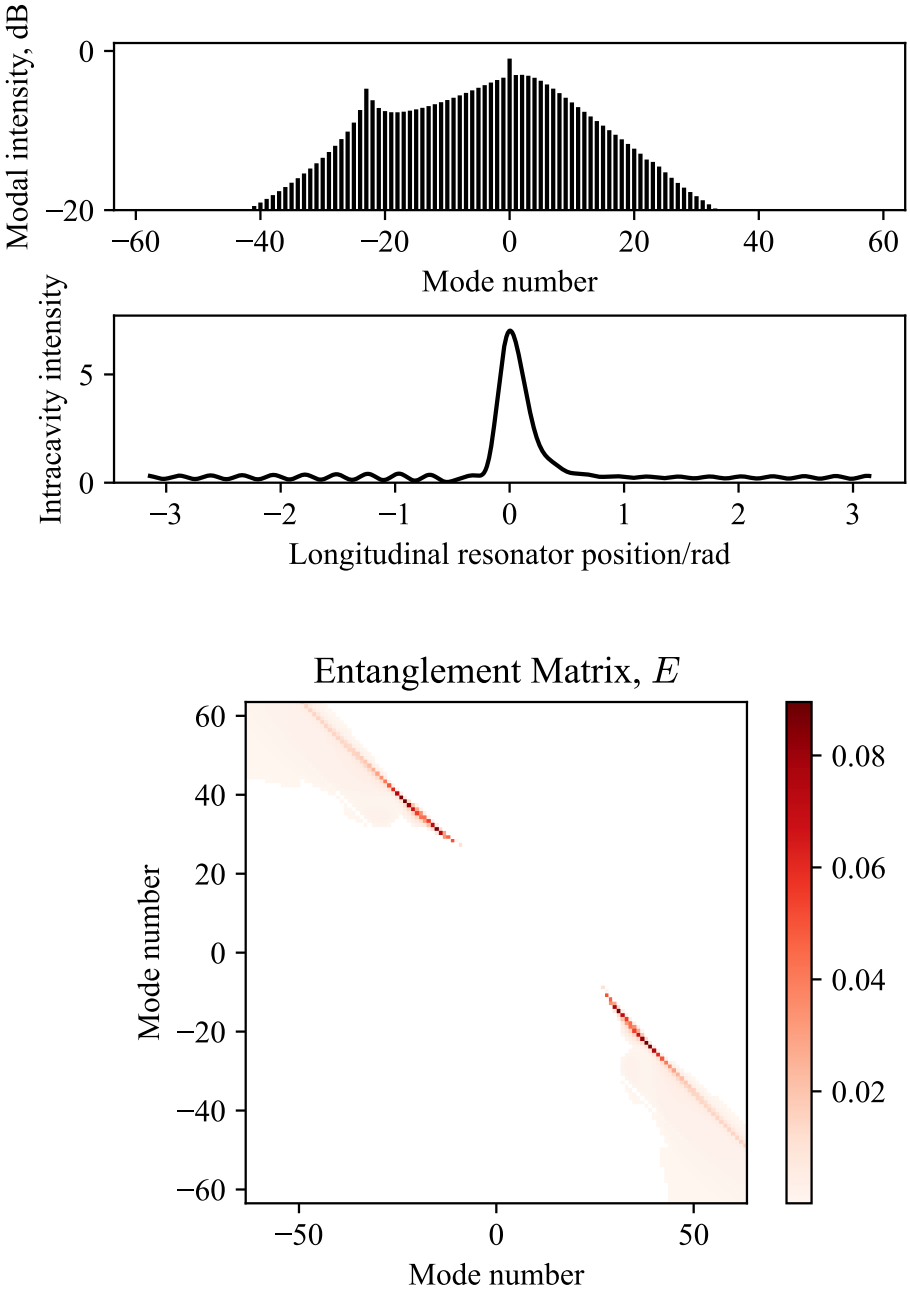

Figure 5.7: Classical and quantum properties of a single soliton state with a dispersive wave. The input parameters to the normalised LLE are $\alpha = 4.00$, $\beta = -0.15$, $\beta_3 = -0.025$, and $F = 1.91$. The strength of the sideband that causes the dispersive wave makes for quite the interesting asymmetric pattern.

5.3.6 Conclusion

This work shows that the Kerr frequency comb can indeed be used as a system to simultaneously entangle multiple mode pairs. When below threshold, only symmetric mode pairs (i.e. those of number $\pm l$ relative to the pump) are entangled, due to conservation of energy. Momentum must also be conserved, meaning that the degree of entanglement is also contingent on phase matching and thus on the interplay of pump detuning, nonlinearity and dispersion.

When above threshold, the presence of multiple strong classical fields leads to multiple avenues for FWM to couple modes. This leads to a more complex entanglement matrix, in which any single mode may be simultaneously entangled to multiple partners, though with reduced magnitude. This form of entanglement may find interesting applications in quantum networks.

A drawback of this approach is that all fields propagate in the same spatial mode at comparable wavelengths. This makes the subsequent demultiplexing of each mode to route, and address, each individually difficult. Utilising the larger FSRs of WGM resonators with smaller diameters increases the spectral separation of the modes, mitigating this issue, which can also be alleviated with improved filter design.

Another major drawback of this approach, in comparison to the optical states generated by synchronously driven optical parametric oscillators, is that in order to have a mode entangled to multiple partner modes, the system must operate above threshold. In this situation, the extra nonlinear coupling mechanisms act to wash-out quantum correlations between modal pairs, limiting the usefulness of such a, above-threshold, system.

This work shows the benefits of using a WGM resonator as a means of generating entangled optical states. The high Q-factors of such devices allow for the realisation of nonlinear phenomena at low powers, and they can be fabricated on-chip with materials that can easily be used with existing telecoms devices. The high intrinsic Q-factors of such devices mean that they can be operated in the over-coupled regime whilst maintaining significant intensity build-up. This allows the fragile quantum states to be out-coupled efficiently, whilst still only requiring low powers to produce. Such a scheme minimises losses to the environment, preserving the entanglement. Finally, the frequency selective nature of an optical cavity naturally splits the optical field into distinct modes. This ability to generate a plurality of entangled modes and transfer them to a telecoms system makes WGM resonators a promising route for the distribution of quantum information. Although this is of limited benefit as a source of multi-partite entanglement in the above threshold regime, it can be a useful source of bipartite entanglement in the telecom band when pumped below threshold, which will be explored further in Chapter 6.

5.3.7 Outlook

This chapter has shown that FWM in WGM resonators can create interesting entangled states of the resonant modes. Some further areas of research include:

- **Cavity input/output formalism.** All of the entanglement here discussed is for the cavity fields, however these are not accessible to the experimenter. Instead, some of this field will "leak" into an output waveguide to be explored, with the rest being lost to the environment. One would expect the output

field entanglement to approach that of the resonator fields in the limit that $\kappa_t \gg \kappa_i$ (κ_t: coupling loss rate, κ_i: intrinsic loss rate), and to approach zero in the opposite limit. However this has not been fully explored, and the intermediate behaviour would be of interest for experimental design as κ_i are set by the resonator, whereas κ_t can to some extent be controlled by the coupling between the resonator and waveguide. High κ_t will indeed ensure the output entanglement approaches that inside the resonator, but it also reduces the cavity intensity buildup due to the extra loss. It is thus expected that there will be some optimal ratio between the intrinsic and coupling loss rates that maximise the output field entanglement. A promising avenue for this work would be to follow the cavity input/output relations as discussed in Ref [193–195].

- **Comparison to other work.** This work follows a similar method to Ref [179], though with quite different qualitative results for the single soliton state. This is quite likely due to the pump suppression there demonstrated in which the intensity of the pump mode is lower than that of some sidebands. This seems to be an nonphysical situation which has been included to show an interesting entanglement matrix, but may be worth more investigation.

- **Multi-partite entanglement.** The analysis in this chapter has been limited to the bipartite entanglement, with all other modes traced over. Interesting future work could include looking at metrics for multi-modal entanglement, with no modes traced over, which may not show the same detrimental effects in the above-threshold regime. Indeed other forms of bipartite entanglement could be studied, say between the two systems made from taking all frequencies above the pump, and all those below.

- **Sub-threshold Kerr comb entanglement.** The sub-threshold Kerr comb, having only a single appreciable classical field (the pumped mode), is much simpler to analyse and seems to show promise for the levels of entanglement that it can exhibit. Chapter 6 includes a more detailed description of such a state and the experimental work that has been started to investigate it.

Chapter 6

Towards the generation of two-mode squeezed vacuum states

6.1 Introduction

The previous chapter showed how Kerr-frequency combs can contain interesting quantum correlations useful for quantum information applications, with FWM coupling different WGM resonator modes giving rise to complex networks of bipartite entanglement. Amongst the regimes identified, the sub-threshold regime is perhaps the most accessible for experiments that aim to study these quantum correlations.

It is not immediately obvious how sub-threshold dynamics can be of any interest as there is only one (classical) field. However, when the two-mode squeezing operator - a consequence of FWM - acts on a pair of modes in the vacuum state, it produces the *two mode squeezed vacuum* (TMSV) state. When looked at in the Fock (the photon number) basis, such states are understood to be a superposition of different photon numbers with photon number entanglement between the modes. Thus, if n photons is measured in one of the modes, this will project the other mode into the $|n\rangle$ photon state. Higher order, i.e. $n \geq 2$, states can be avoided by using low pump powers which reduces the likelihood of such events occurring. This is the basis of *heralded single photon sources*; a pair of pump photons annihilate to create a signal and idler pair, with the detection of one used to project the other mode into the single-photon state.

Single photon sources fall into two categories: the *heralded source*, as described above, and the spontaneous emission from *single quantum emitters* [196]. Single quantum emitters are atom-like systems that can only emit a single photon at a time - in contrast to heralded systems for which higher photon occupation is possible. Quantum dots are perhaps the most preeminent of such devices, but they have poor collection efficiencies (though impressive recent works are pushing the state-of-the-art [197]) and are difficult to reproducibly fabricate into photonic circuits [198]. Thus, there remains great interest in heralded sources of single photons.

This chapter describes unpublished work-in-progress which is intended to be developed into a journal article. Accordingly, rather than giving a comprehensive literature review, the aim is to highlight the key literature that contextualises the work here presented.

The major issue with this approach to generating single photons is that it is a probabilistic process, in any given time frame there is only a finite chance that a single photon will be heralded. Moreover, the method to increase the chance of such an event also increases the chances of higher photon numbers to be generated which would reduce how useful of a resource this state would be. One way to account for this issue is *multiplexing*, which is the process of attempting to make a number of photons in different modes such that at least one of these is near certain to succeed, heralding this success event and converting the associated photon into the desired mode.

Different schemes for multiplexing exist. Perhaps the simplest is *spatial* multiplexing: a set of N heralding sources are ran in parallel such that there is a high probability that at least one of these will produce a photon. Each output photon state enters a $N \times 1$ optical switch which is reconfigured using fast electronics to output one of the generated photons [199–201][1]. *Temporal* multiplexing uses a single heralded photon source, pumped multiple times. For any successful event, the photon is stored in either a quantum memory or a delay line and retrieved at a later time [203–205]. Finally, *spectral* multiplexing seeks to use a single cavity source to simultaneously attempt to create photons in a plurality of mode pairs [206–209]. The frequency of the heralded photon is now dependent on which mode had a successful generation event. Accordingly, there then needs to be a feed forward control to a nonlinear frequency conversion unit to ensure the output photon wavelength is correct [210, 211].

Accordingly, a promising method to create frequency multiplexed states is the *quantum frequency comb* [212]. These utilise a nonlinear medium inside of a cavity which when pumped below threshold generate signal and idler photon pairs in cavity modes of differing longitudinal mode number. This was first done in free space cavities with a $\chi^{(2)}$ crystal [170], generating high-dimensional quantum states [213] which have been shown to be a resource for measurement-based quantum computing [214]. However, the small FSRs associated with large, free-space, cavities make addressing each mode individually difficult. This problem can be solved by using smaller resonators with the $\chi^{(3)}$ nonlinearity, allowing the integration onto photonic chips, individual addressing of each mode, and having all operational wavelengths in the telecoms band. Such devices, which are simply the sub-threshold Kerr-comb, have been dubbed the *quantum microcomb* [215].

Quantum microcombs have been explored theoretically in Ref [53], and there has recently been significant experimental work to generate such states [216–221]. In particular, Ref [216] used a self-locked microring resonator inside of an external cavity to generate photon pairs in the ITU frequency bands used in telecoms. Ref [217] uses a similar approach, though including a pulsed pump configuration that also allows for time-bin entanglement of the generated photons. Ref [219] shows how the multi-modal nature of the quantum microcomb can be used to access, and control, high dimensional quantum states. Spectral correlations between the signal and idler photons from quantum microcombs can reduce the purity of the heralded single photon states, which would make them unusable for many applications. Ref [220] overcomes this issue by using a dual-pump to reduce these correlations, giving a photon purity of 98.0%. Ref [221] produces 20 pairs of entangled qumodes, using

[1]N.B. the efficiency of this process can be improved by using an $N \times M$ optical switch to reduce wasting successful photon generation events [202]

balanced photodetection to confirm quadrature squeezing.

Remark: Also of interest is the use of micro-resonators as the means for the coherent frequency conversion of light [222]. One can imagine the use of one micro-ring to generate a source of frequency-multiplexed single photons, each of which is split into a separate spatial mode and sent to a second micro-ring resonator for de-multiplexing to the required frequency [223].

This chapter expands on the aforementioned work on quantum micro-combs by considering how detuning effects degrade the generated states. Phase-matching is a vital requirement of any nonlinear optical process, and the frequency range over which it is satisfied for any Kerr-comb is set by three parameters: pump detuning, frequency dispersion, and nonlinearity. First, an analytic form of the logarithmic negativity between a pair of modes is given in terms of these parameters. Next, a description of the experimental process which has been undertaken to confirm these results is discussed along with proposed next steps. This is an important step in the development of quantum micro-combs; in order to maximise the number of qumodes available, and thus the dimension of the generated quantum state, an understanding of the effects of imperfect phase matching over a wide frequency range is required.

6.2 Theory

The physics of this Chapter matches that of Chapter 5 with only one caveat - this chapter focuses on sub-threshold effects, which are explored further. Below threshold, the pump mode couples into the cavity, but at a low enough power such that the parametric gain in the other modes is not high enough to compensate their respective losses. Accordingly, there is no lasing in any mode other than the pump - the classical fields are zero in all but the pump mode: $\mathcal{A}_l = 0, l \neq 0$.

Although the four-wave mixing gain is too low to allow the coherent build up of light in other modes, there is still the transfer of light between the modes. This can be thought of in the following manner: degenerate four-wave mixing leads to the annihilation of two photons from the pump mode, creating a signal and idler pair in modes $\pm l$. These photons, occupying a lossy cavity mode, will trickle out - either to the environment, or to an output waveguide - at a rate which exceeds the creation events. Interesting states of light are generated, just at insufficient levels to allow a coherent buildup.

In this sub-threshold regime, the dynamics of such quantum fluctuations in mode l, are given in a modified version of Eq. (5.5):

$$\delta\dot{\hat{a}}_l = -\left(\kappa_{\text{tot}} - i\left(\sigma - \frac{1}{2}\zeta_2 l^2\right)\right)\delta\hat{a}_l + \sum_s \sqrt{2\kappa_s}\hat{V}_{s,l} + ig_0\left(A_0^2\delta\hat{a}^\dagger_{-l} + 2\left|A_0\right|^2\delta\hat{a}_l\right), \quad (6.1)$$

where the latter term shows that mode l is only coupled to the opposite mode $-l$ that is equidistant from the pump. Accordingly, the sub-threshold system is necessarily bi-partite as the linearisation of the model inhibits any entanglement between the signal (idler) and pump modes in the absence of classical fields in the signal (idler) mode.

In a similar fashion to Chapter 5 we can fully characterise this bipartite state using the steady-state covariance matrix. With $\delta\hat{\boldsymbol{a}}_l = [\delta\hat{a}_l, \delta\hat{a}_{-l}]^T$, $\hat{\boldsymbol{V}}_{s,l} = \left[\hat{V}_{s,l}, \hat{V}_{s,-l}\right]^T$, we have a bipartite equivalent of Eq. (5.11):

$$\begin{bmatrix} \delta\dot{\hat{\boldsymbol{a}}}_l \\ \delta\dot{\hat{\boldsymbol{a}}}_l^\dagger \end{bmatrix} = \begin{bmatrix} R_l\mathbb{1}_2, & S_l\boldsymbol{\sigma}_x \\ S_l^\star\boldsymbol{\sigma}_x, & R_l^\star\mathbb{1}_2 \end{bmatrix} \begin{bmatrix} \delta\hat{\boldsymbol{a}}_l \\ \delta\hat{\boldsymbol{a}}_l^\dagger \end{bmatrix} + \sum_s \sqrt{2\kappa_s} \begin{bmatrix} \hat{\boldsymbol{V}}_{s,l} \\ \hat{\boldsymbol{V}}_{s,l}^\dagger \end{bmatrix}, \tag{6.2}$$

where R_l is given by:

$$\begin{aligned} R_l &= -\left(\kappa_{\text{tot}} - i\left(\sigma - \frac{1}{2}\zeta_2 l^2 + 2g_0\left|A_0\right|^2\right)\right), \\ &= -\kappa_{\text{tot}} + i\Delta_{\text{eff},l}, \end{aligned} \tag{6.3}$$

and S_l is given by:

$$S_l = ig_0A_0^2, \tag{6.4}$$

where $\mathbb{1}_2$ is the two dimensional identity operator and $\boldsymbol{\sigma}_x$ the Pauli x-matrix and all the pseudo-detuning terms are brought together into a single effective detuning parameter $\Delta_{\text{eff},l}$ (N.B. this parameter encompasses all of the physical effects that act as detunings: actual detuning of the pump laser, nonlinearity and dispersion). The quadrature basis is here defined by the transforms:

$$\begin{bmatrix} \delta\hat{\boldsymbol{X}}_l \\ \delta\hat{\boldsymbol{Y}}_l \end{bmatrix} = \frac{1}{\sqrt{2}} \begin{bmatrix} 1, & 1 \\ -i, & i \end{bmatrix} \otimes \mathbb{1}_2 \begin{bmatrix} \delta\hat{\boldsymbol{a}}_l \\ \delta\hat{\boldsymbol{a}}_l^\dagger, \end{bmatrix} \tag{6.5a}$$

$$\begin{bmatrix} \delta\hat{\boldsymbol{a}}_l \\ \delta\hat{\boldsymbol{a}}_l^\dagger \end{bmatrix} = \frac{1}{\sqrt{2}} \begin{bmatrix} 1, & i \\ 1, & -i \end{bmatrix} \otimes \mathbb{1}_2 \begin{bmatrix} \delta\hat{\boldsymbol{X}}_l \\ \delta\hat{\boldsymbol{Y}}_l \end{bmatrix}, \tag{6.5b}$$

with Eq. (6.2) in this basis (here the pump field A_0 is taken to be real for simplicity without loss of generality) becoming:

$$\begin{bmatrix} \delta\dot{\hat{\boldsymbol{X}}}_l \\ \delta\dot{\hat{\boldsymbol{Y}}}_l \end{bmatrix} = \begin{bmatrix} -\kappa_{\text{tot}}\mathbb{1}_2, & g_0\left|A_0\right|^2\boldsymbol{\sigma}_x - \Delta_{\text{eff},l}\mathbb{1}_2 \\ g_0\left|A_0\right|^2\boldsymbol{\sigma}_x + \Delta_{\text{eff},l}\mathbb{1}_2, & -\kappa_{\text{tot}}\mathbb{1}_2 \end{bmatrix} \begin{bmatrix} \delta\hat{\boldsymbol{X}}_l \\ \delta\hat{\boldsymbol{Y}}_l \end{bmatrix} + \sqrt{\kappa_{\text{tot}}} \begin{bmatrix} \hat{\boldsymbol{X}}_l^{\text{in}} \\ \hat{\boldsymbol{Y}}_l^{\text{in}} \end{bmatrix}, \tag{6.6}$$

where all vacuum fluctuation operators have been combined into single input noise operators. The steady-state covariance matrix associated with these dynamics, from Eq. (5.20), can be solved analytically to give:

$$\boldsymbol{V}_l = \begin{bmatrix} v_{\text{a},l}, & -v_{\text{b},l}, & 0, & v_{\text{c},l} \\ -v_{\text{b},l}, & v_{\text{a},l}, & v_{\text{c},l}, & 0 \\ 0, & v_{\text{c},l}, & v_{\text{a},l}, & v_{\text{b},l} \\ v_{\text{c},l}, & 0, & v_{\text{b},l}, & v_{\text{a},l} \end{bmatrix}, \tag{6.7a}$$

$$v_{\text{a},l} = \frac{\kappa_{\text{tot}}^2 + \Delta_{\text{eff},l}^2}{2\left(\kappa_{\text{tot}}^2 + \Delta_{\text{eff},l}^2 - g_0^2\left|A_0\right|^4\right)}, \tag{6.7b}$$

$$v_{\text{b},l} = \frac{g_0\left|A_0\right|^2\Delta_{\text{eff},l}}{2\left(\kappa_{\text{tot}}^2 + \Delta_{\text{eff},l}^2 - g_0^2\left|A_0\right|^4\right)}, \tag{6.7c}$$

$$v_{\text{c},l} = \frac{g_0\left|A_0\right|^2\kappa_{\text{tot}}}{2\left(\kappa_{\text{tot}}^2 + \Delta_{\text{eff},l}^2 - g_0^2\left|A_0\right|^4\right)}. \tag{6.7d}$$

6.2.1 Comparison to a two-mode squeezed vacuum

The covariance matrix for a sub-threshold Kerr comb can be compared to that of a TMSV. The TMSV can be given by:

$$|\xi\rangle = S(\xi)\,|0,0\rangle\,, \tag{6.8}$$

$$= \exp\left(\xi\hat{a}^\dagger\hat{b}^\dagger - \xi^\star\hat{a}\hat{b}\right)|0,0\rangle\,, \tag{6.9}$$

where the squeezing parameter $\xi = re^{i\phi}$. The associated Hamiltonian looks similar to that of the sub-threshold Kerr-comb where the squeezing parameter is given by $\xi = -ig_0A_0^2$. The covariance matrix for such a state, where $\phi = \frac{\pi}{2}$, can be shown to be (see Appendix B):

$$\boldsymbol{V}_{\text{TMSV}} = \begin{bmatrix} \frac{\cosh(2r)}{2}, & 0, & 0, & \frac{\sinh(2r)}{2} \\ 0, & \frac{\cosh(2r)}{2}, & \frac{\sinh(2r)}{2}, & 0 \\ 0, & \frac{\sinh(2r)}{2}, & \frac{\cosh(2r)}{2}, & 0 \\ \frac{\sinh(2r)}{2}, & 0, & 0, & \frac{\cosh(2r)}{2} \end{bmatrix}. \tag{6.10}$$

Contrary to the work reported in [53], this does not seem to be comparable to the sub-threshold Kerr comb. However, for $\Delta_{\text{eff},l} = 0$ and $g_0\,|A_0|^2 \ll \kappa_{\text{tot}}$ (i.e. for strong phase matching and well below threshold) it can be shown to agree using the first order expansions of the hyperbolic functions. In this case, the associated squeezing parameter has magnitude $r = \frac{g_0|A_0|^2}{2\kappa_{\text{tot}}}$ and is much less than unity.

6.2.2 Logarithmic negativity

The logarithmic negativity of the TMSV can be shown using Eq. (5.23) to be $E_{\mathcal{N}} = 2r$. Using this same method with the covariance matrix of the sub-threshold Kerr comb - Eq. (6.7) - can give the (somewhat cumbersome) analytic expression:

$$E_{\mathcal{N}} = \frac{1}{2}\ln\left(\frac{(1+D^2-G^2)}{D^4 - D^2\,(G^2-2) + G^2 - 2G\sqrt{D^4 - D^2\,(G^2-2)+1} - 1}\right), \tag{6.11a}$$

$$G = \frac{g_0\,|A_0|^2}{\kappa_{\text{tot}}}, \tag{6.11b}$$

$$D = \frac{\Delta_{\text{eff},l}}{\kappa_{\text{tot}}}. \tag{6.11c}$$

This value is only well defined for arbitrary detunings when $g_0\,|A_0|^2 < \kappa_{\text{tot}}$, a consequence of the analysis only being valid for sub-threshold situations. Figure 6.1 shows these values for the region of interest.

6.2.3 Motivation

Approximating to the TMSV, sub-threshold Kerr-combs are an exciting method to generate multi-partite quantum states for a variety of information processing and communication applications [175]. In particular, when the squeezing parameter is low the TMSV can be used as a source of entangled photon pairs - the key component of a heralded single-photon source. Eq. (6.9) can be expanded in the Fock basis to:

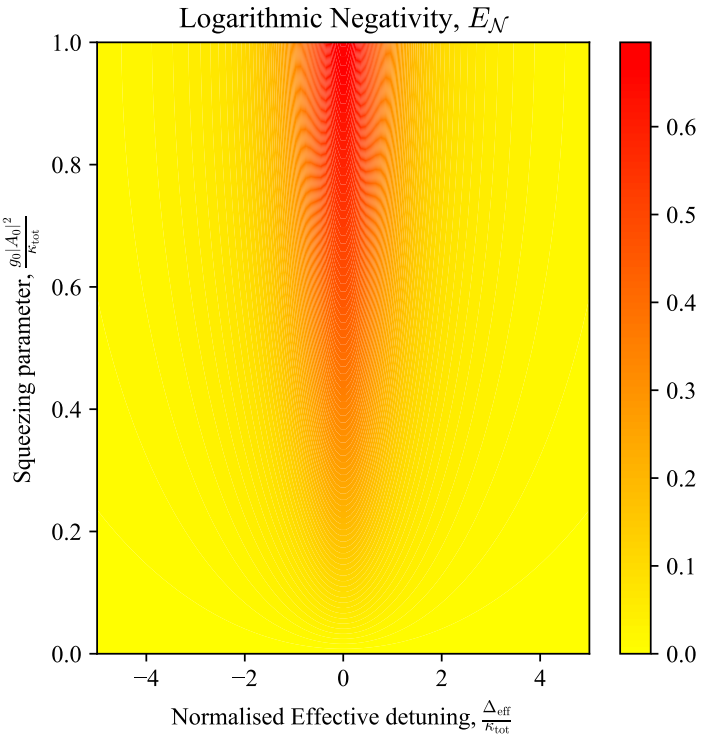

Figure 6.1: Logarithmic negativity of sub-threshold Kerr comb modes as a function of input power and effective detuning.

$$|\xi\rangle = \frac{1}{\cosh(r)} \sum_{n}^{\infty} e^{in\phi} \tanh^{n}(r) |n, n\rangle , \tag{6.12}$$

which has the probability of having a photon occupancy of n as being:

$$p_n = |\langle n|\xi\rangle|^2 = \frac{\tanh^{2n}(r)}{\cosh^2(r)}. \tag{6.13}$$

For a heralded *single* photon source, the presence of a photon state in the heralding mode - affectionately referred to as a "click" in a photon detector - would only happen when there was a *single* photon in the heralded mode. Accordingly it is undesirable to have any photon state where $n > 1$. The probability of heralding a *single* photon state given a click from the heralding mode is then given by:

$$p_{n=1|n>0} = 1 - \tanh^2(r), \tag{6.14}$$

which is greater than 99% for $r \leq 0.1$. Accordingly, sub-threshold Kerr comb modes that have low effective detunings and low squeezing parameters are a promising source of heralded single-photons.

However, section 6.2.1 has shown that the dynamics of the system are somewhat richer than the pure TMSV, which further motivates experimental investigation of this regime. The remainder of this chapter will detail the work that has been undertaken at the time of writing, the challenges that have been encountered, and proposed methods to characterise these states.

6.3 Experimental work

The previous section describes how the sub-threshold Kerr comb approximates a squeezed vacuum for small effective detunings and squeezing levels. During the course of this thesis, significant experimental work was undertaken to demonstrate and characterise the quantum nature of these states, with progress limited by device performance. This section will detail the work completed thus far, along with the challenges that need to be addressed.

6.3.1 Experimental setup

Figure 6.2 shows the experimental setup for generating a sub-threshold Kerr-comb. Light from an external cavity diode laser (ECDL) is amplified by an erbium doped fiber amplifier (EDFA) to the required power. Both of these processes generate broadband noise by (amplified) spontaneous emission, which would ultimately be detrimental to the system by generating unwanted photons in the same frequency bins as those created by four-wave mixing. Thus, this noise is rejected using a narrowband tunable filter.

The pump field, as has been described in section 4.3, is coupled into the resonator via a polarisation controller (to match the input and cavity polarisation states) and tapered optical fiber. Spontaneous four-wave mixing between the cavity modes leads to the generation of squeezed states, which then couple out of the resonator into the tapered fiber.

To ensure the system remains sub-threshold - i.e. that there is only one lasing mode inside the resonator - 1% of the output is sent, via a beam splitter, to an optical spectrum analyser. The input laser power/detuning is then set such that no sidebands are observed.

In order to split each of the frequency modes of the resonator for further investigation, a dense wavelength division multiplexer (DWDM) is used. However, these devices still exhibit residual cross-coupling between frequency channels, meaning that the unfiltered strong pump - relative to the single-photon level signals in the other modes - will dominate. Accordingly a further tunable filter (or indeed a series of them) is used to selectively filter out the pump frequency before the DWDM. This signal rejected from the filter (i.e. the pump) is then sent to a photodiode (PD) and monitored on an oscilloscope to determine the frequency of the laser in comparison to the cavity resonances. DWDMs are commercially available devices, commonly used to (de)multiplex different frequency channels in optical fiber for telecoms applications. These channels are spaced by 100 GHz (some allow 50 GHz) and the diameter of the microresonator was designed so that the FSR matched this spacing. For a fused silica WGM resonator, this corresponds to a diameter of 660 µm, which can be accurately fabricated as a rod resonator as described in section 2.2.2.

6.3.2 Method for photon-pair generation

Using this setup, the following method can be used to generate photon pairs in the output fibers from the DWDM.

1. *Set the laser frequency inside the central DWDM channel.* DWDMs have frequency channels according to the ITU specifications, which have channels

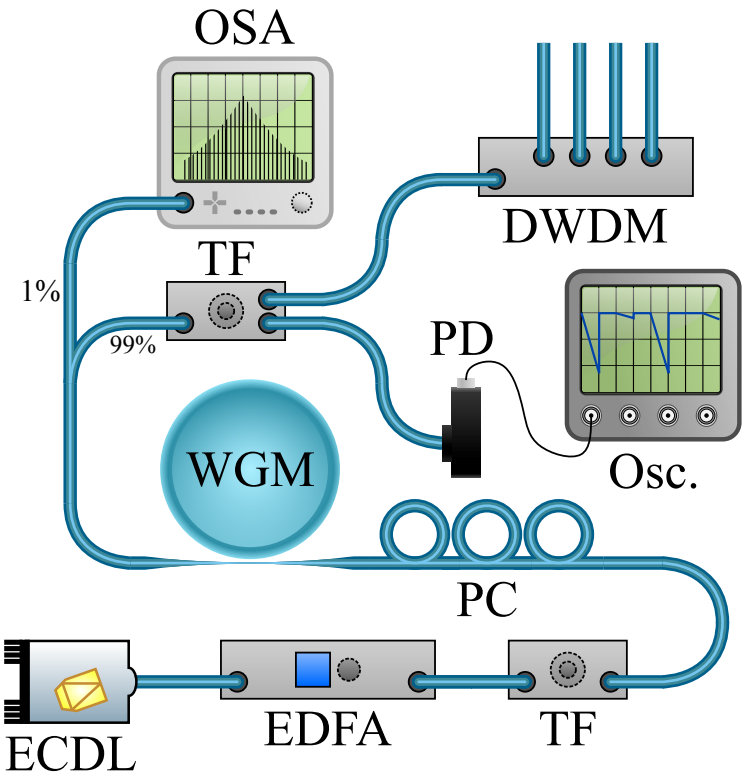

Figure 6.2: Experimental setup for the generation of a two-mode squeezed vacuum (TMSV) state. Light from an external cavity diode laser (ECDL) is amplified by an erbium-doped fiber amplifier (EDFA). Broadband noise is rejected using a tunable filter (TF) and this light has its polarisation set to that of a cavity mode using a polarisation controller (PC). The light then enters a whispering gallery mode resonator (WGM) via a tapered fiber, with some proportion of the cavity field also coupling out into the tapered fiber. 1% of this output is sent to an optical spectrum analyser (OSA) to monitor sideband formation, with the remainder going through a further tunable filter. The light reflected from the filter - corresponding to the pump frequency - is sent to a photodiode (PD) and observed on an oscilloscope (Osc.). The filter transmission - corresponding to any light generated in the resonator at frequencies different to the pump - is split into different frequency modes for further experimentation using a dense wavelength division multiplexer (DWDM).

separated by 100 GHz. The specific device used in this study used ITU channels 30-37 (1553.33 nm - 1547.72 nm) such that the pump can be centred on channel 34 (1550.12 nm) which has the lowest loss in standard optical fiber.

2. *Tune the filters.* Both filters in Fig. 6.2 need to be tuned to the correct frequency. This is completed in two stages, using the OSA to monitor the transmission window of the first filter and tuning it such that the laser transmits through it. The second filter is then set by maximising the photodiode output on the oscilloscope.

3. *Search for resonances that exhibit stimulated four wave mixing.* In this stage, the OSA is used to find resonances for which sidebands are generated via stimulated four-wave mixing. Although these sidebands are not actually wanted in the exploration of sub-threshold dynamics, they indicate that the resonances are of the required quality. In this process, the laser frequency must be swept over multiple resonances, with the polarisation controller and taper position adjusted to optimise the associated nonlinear effects - in practice this is maximising the width of the resonances that are broadened by thermal and Kerr nonlinearities, as described in section 2.3.10. This process is iterated until sidebands are seen on the OSA, identifying a suitable resonance for further study. DWDM channels have a relatively large bandwidth of 10 GHz to allow for high bitrate telecoms signals, meaning that finding a suitable resonance in this spectral region is likely. If this were not the case, thermal tuning of the resonator could be used to bring suitable resonances into this required region.

4. *Reduce input power.* The power is now reduced until the sidebands are no longer observed, giving a good approximation to the threshold power. The power can be further reduced to explore the full range of the sub-threshold regime.

5. *Couple into resonance.* As described in section 2.3.10, the laser can be passively locked to a resonance via the thermal nonlinearity. In practice this is done by progressively reducing the laser frequency scan range whilst keeping the center of the scan inside the resonance. When the scan has reduced to zero amplitude, the laser is passively locked to the resonance and the detuning can be monitored using the photodiode output (lower voltage means less light is transmitted through the tapered fiber implying the input is closer to resonance, i.e. lower detuning).

6. *Choose DWDM output fibers.* Having now found a resonance that exhibits four-wave mixing inside a DWDM channel, output fibers are chosen that should have mutually entangled output fields. These are chosen such that they are spectrally equidistant from the pump, i.e. if the pumped mode is in channel 34, the channel pairs 33 : 35, 32 : 36 or 31 : 37 can be chosen.

6.3.3 Superconducting nanowire single photon detectors

During this work, a set of superconducting nanowire single photon detectors (SNSPDs) was assembled and configured. These devices have lower dark counts and

higher detection probabilities and temporal resolution than single photon avalanche diodes (SPADs), and do not require to be gated.

The operating principle is as follows: a nanowire is patterned in a spiral-type shape such that it covers a wide area. It is cooled in a cryostat to below its superconducting critical temperature and a bias current that is close to, but below, the critical current is applied. Incident photons are then absorbed by Cooper pairs of superconducting electrons, breaking superconduction and leading to a voltage spike across the device. So long as the bias current is low enough to ensure that ohmic heating doesn't permanently break superconduction, the device then cools back into a superconducting state ready to signal the arrival of subsequent photons.

The relative arrival time of photons incident to each of the detectors in the cryostat are then measured by a time tagger, which allows for temporal correlations between different spatial modes to be established.

6.3.4 Pump suppression

The main experimental difficulty in this work is the separation of the strong pump from the single-photon-level signals that are being investigated. Section IV.C. of Ref [53] gives a method to calculate the output photon flux from spontaneous four-wave mixing inside a resonator and this was calculated to be $\approx$ 100 dB below that associated with the pump for the resonator parameters estimated from the experiment.

If not suitably suppressed prior to input to the DWDM, each of the outputs will be dominated by the crosstalk from the pump. This is exactly the problem that has been faced in experiment; the insufficient suppression of the pump masking the signals of interest.

At the time of writing, the level of suppression that has been established gives output photons that are $15 - 20\%$ likely to be from four-wave mixing, rather than simply being an unfiltered pump photon. This is calculated by sending the DWDM output to SNSPDs, and measuring the associated photon count rate. When the laser is far detuned from resonance, all of these photons will be a mix of dark counts from the environment (found to be of negligible amount) and unfiltered pump photons. As we tune into resonance, pump light couples into, and is lost inside, the resonator. Accordingly, the pump photon count rate can only go down when tuning into a resonance. Instead the count rate is seen to increase, indicating the creation of photons in this frequency range by FWM. The difference between this higher value and the original, FWM free, count rate gives a lower bound for the proportion of photons that are from FWM.

Unfortunately, this level was not high enough to see any interesting signals (e.g. heralded sub-Poissonian photon statistics). At the time of writing, further tunable filters are being added to the experiment to further suppress the pump in this pursuit.

6.4 Conclusion

This chapter presents the initial work undertaken to demonstrate detuning effects on the quantum states generated by a sub-threshold Kerr-comb. First, an analytic form of the associated entanglement between the modes is presented, followed by

a discussion on the experimental endeavours to explore these effects. Ultimately, insufficient pump suppression prevented the completion of this work, which can be solved with improved wavelength filtering. This work will be an important step in the understanding of the applicability of Kerr-combs as a platform for different quantum technologies.

6.5 Outlook

This section will describe subsequent steps in the experiment once further tunable filters are delivered to better suppress unwanted pump photons.

6.5.1 Temporal correlation of photon pairs

Degenerate FWM annihilates a pair of pump photons, simultaneously creating a signal and idler pair in the $\pm l$ modes of the resonator. Accordingly, there should be a strong correlation in the timing of the clicks from the SNSPDs that are connected to output fibers of the DWDM that correspond to these $\pm l$ modes.

The finite bandwidth of these modes, giving the photons themselves a finite bandwidth, means they are not perfectly localised in time. Instead, after the FWM creation event, both of the photons "leak" out of the cavity, giving them a temporal envelope that would be interesting to characterize.

This temporal profile can be measured in the following way: take the time a photon is measured in mode $-l$ to be $\tau = 0$. Measure the time difference between this event and the measurement of a sister photon in mode $+l$ as τ. Time binning such results over many measurements then allows for the build up of the temporal profile of the photons in mode l.

This process illuminates a number of interesting things about the system in question. Firstly, losses in the system mean that for each photon measured in mode $-l$ there is not necessarily going to be a partner measured in $+l$. These losses, which come from scattering from the resonator to the environment (which can be reduced by overcoupling) and losses within the fiber/filters/DWDM, are useful for knowing the heralding efficiency of the system when used as a single-photon source. Secondly, the temporal width of these photons is linked to the linewidth and effective phase matching of the modes the photons are generated in. It would be interesting to see whether factors which affect this phase matching, such as cavity dispersion, affects the linewidth of the photons. This will be particularly interesting as it could affect the associated purity of the photons (see section 6.5.3).

6.5.2 Second order temporal coherence, $g^{(2)}(\tau)$

A useful metric in quantum optics is the second-order temporal coherence, $g^{(2)}(\tau)$, as for classical optics $g^{(2)}(0) \geq 1$ and this inequality can *only* be broken for a quantum state. For low photon-number signals, this can be experimentally measured by sending a mode through a beam splitter into two separate SNSPDs and measuring the relative timing of detection events [224].

For the TMSV state that is here discussed, ignoring one mode - equivalent to partially tracing over it - leaves the other in a thermal state. This (classical) state shows photon bunching, with $g^{(2)}(0) > 1$. In Fig 6.3 this would mean that a photon

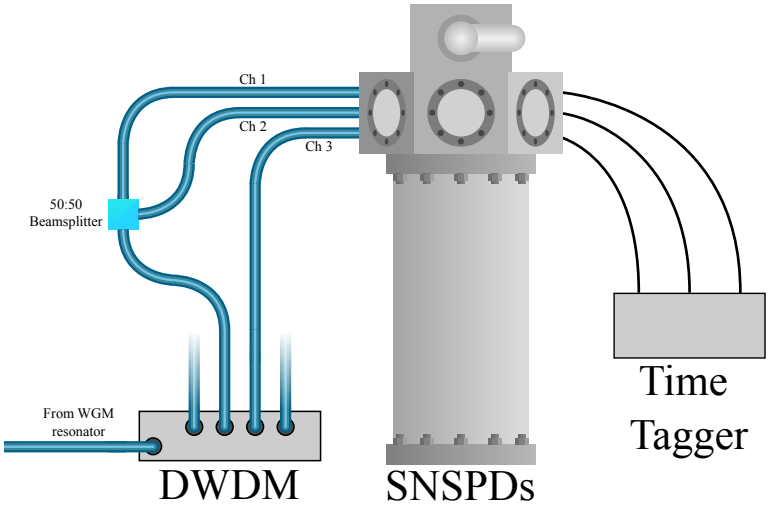

Figure 6.3: Proposed setup to measure the $g^{(2)}(\tau)$ of the generated states. The $\pm l$ modes are separated from the output of the DWDM. One of these, say mode $-l$, is sent through a beam splitter into channels 1 and 2 of the SNSPDs. Ignoring mode $+l$, which is sent to channel 3, projects mode $-l$ into a thermal state and so photon bunching is seen between channels 1 and 2 ($g^{(2)}(0) > 1$). However, conditioning these measurements on a click in channel 3 projects the system into a single-photon state which should demonstrate anti-bunching ($g^{(2)}(0) \to 0$).

measured in Ch 1 will imply a higher likelihood of measuring a photon in Ch 2 immediately before/after than normal. If the filtering and measurement procedure work well, an ideal thermal state with $g^{(2)}(0) = 2$ could be approached.

Instead, photon anti-bunching should be seen in this mode when the measurement is conditioned on the measurement of a photon in its partner. Conditioning here means that measurements on Ch 1 and Ch-2 are *only* considered when there has been a click in Ch-3. This click in Ch-3 projects the other mode into a single photon state (higher photon number states are suppressed by using suitably low pump power). This single photon cannot further split, and so there *will* be a click in *either* Ch-1 *or* Ch-2, but there *cannot* be simultaneous clicks in both. This photon *anti*bunching is associated with $g^{(2)}(0) < 1$ and is evidence of the quantum nature of the state.

In particular, the actual value of $g^{(2)}(0)$ gives a sense for the photon occupancy of the state. For a Fock state, $|n\rangle$ (i.e. the n-photon state), the second order temporal coherence with zero delay is given by [195]:

$$g^{(2)}(0) = 1 - \frac{1}{n} \tag{6.15}$$

Accordingly, for the single-photon state, $g^{(2)}(0) = 0$. A value of $g^{(2)}(0) < 0.5$ indicates that the photon occupancy of the state $\overline{n} < 2$, and so is taken as an indicator of a single photon state. However, the value should be minimised so as to suppress unwanted effects from higher photon occupancies.

The value of $g^{(2)}(0)$ can be related to the squeezing parameter r and so makes a useful metric to characterise the differences in mode pairs of the sub-threshold

Kerr comb. Higher r leads to an increased generation rate of photon states (often called the "brightness" of the source) which is beneficial as it allows for increased operational speed of whichever device employs such states. However, this comes at the cost of increasing $g^{(2)}(0)$, increasing the likelihood of heralding a multi-photon state, which would degrade the operational accuracy of the device. Accordingly in practice there is often a compromise made on the levels of squeezing employed.

6.5.3 Spectral/temporal purity

An ideal single-photon source would have a high-purity output such that generated photons are indistinguishable. This is required for their mutual interference, a requirement for most interesting applications e.g. quantum photonic computation [159].

Residual frequency correlations between the heralding and heralded photons can degrade this purity. For a monochromatic pump, the signal and idler photons created by FWM are perfectly correlated in frequency with some spectral bandwidth set by the resonator lineshape. The heralding detection of one of these photons destroys its frequency information, equivalent to a trace over this parameter, leaving the other in an incoherent mixture of frequencies.

Pulsed pumping goes some way to alleviate these issues, as the ambiguity in the frequencies of the annihilated pump photons reduces the residual frequency correlations between the signal and idler photons [220, 225]. Moreover, using a Mach-Zender interferometer (MZI) coupling setup can change the relative linewidths of the pump, signal and idler modes, further increasing the pump photon frequency ambiguity and improving the associated purity [226].

A proposed idea would be to use cavity dispersion to effectively narrow the linewidths of the signal and idler photons, due to the narrower window of effective phase matching. Thus the relative frequency ambiguity of the pump photons can again be increased, potentially giving the benefits of the MZI setup without the associated experimental difficulties.

6.5.4 Optomechanical coupling

Finally, an interesting application of this system as a single-photon source would be its coupling to a WGM optomechanical resonator. Strong coupling between optical and mechanical fields have been seen in such devices mediated by Brillouin scattering [227]. The similarity in linewidths between these modes and those of the photons generated in this work imply they should interact strongly, with a photon generated in one WGM resonator, coupling into another and being converted into a phonon by Brillouin scattering to be retrieved by a read-pulse at a later time. Accordingly, this work could constitute an important part of an integrated quantum optical memory.

Chapter 7

Conclusion

The aim of this thesis was to investigate the applicability of Kerr microresonators as a platform for future classical and quantum technologies.

Microresonators have been shown to have high Q-factors, allowing for the integration of Kerr-nonlinearities into photonic circuits. This nonlinearity can exhibit two separate phenomena: the intensity dependent refractive index, and four-wave mixing. This work has shown how these effects can be used as the basis for various technologies.

In fabricating a polarisation degenerate, high finesse, fiber Fabry-Pérot cavity, it has been shown that the nonlinear refractive index can lead to a splitting of the degenerate modes, with the cavity field spontaneously developing a chirality even though the rest of the system has none. This is not only interesting in of itself, it was also shown to be a method for the all-optical control of an optical field's polarisation, which could find application in any photonic circuit for which polarisation must be controlled but the current fabrication techniques are prohibitive. Such cavities should be investigated further as they are a promising architecture to study the nonlinear interactions of polarisation modes - in particular, an enhancement to the sensitivity of a field's polarisation could find many applications.

The same splitting of degenerate modes, though of the counter-propagating modes in a whispering-gallery mode resonator, was then demonstrated as a useful platform for all-optical logic. The main benefits of this system in comparison to others was the fact that a universal logic gate was presented and all fields could operate at the same frequency. Accordingly, such a device could be replicated multiple times into a complex photonic circuit in which an optical signal can be routed from a given input to a chosen output port without the latency associated with converting the signal to the electronic domain. With the rise of distributed computing in data centres with information communicated between individual cores via fiber optics, and the increase in demand for latency free telecommunication, such a device could improve internet and high power computing performance.

Finally, four-wave mixing was investigated as a source of entanglement for quantum optics applications. Numerical simulations were performed to determine the logarithmic negativity (the magnitude of entanglement) between each pair of modes in a Kerr frequency comb. The sub-threshold regime was deemed worthy of further study, leading to an analytic solution for the logarithmic negativity in terms of the relevant parameters: detuning, dispersion and nonlinearity.

It was then decided to experimentally verify these theoretical results in an ex-

periment that uses single photon detectors to measure coincidence counts of photon pairs that are associated with the two-mode squeezed vacuum. Good progress was made on this experiment, but in order to see signals that are indicative of quantum effects, there needs to be improved pump suppression to reduce false "clicks" from the photon detectors. Such experimental investigations are interesting and worthy of further work as these systems can be used as heralded single photon sources for photonic quantum computing and quantum key distribution applications, and this investigation will lead to a better understanding of limitations to the system.

The Kerr effect in microresonators shows promise for utilisation in future photonic circuit devices. In particular, their ability to support multiple optical modes which can mutually couple via the material nonlinearity allows for the realisation of bistable systems. Such systems are important for the development of all-optical controllable devices, necessary for optical information processing. In particular, the high intrinsic Q-factors from such resonators allow for the development of devices for real-world application, as this allows low-power operation (though at the cost of operating speed). Furthermore, there are fabrication methods available which would allow such devices to be reliably and repeatedly integrate into photonic chips.

Such resonators also show promise for the generation of quantum optical states. Again, for such devices to be scalable, they require low power operation and the ability to be integrated on-chip. The frequency selective nature of optical cavities means that the optical states generated inside of them are naturally multi-modal. Accordingly, the Kerr effect can be used to generate multi-modal entangled states. When operated below threshold - i.e. with no sideband modes lasing - these systems can be used as a frequency multiplexed source of heralded single photons, an important device for quantum optical technologies. The main issues with using such devices for quantum technologies is: *out-coupling*, ensuring that the generated quantum states exit the device without loss, and *pump suppression*, as the strong pump field can wash out any quantum effects without adequate filtering. Such difficulties in operation are mitigated by the high intrinsic Q-factors of such devices, which allow for the exploitation of nonlinear effects even in the presence of high out-coupling. Also, the Kerr effect ensures that all generated sidebands are similar in frequency to the pump, which makes filtering difficult, but has benefits in terms of allowing all modes to exist at telecoms wavelengths - allowing the employment of off-the-shelf componenets.

In summary, this body of work constitutes a series of advancements in the knowledge and opportunities available to (quantum) photonic circuit design. Kerr microresonators allow the realisation of low-power, on-chip, all-optical devices that can be used for a plethora of real-world applications. Progressing our ability to have light self-interact in non-trivial ways promises to launch new and exciting areas of technology.

Bibliography

[1] T. H. Maiman, "Stimulated optical radiation in ruby," *Nature 1960 187:4736*, vol. 187, pp. 493–494, 4736 1960, ISSN: 1476-4687. DOI: 10.1038/187493a0.

[2] J. Bardeen and W. H. Brattain, "The transistor, a semi-conductor triode," *Physical Review*, vol. 74, pp. 230–231, 2 Jul. 1948, ISSN: 0031899X. DOI: 10.1103/PHYSREV.74.230/FIGURE/1/THUMB.

[3] M. D. Al-Amri, M. M. El-Gomati, and M. S. Zubairy, *Optics in Our Time*, 1st ed. Springer, Cham, 2016. DOI: https://doi.org/10.1007/978-3-319-31903-2.

[4] A. Einstein, "Über einen die erzeugung und verwandlung des lichtes betreffenden heuristischen gesichtspunkt," *Annalen der Physik*, vol. 322, pp. 132–148, 6 Jan. 1905, ISSN: 1521-3889. DOI: 10.1002/ANDP.19053220607.

[5] H. Kragh, *Max planck: The reluctant revolutionary*, P. World, Ed.

[6] J. A. Rarick, "A short review of fiber-optics technology," *University of Kentucky, Office of Engineering Services, (Bulletin) UKY BU*, pp. 157–167, Jan. 1987, ISSN: 02706504. DOI: 10.1016/B978-0-409-90052-1.50024-1.

[7] J. Wei, "Laser heat-mode lithography," vol. 291, 2019. DOI: 10.1007/978-981-15-0943-8.

[8] H. M. Gibbs, S. L. McCall, and T. N. C. Venkatesan, "Differential gain and bistability using a sodium-filled fabry-perot interferometer," *Phys. Rev. Lett.*, vol. 36, pp. 1135–1138, 19 May 1976. DOI: 10.1103/PhysRevLett.36.1135.

[9] H. M. Gibbs, "Chapter 1 - introduction to optical bistability," in *Optical Bistability: Controlling Light with Light*, H. M. Gibbs, Ed., Academic Press, 1985, pp. 1–17, ISBN: 978-0-12-281940-7. DOI: https://doi.org/10.1016/B978-0-12-281940-7.50006-8.

[10] J. A. Goldstone and E. Garmire, "Intrinsic optical bistability in nonlinear media," *Phys. Rev. Lett.*, vol. 53, pp. 910–913, 9 Aug. 1984. DOI: 10.1103/PhysRevLett.53.910.

[11] H. M. Gibbs, "Chapter 5 - optical switching: Controlling light with light," in *Optical Bistability: Controlling Light with Light*, H. M. Gibbs, Ed., Academic Press, 1985, pp. 195–239, ISBN: 978-0-12-281940-7. DOI: https://doi.org/10.1016/B978-0-12-281940-7.50010-X.

[12] ——, "Chapter 7 - toward practical devices," in *Optical Bistability: Controlling Light with Light*, H. M. Gibbs, Ed., Academic Press, 1985, pp. 305–335, ISBN: 978-0-12-281940-7. DOI: https://doi.org/10.1016/B978-0-12-281940-7.50012-3.

[13] E. Garmire *et al.*, "Nonlinear optics in daily life," *Optics Express, Vol. 21, Issue 25, pp. 30532-30544*, vol. 21, pp. 30 532–30 544, 25 Dec. 2013, ISSN: 1094-4087. DOI: 10.1364/OE.21.030532.

[14] J. L. Hall, "Nobel lecture: Defining and measuring optical frequencies," *Reviews of Modern Physics*, vol. 78, pp. 1279–1295, 4 Nov. 2006, ISSN: 00346861. DOI: 10.1103/REVMODPHYS.78.1279/FIGURES/4/MEDIUM.

[15] T. W. Hänsch, "Nobel lecture: Passion for precision," *Reviews of Modern Physics*, vol. 78, pp. 1297–1309, 4 Nov. 2006, ISSN: 00346861. DOI: 10.1103/REVMODPHYS.78.1297/FIGURES/3/MEDIUM.

[16] T. Fortier and E. Baumann, "20 years of developments in optical frequency comb technology and applications," *Communications Physics 2019 2:1*, vol. 2, pp. 1–16, 1 Dec. 2019, ISSN: 2399-3650. DOI: 10.1038/s42005-019-0249-y.

[17] P. Del'haye, A. Schliesser, O. Arcizet, T. Wilken, R. Holzwarth, and T. J. Kippenberg, "Optical frequency comb generation from a monolithic microresonator," vol. 450, 2007. DOI: 10.1038/nature06401.

[18] B. Shen *et al.*, "Integrated turnkey soliton microcombs," *Nature*, vol. 582, pp. 365–369, 7812 Jun. 2020, ISSN: 14764687. DOI: 10.1038/s41586-020-2358-x.

[19] E. Knill, R. Laflamme, and G. J. Milburn, "A scheme for efficient quantum computation with linear optics," *Nature*, vol. 409, no. 6816, pp. 46–52, Jan. 2001. DOI: 10.1038/35051009.

[20] P. Shor, "Algorithms for quantum computation: Discrete logarithms and factoring," pp. 124–134, 1994. DOI: 10.1109/SFCS.1994.365700.

[21] F. Xu, X. Ma, Q. Zhang, H.-K. Lo, and J.-W. Pan, "Secure quantum key distribution with realistic devices," *Rev. Mod. Phys.*, vol. 92, p. 025 002, 2 May 2020. DOI: 10.1103/RevModPhys.92.025002.

[22] H. J. Kimble, M. Dagenais, and L. Mandel, "Photon antibunching in resonance fluorescence," *Physical Review Letters*, vol. 39, p. 691, 11 Sep. 1977, ISSN: 00319007. DOI: 10.1103/PhysRevLett.39.691.

[23] D. F. Walls, "Squeezed states of light," *Nature 1983 306:5939*, vol. 306, pp. 141–146, 5939 1983, ISSN: 1476-4687. DOI: 10.1038/306141a0.

[24] M. Tse *et al.*, "Quantum-enhanced advanced ligo detectors in the era of gravitational-wave astronomy," *Physical Review Letters*, vol. 123, p. 231 107, 23 Dec. 2019, ISSN: 10797114. DOI: 10.1103/PHYSREVLETT.123.231107/FIGURES/2/MEDIUM.

[25] R. W. Boyd, *Nonlinear Optics*, 4th ed. Elsevier Science, 2020, p. 634, ISBN: 9780323850575.

[26] R. E. Slusher, L. W. Hollberg, B. Yurke, J. C. Mertz, and J. F. Valley, "Observation of squeezed states generated by four-wave mixing in an optical cavity," *Physical Review Letters*, vol. 55, p. 2409, 22 Nov. 1985, ISSN: 00319007. DOI: 10.1103/PhysRevLett.55.2409.

[27] L. A. Wu, H. J. Kimble, J. L. Hall, and H. Wu, "Generation of squeezed states by parametric down conversion," *Physical Review Letters*, vol. 57, p. 2520, 20 Nov. 1986, ISSN: 00319007. DOI: 10.1103/PhysRevLett.57.2520.

[28] A. Aspect, P. Grangier, and G. Roger, "Experimental realization of einstein-podolsky-rosen-bohm gedankenexperiment: A new violation of bell's inequalities," *Physical Review Letters*, vol. 49, p. 91, 2 Jul. 1982, ISSN: 00319007. DOI: 10.1103/PhysRevLett.49.91.

[29] D. Bouwmeester, J.-W. Pan, K. Mattle, M. Eibl, H. Weinfurter, and A. Zeilinger, "Experimental quantum teleportation," vol. 390, pp. 575–579, 1997. DOI: https://doi.org/10.1038/37539.

[30] H. S. Zhong *et al.*, "Quantum computational advantage using photons," *Science*, vol. 370, pp. 1460–1463, 6523 Dec. 2020, ISSN: 10959203. DOI: 10.1126/SCIENCE.ABE8770/SUPPL_FILE/ABE8770_ZHONG_SM.PDF.

[31] L. S. Madsen *et al.*, "Quantum computational advantage with a programmable photonic processor," *Nature*, vol. 606, no. 7912, pp. 75–81, Jun. 2022, ISSN: 1476-4687. DOI: 10.1038/s41586-022-04725-x.

[32] N. Hodgson and H. Weber, *Optical Resonators*, 1st ed. Springer, London, 1997, p. 659, ISBN: 978-3-540-76137-2. DOI: https://doi.org/10.1007/978-1-4471-3595-1.

[33] A. E. Siegman, "Laser beams and resonators: The 1960s," *IEEE Journal on Selected Topics in Quantum Electronics*, vol. 6, pp. 1380–1388, 6 Nov. 2000, ISSN: 1077260X. DOI: 10.1109/2944.902192.

[34] A. G. Fox and T. Li, "Resonant modes in a maser interferometer," *Bell System Technical Journal*, vol. 40, pp. 453–488, 2 1961, ISSN: 15387305. DOI: 10.1002/J.1538-7305.1961.TB01625.X.

[35] B. P. Abbott *et al.*, "Observation of gravitational waves from a binary black hole merger," *Physical Review Letters*, vol. 116, p. 061 102, 6 Feb. 2016, ISSN: 10797114. DOI: 10.1103/PHYSREVLETT.116.061102/FIGURES/4/MEDIUM.

[36] O. Alibart *et al.*, "Nonlinear and quantum optics with whispering gallery resonators," *J. Opt.*, vol. 18, 2016. DOI: 10.1088/2040-8978/18/12/123002.

[37] N. Ismail *et al.*, "Fabry-pérot resonator: Spectral line shapes, generic and related airy distributions, linewidths, finesses, and performance at low or frequency-dependent reflectivity," *Optics Express, Vol. 24, Issue 15, pp. 16366-16389*, vol. 24, pp. 16 366–16 389, 15 Jul. 2016, ISSN: 1094-4087. DOI: 10.1364/OE.24.016366.

[38] D. Hunger, T. Steinmetz, Y. Colombe, C. Deutsch, T. W. Hänsch, and J. Reichel, "A fiber fabry–perot cavity with high finesse," *New Journal of Physics*, vol. 12, p. 065 038, 6 Jun. 2010, ISSN: 1367-2630. DOI: 10.1088/1367-2630/12/6/065038.

[39] A. Yariv, "Universal relations for coupling of optical power between microresonators and dielectric waveguides," *Electronics Letters*, vol. 36, pp. 321–322, 4 Feb. 2000, ISSN: 00135194. DOI: 10.1049/EL:20000340.

[40] M. L. Gorodetsky, A. A. Savchenkov, and V. S. Ilchenko, "Ultimate q of optical microsphere resonators," *Opt. Lett.*, vol. 21, no. 7, pp. 453–455, Apr. 1996. DOI: 10.1364/OL.21.000453.

[41] D. W. Vernooy, V. S. Ilchenko, H. Mabuchi, E. W. Streed, and H. J. Kimble, "High-q measurements of fused-silica microspheres in the near infrared," *Opt. Lett.*, vol. 23, no. 4, pp. 247–249, Feb. 1998. DOI: 10.1364/OL.23.000247.

[42] C.-H. Chen, P.-T. Chen, T.-J. Wang, and W.-C. Hsiao, "High-Q $LiNbO_3$ Microtoroid Resonators," *Journal of Lightwave Technology, Vol. 34, Issue 14, pp. 3306-3311*, vol. 34, pp. 3306–3311, 14 Jul. 2016. DOI: 10.1109/JLT.2016.2568220.

[43] D. J. Moss, R. Morandotti, A. L. Gaeta, and M. Lipson, "New CMOS-compatible platforms based on silicon nitride and Hydex for nonlinear optics," *Nature Photonics*, vol. 7, pp. 597–607, 8 Aug. 2013, ISSN: 17494885. DOI: 10.1038/nphoton.2013.183.

[44] D. K. Armani, T. J. Kippenberg, S. M. Spillane, and K. J. Vahala, "Ultra-high-q toroid microcavity on a chip," *Nature*, vol. 421, pp. 925–928, 6926 Feb. 2003, ISSN: 00280836. DOI: 10.1038/nature01371.

[45] P. Del'Haye, S. A. Diddams, and S. B. Papp, "Laser-machined ultra-high-q microrod resonators for nonlinear optics," *Applied Physics Letters*, vol. 102, p. 221 119, 22 Jun. 2013, ISSN: 00036951. DOI: 10.1063/1.4809781.

[46] Y. L. Pan and R. K. Chang, "Highly efficient prism coupling to whispering gallery modes of a square micro-cavity," *Applied Physics Letters*, vol. 82, pp. 487–489, 4 Jan. 2003, ISSN: 00036951. DOI: 10.1063/1.1540242.

[47] Z. Wang *et al.*, "On-chip single-mode high-q terahertz whispering gallery mode resonator," *Optics Letters*, vol. 44, p. 2835, 11 Jun. 2019, ISSN: 0146-9592. DOI: 10.1364/ol.44.002835.

[48] J. C. Knight, G. Cheung, F. Jacques, and T. A. Birks, "Phase-matched excitation of whispering-gallery-mode resonances by a fiber taper," *Optics Letters*, vol. 22, p. 1129, 15 Aug. 1997, ISSN: 0146-9592. DOI: 10.1364/ol.22.001129.

[49] L. Hill, G.-L. Oppo, M. T. M. Woodley, and P. Del'Haye, "Effects of self- and cross-phase modulation on the spontaneous symmetry breaking of light in ring resonators," *Phys. Rev. A*, vol. 101, p. 013 823, 2020. DOI: 10.1103/PhysRevA.101.013823.

[50] S. E. Harris, M. K. Oshman, and R. L. Byer, "Observation of tunable optical parametric fluorescence," *Physical Review Letters*, vol. 18, p. 732, 18 May 1967, ISSN: 00319007. DOI: 10.1103/PhysRevLett.18.732.

[51] P. G. Kwiat, K. Mattle, H. Weinfurter, A. Zeilinger, A. V. Sergienko, and Y. Shih, "New high-intensity source of polarization-entangled photon pairs," *Physical Review Letters*, vol. 75, p. 4337, 24 Dec. 1995, ISSN: 00319007. DOI: 10.1103/PhysRevLett.75.4337.

[52] J. B. Geddes, J. V. Moloney, E. M. Wright, and W. J. Firth, "Polarisation patterns in a nonlinear cavity," *Optics Communications*, vol. 111, pp. 623–631, 5-6 Oct. 1994, ISSN: 00304018. DOI: 10.1016/0030-4018(94)90540-1.

[53] Y. K. Chembo, "Quantum dynamics of kerr optical frequency combs below and above threshold: Spontaneous four-wave mixing, entanglement, and squeezed states of light," *Physical Review A*, vol. 93, p. 033 820, 3 Mar. 2016, ISSN: 24699934. DOI: 10.1103/PhysRevA.93.033820.

[54] ——, "Quantum dynamics of kerr optical frequency combs below and above threshold: Spontaneous four-wave mixing, entanglement, and squeezed states of light," *Physical Review A*, vol. 93, p. 33 820, 2016. DOI: 10.1103/PhysRevA.93.033820.

[55] S. A. Castelletto and R. E. Scholten, "Heralded single photon sources: A route towards quantum communication technology and photon standards," *The European Physical Journal - Applied Physics*, vol. 41, pp. 181–194, 3 Mar. 2008, ISSN: 1286-0042. DOI: 10.1051/EPJAP:2008029.

[56] S. Fujii and T. Tanabe, "Dispersion engineering and measurement of whispering gallery mode microresonator for kerr frequency comb generation," *Nanophotonics*, vol. 9, pp. 1087–1104, 5 May 2020, ISSN: 21928614. DOI: 10.1515/nanoph-2019-0497.

[57] P. D. 'Haye, "Optical frequency comb generation in monolithic microresonators," 2011.

[58] T. Herr *et al.*, "Temporal solitons in optical microresonators," *Nature Photonics*, vol. 8, pp. 145–152, 2 Feb. 2014, ISSN: 17494885. DOI: 10.1038/nphoton.2013.343.

[59] L. A. Lugiato and R. Lefever, "Spatial dissipative structures in passive optical systems," *Physical Review Letters*, vol. 58, pp. 2209–2211, 21 May 1987, ISSN: 00319007. DOI: 10.1103/PhysRevLett.58.2209.

[60] Y. K. Chembo and C. R. Menyuk, "Spatiotemporal lugiato-lefever formalism for kerr-comb generation in whispering-gallery-mode resonators," *Physical Review A*, vol. 87, p. 53 852, 2013. DOI: 10.1103/PhysRevA.87.053852.

[61] R. Suzuki, S. Fujii, A. Hori, and T. Tanabe, "Theoretical study on dual-comb generation and soliton trapping in a single microresonator with orthogonally polarized dual pumping," *IEEE Photonics Journal*, vol. 11, no. 1, pp. 1–11, 2019. DOI: 10.1109/JPHOT.2018.2888637.

[62] D. C. Cole, A. Gatti, S. B. Papp, F. Prati, and L. Lugiato, "Theory of kerr frequency combs in fabry-perot resonators," *Phys. Rev. A*, vol. 98, p. 013 831, 1 Jul. 2018. DOI: 10.1103/PhysRevA.98.013831.

[63] E. Obrzud, S. Lecomte, and T. Herr, "Temporal solitons in microresonators driven by optical pulses," *Nature Photonics 2017 11:9*, vol. 11, pp. 600–607, 9 Aug. 2017, ISSN: 1749-4893. DOI: 10.1038/nphoton.2017.140.

[64] T. Hansson, D. Modotto, and S. Wabnitz, "On the numerical simulation of kerr frequency combs using coupled mode equations," *Optics Communications*, vol. 312, pp. 134–136, 2014, ISSN: 00304018. DOI: 10.1016/j.optcom.2013.09.017.

[65] R. W. P. Drever *et al.*, "Laser phase and frequency stabilization using an optical resonator," *Appl. Phys. B*, vol. 31, pp. 97–105, DOI: https://doi.org/10.1007/BF00702605.

[66] J. I. Thorpe *et al.*, "Laser frequency stabilization and control through offset sideband locking to optical cavities references and links," 2008. DOI: 10.1364/OE.16.015980.

[67] T. Carmon, L. Yang, and K. J. Vahala., "Dynamical thermal behavior and thermal self-stability of microcavities," vol. 12, Optical Society of America, Oct. 2005, pp. 4742–4750, ISBN: 1557527709. DOI: 10.1364/opex.12.004742.

[68] N. Moroney *et al.*, "A kerr polarization controller," *Nature Communications 2022 13:1*, vol. 13, pp. 1–8, 1 Jan. 2022, ISSN: 2041-1723. DOI: 10.1038/s41467-021-27933-x.

[69] D. Sinha and G. A. J. Amaratunga, *Spontaneous symmetry breaking*, 2016. DOI: 10.1088/978-1-6817-4357-8ch3.

[70] F. Strocchi, "Spontaneous symmetry breaking in local gauge quantum field theory; the higgs mechanism," *Comm. Math. Phys.*, vol. 56, pp. 57–78, 1 Feb. 1977, ISSN: 00103616. DOI: 10.1007/BF01611117.

[71] A. J. Beekman, L. Rademaker, and J. van Wezel, "An introduction to spontaneous symmetry breaking," *SciPost Physics Lecture Notes*, Sep. 2019, ISSN: 2590-1990. DOI: 10.21468/scipostphyslectnotes.11.

[72] Y. Xu and S. Coen, "Experimental observation of the spontaneous breaking of the time-reversal symmetry in a synchronously pumped passive kerr resonator," *Optics Letters*, vol. 39, p. 3492, 12 Jun. 2014, ISSN: 0146-9592. DOI: 10.1364/ol.39.003492.

[73] F. Copie, M. T. Woodley, L. D. Bino, J. M. Silver, S. Zhang, and P. Del'Haye, "Interplay of polarization and time-reversal symmetry breaking in synchronously pumped ring resonators," *Physical Review Letters*, vol. 122, p. 013 905, 1 Jan. 2019, ISSN: 10797114. DOI: 10.1103/PhysRevLett.122.013905.

[74] Q. F. Yang, X. Yi, K. Y. Yang, and K. Vahala, "Counter-propagating solitons in microresonators," *Nature Photonics*, vol. 11, pp. 560–564, 9 Sep. 2017, ISSN: 17494893. DOI: 10.1038/nphoton.2017.117.

[75] C. Bao *et al.*, "Orthogonally polarized frequency comb generation from a kerr comb via cross-phase modulation," *Optics Letters*, vol. 44, p. 1472, 6 Mar. 2019, ISSN: 0146-9592. DOI: 10.1364/ol.44.001472.

[76] E. Lucas *et al.*, "Spatial multiplexing of soliton microcombs," *Nature Photonics*, vol. 12, pp. 699–705, 11 2018. DOI: 10.1038/s41566-018-0256-7.

[77] C. Joshi *et al.*, "Counter-rotating cavity solitons in a silicon nitride microresonator," *Opt. Lett.*, vol. 43, pp. 547–550, 3 2018. DOI: 10.1364/OL.43.000547.

[78] S. Zhang, J. M. Silver, T. Bi, and P. Del'Haye, "Spectral extension and synchronization of microcombs in a single microresonator," *Nature Communications*, vol. 11, p. 6384, 1 Dec. 2020, ISSN: 20411723. DOI: 10.1038/s41467-020-19804-8.

[79] L. D. Bino, J. M. Silver, S. L. Stebbings, and P. Del'Haye, "Symmetry breaking of counter-propagating light in a nonlinear resonator," *Sci. Rep.*, vol. 7, p. 43 412, 1 Feb. 2017, ISSN: 20452322. DOI: 10.1038/srep43142.

[80] Q. T. Cao *et al.*, "Experimental demonstration of spontaneous chirality in a nonlinear microresonator," *Physical Review Letters*, vol. 118, p. 033 901, 3 Jan. 2017, ISSN: 10797114. DOI: 10.1103/PhysRevLett.118.033901.

[81] M. T. Woodley *et al.*, "Universal symmetry-breaking dynamics for the kerr interaction of counterpropagating light in dielectric ring resonators," *Physical Review A*, vol. 98, p. 053 863, 5 Nov. 2018, ISSN: 24699934. DOI: 10.1103/PhysRevA.98.053863.

[82] B. Garbin, J. Fatome, G. L. Oppo, M. Erkintalo, S. G. Murdoch, and S. Coen, "Dissipative polarization domain walls in a passive coherently driven kerr resonator," *Physical Review Letters*, vol. 126, p. 023 904, 2 Jan. 2021, ISSN: 10797114. DOI: 10.1103/PhysRevLett.126.023904.

[83] J. Fatome *et al.*, "Polarization modulation instability in a nonlinear fiber kerr resonator," *Opt. Lett.*, vol. 45, pp. 5069–5072, 18 Oct. 2020, ISSN: 23318422. DOI: 10.1364/ol.400474.

[84] G. Xu *et al.*, "Spontaneous symmetry breaking of dissipative optical solitons in a two-component kerr resonator," *Nature Communications*, vol. 12, p. 4023, 1 Dec. 2021, ISSN: 20411723. DOI: 10.1038/s41467-021-24251-0.

[85] L. Hill *et al.*, "Breathing dynamics of symmetry-broken polarized temporal cavity solitons in kerr ring resonators," The Optical Society, Oct. 2020, NpTu1D.3. DOI: 10.1364/np.2020.nptu1d.3.

[86] B. Garbin, J. Fatome, G.-L. Oppo, M. Erkintalo, S. G. Murdoch, and S. Coen, "Asymmetric balance in symmetry breaking," *Phys. Rev. Research*, vol. 2, pp. 023 244–023 256, 2 2020. DOI: 10.1103/PhysRevResearch.2.023244.

[87] B. Sun *et al.*, "On-chip beam rotators, adiabatic mode converters, and waveplates through low-loss waveguides with variable cross-sections," *Light: Science & Applications*, vol. 11, no. 1, p. 214, Jul. 2022, ISSN: 2047-7538. DOI: 10.1038/s41377-022-00907-4.

[88] Z.-S. Hou *et al.*, "On-chip polarization rotators," *Advanced Optical Materials*, vol. 7, no. 10, p. 1 900 129, 2019. DOI: https://doi.org/10.1002/adom.201900129. eprint: https://onlinelibrary.wiley.com/doi/pdf/10.1002/adom.201900129.

[89] Y. Zhang *et al.*, "Complete polarization controller based on magneto-optic crystals and fixed quarter wave plates," *Optics Express*, vol. 14, p. 3484, 8 Apr. 2006, ISSN: 1094-4087. DOI: 10.1364/oe.14.003484.

[90] D. Floess *et al.*, "Tunable and switchable polarization rotation with nonreciprocal plasmonic thin films at designated wavelengths," *Light: Science & Applications*, vol. 4, no. 5, e284–e284, May 2015, ISSN: 2047-7538. DOI: 10.1038/lsa.2015.57.

[91] J. Shi, X. Chen, Y. Xia, and Y. Chen, "Polarization control by use of the electro-optic effect in periodically poled lithium niobate," *Applied Optics*, vol. 42, p. 5722, 28 Oct. 2003, ISSN: 0003-6935. DOI: 10.1364/ao.42.005722.

[92] T. Li, Q. Chen, and X. Zhang, "Electrically controlled polarization rotator using nematic liquid crystal," *Opt. Express*, vol. 26, no. 24, pp. 32 317–32 323, Nov. 2018. DOI: 10.1364/OE.26.032317.

[93] P. Velha *et al.*, "Wide-band polarization controller for si photonic integrated circuits," *Optics Letters*, vol. 41, p. 5656, 24 Dec. 2016, ISSN: 0146-9592. DOI: 10.1364/ol.41.005656.

[94] J. D. Sarmiento-Merenguel *et al.*, "Demonstration of integrated polarization control with a 40 db range in extinction ratio," *Optica*, vol. 2, pp. 1019–1023, 12 2015. DOI: 10.1364/OPTICA.2.001019.

[95] Q. Xu, L. Chen, M. G. Wood, P. Sun, and R. M. Reano, "Electrically tunable optical polarization rotation on a silicon chip using berry's phase," *Nature Communications*, vol. 5, p. 5337, 1 Nov. 2014, ISSN: 20411723. DOI: 10.1038/ncomms6337.

[96] R. Roth, M. M. Koch, A. D. Rata, and K. Dörr, "Mechanical nanoscale polarization control in ferroelectric pvdf-trfe films," *Advanced Electronic Materials*, vol. 8, p. 2 101 416, 6 Jun. 2022, ISSN: 2199-160X. DOI: 10.1002/AELM.202101416.

[97] M. T. Woodley, L. Hill, L. D. Bino, G. L. Oppo, and P. Del'Haye, "Self-switching kerr oscillations of counterpropagating light in microresonators," *Physical Review Letters*, vol. 126, p. 043 901, 4 Jan. 2021, ISSN: 10797114. DOI: 10.1103/PhysRevLett.126.043901.

[98] N. Moroney *et al.*, "Logic gates based on interaction of counterpropagating light in microresonators," *Journal of Lightwave Technology*, vol. 38, pp. 1414–1419, 6 Mar. 2020, ISSN: 15582213. DOI: 10.1109/JLT.2020.2975119.

[99] L. D. Bino, N. Moroney, and P. Del'Haye, "Optical memories and switching dynamics of counterpropagating light states in microresonators," *Optics Express*, vol. 29, p. 2193, 2 2021. DOI: 10.1364/OE.417951.

[100] Q. Cheng, M. Bahadori, M. Glick, S. Rumley, and K. Bergman, "Recent advances in optical technologies for data centers: A review," *Optica*, vol. 5, p. 1354, 11 Nov. 2018, ISSN: 2334-2536. DOI: 10.1364/optica.5.001354.

[101] V. Sasikala and K. Chitra, "All optical switching and associated technologies: A review," *Journal of Optics (India)*, vol. 47, pp. 307–317, 3 Sep. 2018, ISSN: 09746900. DOI: 10.1007/s12596-018-0452-3.

[102] J. Wang and Y. Long, *On-chip silicon photonic signaling and processing: A review*, Oct. 2018. DOI: 10.1016/j.scib.2018.05.038.

[103] D. Marcuse, "Coupled mode theory of optical resonant cavities," *IEEE Journal of Quantum Electronics*, vol. 21, pp. 1819–1826, 11 1985, ISSN: 15581713. DOI: 10.1109/JQE.1985.1072590.

[104] G. P. Agrawal, *Nonlinear fiber optics*. 2019, pp. 1–728, ISBN: 9780128170427. DOI: 10.1016/C2018-0-01168-8.

[105] N. Moroney *et al.*, "Logic Gates Based on Interaction of Counterpropagating Light in Microresonators," *Journal of Lightwave Technology*, vol. 38, no. 6, pp. 1414–1419, Mar. 2020. DOI: 10.1109/JLT.2020.2975119.

[106] J. Silver, L. D. Bino, and P. D. Haye, "A nonlinear enhanced microresonator gyroscope," vol. 2017-Janua, Institute of Electrical and Electronics Engineers Inc., Oct. 2017, pp. 1–2, ISBN: 9781943580279. DOI: 10.1109/cleoe-eqec.2017.8086527.

[107] W. M. Macek and D. T. M. Davis, "Rotation rate sensing with traveling-wave ring lasers," *Applied Physics Letters*, vol. 2, no. 3, pp. 67–68, 1963. DOI: 10.1063/1.1753778. eprint: https://doi.org/10.1063/1.1753778.

[108] A. D. V. Di Virgilio, N. Beverini, G. Carelli, D. Ciampini, F. Fuso, and E. Maccioni, "Analysis of ring laser gyroscopes including laser dynamics," *The European Physical Journal C*, vol. 79, no. 7, p. 573, Jul. 2019, ISSN: 1434-6052. DOI: 10.1140/epjc/s10052-019-7089-5.

[109] L. L. Bonilla, M. Alvaro, and M. Carretero, "Chaos-based true random number generators," *Journal of Mathematics in Industry*, vol. 7, no. 1, p. 1, Jun. 2016, ISSN: 2190-5983. DOI: 10.1186/s13362-016-0026-4.

[110] R. G. Gallager, *Principles of digital communication*. Cambridge University Press Cambridge, UK, 2008, vol. 1.

[111] K. Binder, D. Heermann, L. Roelofs, A. J. Mallinckrodt, and S. McKay, "Monte carlo simulation in statistical physics," *Computers in Physics*, vol. 7, no. 2, pp. 156–157, 1993.

[112] S. Asmussen and P. W. Glynn, *Stochastic simulation: algorithms and analysis*. Springer, 2007, vol. 57.

[113] D. R. Stinson, *Cryptography: theory and practice*. Chapman and Hall/CRC, 2005.

[114] E. Agrell *et al.*, "Roadmap of optical communications," *J. Opt.*, vol. 18, no. 063002, p. 40, 2016. DOI: 10.1088/2040-8978/18/6/063002.

[115] W. Liu *et al.*, "A fully reconfigurable photonic integrated signal processor," *Nat. Photon.*, vol. 10, pp. 190–195, 2016. DOI: 10.1038/NPHOTON.2015.281.

[116] A. Jajszczyk, "Optical networks - the electro-optic reality," *OSN*, vol. 1, no. 1, pp. 3–18, Jan. 2005, ISSN: 15734277. DOI: 10.1016/j.osn.2004.11.002.

[117] J. Touch, A. H. Badawy, and V. J. Sorger, "Optical computing," *Nanophotonics*, vol. 6, pp. 503–505, 3 May 2017, ISSN: 21928614. DOI: 10.1515/NANOPH-2016-0185/MACHINEREADABLECITATION/RIS.

[118] J. Touch, Y. Cao, M. Ziyadi, A. Almaiman, A. Mohajerin-Ariaei, and A. E. Willner, "Digital optical processing of optical communications: Towards an optical turing machine," *Nanophotonics*, vol. 6, pp. 507–530, 3 May 2017, ISSN: 21928614. DOI: 10.1515/NANOPH-2016-0145/ASSET/GRAPHIC/J_NANOPH-2016-0145_FIG_033.JPG.

[119] T. F. D. Lima, B. J. Shastri, A. N. Tait, M. A. Nahmias, and P. R. Prucnal, "Progress in neuromorphic photonics," *Nanophotonics*, vol. 6, pp. 577–599, 3 May 2017, ISSN: 21928614. DOI: 10.1515/NANOPH-2016-0139/ASSET/GRAPHIC/J_NANOPH-2016-0139_FIG_006.JPG.

[120] G. V. D. Sande, D. Brunner, and M. C. Soriano, "Advances in photonic reservoir computing," *Nanophotonics*, vol. 6, pp. 561–576, 3 May 2017, ISSN: 21928614. DOI: 10.1515/NANOPH-2016-0132/ASSET/GRAPHIC/J_NANOPH-2016-0132_FIG_010.JPG.

[121] Y. Shen *et al.*, "Deep learning with coherent nanophotonic circuits," *Nature Photonics*, vol. 11, no. 7, pp. 441–446, Jul. 2017, ISSN: 1749-4893. DOI: 10.1038/nphoton.2017.93.

[122] H. Krovi, "Models of optical quantum computing," *Nanophotonics*, vol. 6, pp. 531–541, 3 May 2017, ISSN: 21928614. DOI: 10.1515/NANOPH-2016-0136/ASSET/GRAPHIC/J_NANOPH-2016-0136_FIG_006.JPG.

[123] Q. Cheng, M. Bahadori, M. Glick, S. Rumley, and K. Bergman, "Recent advances in optical technologies for data centers: A review," *Optica*, vol. 5, no. 11, pp. 1354–1370, Nov. 2018. DOI: 10.1364/OPTICA.5.001354.

[124] C. A. Thraskias *et al.*, "Survey of photonic and plasmonic interconnect technologies for intra-datacenter and high-performance computing communications," *IEEE Communications Surveys & Tutorials*, vol. 20, no. 4, pp. 2758–2783, 2018. DOI: 10.1109/COMST.2018.2839672.

[125] S. Misik, A. Cela, and Z. Bradac, "Distributed systems - a brief review of theory and practice," *IFAC-PapersOnLine*, vol. 49, no. 25, pp. 318–323, 2016, 14th IFAC Conference on Programmable Devices and Embedded Systems PDES 2016, ISSN: 2405-8963. DOI: https://doi.org/10.1016/j.ifacol.2016.12.057.

[126] M. A. Taubenblatt, "Optical Interconnects for High-Performance Computing," *Journal of Lightwave Technology, Vol. 30, Issue 4, pp. 448-457*, vol. 30, no. 4, pp. 448–457, Feb. 2012. DOI: 10.1109/PHO.2011.6110726.

[127] C. Sun *et al.*, "Single-chip microprocessor that communicates directly using light," *Nature*, vol. 528, no. 7583, pp. 534–538, Dec. 2015, ISSN: 1476-4687. DOI: 10.1038/nature16454.

[128] A. F. Benner, M. Ignatowski, J. A. Kash, D. M. Kuchta, and M. B. Ritter, "Exploitation of optical interconnects in future server architectures," *IBM Journal of Research and Development*, vol. 49, no. 4.5, pp. 755–775, 2005. DOI: 10.1147/rd.494.0755.

[129] S. Rumley *et al.*, "Optical interconnects for extreme scale computing systems," *Parallel Computing*, vol. 64, pp. 65–80, 2017, High-End Computing for Next-Generation Scientific Discovery, ISSN: 0167-8191. DOI: https://doi.org/10.1016/j.parco.2017.02.001.

[130] J. M. Johansson, "On the impact of network latency on distributed systems design," *Information Technology and Management*, vol. 1, no. 3, pp. 183–194, Jan. 2000, ISSN: 1573-7667. DOI: 10.1023/A:1019121024410.

[131] G. Zervas, H. Yuan, A. Saljoghei, Q. Chen, and V. Mishra, "Optically disaggregated data centers with minimal remote memory latency: Technologies, architectures, and resource allocation," *J. Opt. Commun. Netw.*, vol. 10, no. 2, A270–A285, Feb. 2018. DOI: 10.1364/JOCN.10.00A270.

[132] G. Lin, C. Aurélien, and Y. K. Chembo, "Nonlinear photonics with high-Q resonators," *Adv. Opt. Photonics*, vol. 9, no. 4, pp. 828–890, 2017. DOI: 10.1364/AOP.9.000828.

[133] L. Gorodetsky, "Quality-factor and Nonlinear Properties of Optical Whispering-Gallery Modes," *Phys. Lett. A*, vol. 137, no. 7, pp. 393–397, 1989. DOI: https://doi.org/10.1016/0375-9601(89)90912-2.

[134] S. Zhang *et al.*, "Sub-milliwatt-level microresonator solitons with extended access range using an auxiliary laser," *Optica*, vol. 6, no. 2, pp. 206–212, 2019. DOI: 10.1364/OPTICA.6.000206.

[135] Z. I. W. Ang, S. H. Y. Uan, G. A. D. Ong, R. U. W. Ang, L. I. A. O. C. Hen, and X. W. U. Iaojun, "On-chip single-mode high-Q terahertz whispering gallery mode resonator," *Opt. Lett.*, vol. 44, no. 11, pp. 3–6, 2019. DOI: 10.1364/OL.44.002835.

[136] T. Hett, S. Krämmer, U. Hilleringmann, H. Kalt, and A. Zrenner, "High-Q whispering gallery microdisk resonators based on silicon oxynitride," *J. Lumin.*, vol. 191, pp. 131–134, Nov. 2017, ISSN: 00222313. DOI: 10.1016/j.jlumin.2016.11.016.

[137] D. J. Moss, R. Morandotti, A. L. Gaeta, and M. Lipson, "New CMOS-compatible platforms based on silicon nitride and Hydex for nonlinear optics," *Nat. Photon.*, vol. 7, pp. 597–607, 2013. DOI: 10.1038/NPHOTON.2013.183.

[138] Q. Xu and M. Lipson, "All-optical logic based on silicon micro-ring resonators," *Opt. Express*, vol. 15, no. 3, p. 924, 2007, ISSN: 1094-4087. DOI: 10.1364/OE.15.000924.

[139] D. Gostimirovic and W. N. Ye, "Ultracompact CMOS-compatible optical logic using carrier depletion in microdisk resonators," *Sci. Rep.*, vol. 7, no. 12603, pp. 1–10, 2017. DOI: 10.1038/s41598-017-12680-1.

[140] P. Sethi and S. Roy, "All-optical ultrafast XOR/XNOR logic gates, binary counter, and double-bit comparator with silicon microring resonators," *Appl. Opt.*, vol. 53, no. 28, p. 6527, 2014, ISSN: 0003-6935. DOI: 10.1364/ao.53.006527.

[141] A. Godbole, P. P. Dali, V. Janyani, T. Tanabe, and G. Singh, "All Optical Scalable Logic Gates Using Si_3N_4 Microring Resonators," *IEEE J. Sel. Top. Quantum Electron.*, vol. 22, no. 6, pp. 326–333, 2016, ISSN: 1077260X. DOI: 10.1109/JSTQE.2016.2593278.

[142] M. Xiong *et al.*, "All-optical 10 Gb/s AND logic gate in a silicon microring resonator," *Opt. Express*, vol. 21, no. 22, 2013. DOI: 10.1364/OE.21.025772.

[143] S. Mikroulis, H. Simos, E. Roditi, and D. Syvridis, "Ultrafast All-Optical AND Logic Operation Based on Four-Wave Mixing in a Passive InGaAsP-InP Microring Resonator," *IEEE Photonic Tech. L.*, vol. 17, no. 9, pp. 1878–1880, 2005. DOI: 10.1109/LPT.2005.853260.

[144] T. A. Ibrahim, R. Grover, L.-C. Kuo, S. Kanakaraju, L. C. Calhoun, and P.-T. Ho, "All-Optical AND/NAND Logic Gates Using Semiconductor Microresonators," *IEEE Photonic Tech. L.*, vol. 15, no. 10, 2003. DOI: 10.1109/LPT.2003.818049.

[145] A. Fushimi and T. Tanabe, "All-optical logic gate operating with single wavelength," *Opt. Express*, vol. 22, no. 4, p. 4466, Feb. 2014, ISSN: 1094-4087. DOI: 10.1364/OE.22.004466.

[146] P. P. Dali, A. Godbole, S. Sahu, G. Singh, and T. Tanabe, "Microring Resonator Based All Optical NAND and NOT Gate with Higher Output Power," in *ACP*, Washington, D.C.: OSA, Nov. 2015, ISBN: 978-1-943580-06-4. DOI: 10.1364/ACPC.2015.ASu2A.28.

[147] L. Zhang *et al.*, "Demonstration of directed XOR / XNOR logic gates using two cascaded microring resonators," *Opt. Lett.*, vol. 35, no. 10, pp. 1620–1622, 2010. DOI: 10.1364/OL.35.001620.

[148] Q. Xu *et al.*, "Reconfigurable optical directed-logic circuits using microresonator-based optical switches," *Optics Express*, vol. 15, no. 1, pp. 10 941–10 946, 2007.

[149] C. Qiu, W. Gao, R. Soref, J. T. Robinson, and Q. Xu, "Reconfigurable electro-optical directed-logic circuit using carrier-depletion micro-ring resonators," *Opt. Lett.*, vol. 39, no. 24, pp. 6767–6770, 2014. DOI: 10.1364/OL.39.006767.

[150] Y. Tian *et al.*, "Experimental demonstration of an optical Feynman gate for reversible logic operation using silicon micro-ring resonators," *Nanophotonics*, vol. 7, no. 1, pp. 333–337, 2018. DOI: 10.1515/nanoph-2017-0071.

[151] Y. Tian, L. Zhang, and L. Yang, "Directed XOR/XNOR Logic Gates Using U-to-U Waveguides and Two Microring Resonators," *IEEE Photonic Tech. L.*, vol. 25, no. 1, pp. 18–21, 2013. DOI: 10.1109/LPT.2012.2227307.

[152] T. A. Ibrahim, K. Amarnath, L. C. Kuo, R. Grover, V. Van, and P.-T. Ho, "Photonic logic NOR gate based on two symmetric microring resonators," *Opt. Lett.*, vol. 29, no. 23, p. 2779, 2004, ISSN: 0146-9592. DOI: 10.1364/OL.29.002779.

[153] T. M. Rambo, "Low-Loss, All-Optical, Quantum Switching For Interferometric Processing of Weak Signals," Ph.D. dissertation, Northwestern University, Jan. 2016.

[154] J. E. Davis and D. Ö. Güney, "Effect of loss on linear optical quantum logic gates," *J. Opt. Soc. Am. B*, vol. 38, no. 9, pp. C153–C159, Sep. 2021. DOI: 10.1364/JOSAB.430603.

[155] R. Landauer, "Irreversibility and heat generation in the computing process," *IBM Journal of Research and Development*, vol. 5, no. 3, pp. 183–191, 1961. DOI: 10.1147/rd.53.0183.

[156] A. Svela *et al.*, "Coherent suppression of backscattering in optical microresonators," *Light: Science & Applications 2020 9:1*, vol. 9, no. 1, pp. 1–8, Dec. 2020, ISSN: 2047-7538. DOI: 10.1038/s41377-020-00440-2. arXiv: 2002.12379.

[157] Y. Liu *et al.*, "A photonic integrated circuit-based erbium-doped amplifier," *Science*, vol. 376, no. 6599, pp. 1309–1313, 2022. DOI: 10.1126/science.abo2631. eprint: https://www.science.org/doi/pdf/10.1126/science.abo2631.

[158] T. Matsumoto *et al.*, "Hybrid-integration of SOA on silicon photonics platform based on flip-chip bonding," *Journal of Lightwave Technology*, vol. 37, no. 2, pp. 307–313, 2019. DOI: 10.1109/JLT.2018.2870128.

[159] P. Kok, W. J. Munro, K. Nemoto, T. C. Ralph, J. P. Dowling, and G. J. Milburn, "Linear optical quantum computing with photonic qubits," *Reviews of Modern Physics*, vol. 79, pp. 135–174, 1 Jan. 2007, ISSN: 00346861. DOI: 10.1103/REVMODPHYS.79.135/FIGURES/37/MEDIUM.

[160] F. Shahandeh, A. P. Lund, T. C. Ralph, and M. R. Vanner, "Arbitrary multiqubit generation," *New Journal of Physics*, vol. 18, p. 103 020, 10 Oct. 2016, ISSN: 1367-2630. DOI: 10.1088/1367-2630/18/10/103020.

[161] T. Tyc and N. Korolkova, "Highly non-gaussian states created via cross-kerr nonlinearity," *New Journal of Physics*, vol. 10, no. 2, p. 023 041, Feb. 2008. DOI: 10.1088/1367-2630/10/2/023041.

[162] C. Navarrete-Benlloch, T. Weiss, S. Walter, and G. J. de Valcárcel, "General linearized theory of quantum fluctuations around arbitrary limit cycles," *Phys. Rev. Lett.*, vol. 119, p. 133 601, 13 Sep. 2017. DOI: 10.1103/PhysRevLett.119.133601.

[163] P. Drummond, K. McNeil, and D. Walls, "Non-equilibrium transitions in sub/second harmonic generation," *Optica Acta: International Journal of Optics*, vol. 28, no. 2, pp. 211–225, 1981. DOI: 10.1080/713820531. eprint: https://doi.org/10.1080/713820531.

[164] C. T. Lee, "Nonclassical photon statistics of two-mode squeezed states," *Phys. Rev. A*, vol. 42, pp. 1608–1616, 3 Aug. 1990. DOI: 10.1103/PhysRevA.42.1608.

[165] S. L. Braunstein, "Squeezing as an irreducible resource," *Phys. Rev. A*, vol. 71, p. 055 801, 5 May 2005. DOI: 10.1103/PhysRevA.71.055801.

[166] G. Patera, N. Treps, C. Fabre, and G. J. de Valcárcel, "Quantum theory of synchronously pumped type i optical parametricoscillators: Characterization of the squeezed supermodes," *The European Physical Journal D*, vol. 56, no. 1, p. 123, Dec. 2009, ISSN: 1434-6079. DOI: 10.1140/epjd/e2009-00299-9.

[167] G. J. de Valcárcel, G. Patera, N. Treps, and C. Fabre, "Multimode squeezing of frequency combs," *Phys. Rev. A*, vol. 74, p. 061 801, 6 Dec. 2006. DOI: 10.1103/PhysRevA.74.061801.

[168] E. C. Cheung and J. M. Liu, "Theory of a synchronously pumped optical parametric oscillator in steady-state operation," *J. Opt. Soc. Am. B*, vol. 7, no. 8, pp. 1385–1401, Aug. 1990. DOI: 10.1364/JOSAB.7.001385.

[169] D. C. Edelstein, E. S. Wachman, and C. L. Tang, "Broadly tunable high repetition rate femtosecond optical parametric oscillator," *Applied Physics Letters*, vol. 54, no. 18, pp. 1728–1730, 1989. DOI: 10.1063/1.101272. eprint: https://doi.org/10.1063/1.101272.

[170] O. Pinel *et al.*, "Generation and characterization of multimode quantum frequency combs," *Physical Review Letters*, vol. 108, p. 083 601, 8 Feb. 2012, ISSN: 00319007. DOI: 10.1103/PHYSREVLETT.108.083601/FIGURES/4/MEDIUM.

[171] M. Chen, N. C. Menicucci, and O. Pfister, "Experimental realization of multipartite entanglement of 60 modes of a quantum optical frequency comb," *Phys. Rev. Lett.*, vol. 112, p. 120 505, 12 Mar. 2014. DOI: 10.1103/PhysRevLett.112.120505.

[172] N. C. Menicucci, P. van Loock, M. Gu, C. Weedbrook, T. C. Ralph, and M. A. Nielsen, "Universal quantum computation with continuous-variable cluster states," *Phys. Rev. Lett.*, vol. 97, p. 110 501, 11 Sep. 2006. DOI: 10.1103/PhysRevLett.97.110501.

[173] C. Weedbrook *et al.*, "Gaussian quantum information," *Rev. Mod. Phys.*, vol. 84, pp. 621–669, 2 May 2012. DOI: 10.1103/RevModPhys.84.621.

[174] J. U. Fürst *et al.*, "Quantum light from a whispering-gallery-mode disk resonator," *Phys. Rev. Lett.*, vol. 106, p. 113 901, 11 Mar. 2011. DOI: 10.1103/PhysRevLett.106.113901.

[175] M. Kues *et al.*, "Quantum optical microcombs," *Nature Photonics 2019 13:3*, vol. 13, pp. 170–179, 3 Feb. 2019, ISSN: 1749-4893. DOI: 10.1038/s41566-019-0363-0.

[176] R. Simon, "Peres-horodecki separability criterion for continuous variable systems," *Physical Review Letters*, vol. 84, p. 2726, 12 Mar. 2000, ISSN: 10797114. DOI: 10.1103/PhysRevLett.84.2726.

[177] R. F. Werner and M. M. Wolf, "Bound entangled gaussian states," *Physical Review Letters*, vol. 86, p. 3658, 16 Apr. 2001, ISSN: 00319007. DOI: 10.1103/PhysRevLett.86.3658.

[178] G. Vidal and R. F. Werner, "Computable measure of entanglement," *Physical Review A*, vol. 65, p. 032 314, 3 Feb. 2002, ISSN: 10502947. DOI: 10.1103/PhysRevA.65.032314.

[179] M. Li *et al.*, "Multi-color continuous-variable quantum entanglement in dissipative kerr solitons," *ArXiv e-prints*, DOI: https://doi.org/10.48550/arXiv.2101.07734. arXiv: 2101.07734.

[180] M. A. Guidry, D. M. Lukin, K. Y. Yang, R. Trivedi, and J. Vučković, "Quantum optics of soliton microcombs," *Nature Photonics 2021 16:1*, vol. 16, pp. 52–58, 1 Dec. 2021, ISSN: 1749-4893. DOI: 10.1038/S41566-021-00901-Z.

[181] O. F. Anjum *et al.*, "Bandwidth enhancement of inter-modal four wave mixing bragg scattering by means of dispersion engineering," *APL Photonics*, vol. 4, p. 022 902, 2 Dec. 2018, ISSN: 23780967. DOI: 10.1063/1.5048495.

[182] E. Zhu, C. Zhao, and H. Li, "Frequency-domain model of optical frequency-comb generation in optical resonators with second- and third-order nonlinearities," *Physical Review A*, vol. 102, p. 053 508, 5 Nov. 2020, ISSN: 24699934. DOI: 10.1103/PHYSREVA.102.053508/FIGURES/4/MEDIUM.

[183] G. Grynberg, A. Aspect, C. Fabre, and C. Cohen-Tannoudji, *Introduction to Quantum Optics*. Cambridge University Press, 2010. DOI: 10.1017/cbo9780511778261.

[184] C. Gardiner, *Quantum Noise*. Springer, 2004.

[185] A. Barchielli and B. Vacchini, "Quantum langevin equations for optomechanical systems," *New Journal of Physics*, vol. 17, p. 083 004, 8 Aug. 2015, ISSN: 1367-2630. DOI: 10.1088/1367-2630/17/8/083004.

[186] A. S. Hodel, B. Tenison, and K. R. Poolla, "Numerical solution of the lyapunov equation by approximate power iteration," *Linear Algebra and its Applications*, vol. 236, pp. 205–230, Mar. 1996, ISSN: 0024-3795. DOI: 10.1016/0024-3795(94)00155-3.

[187] J. Lee, M. S. Kim, Y. J. Park, and S. Lee, "Partial teleportation of entanglement in a noisy environment," *Journal of Modern Optics*, vol. 47, no. 12, pp. 2151–2164, 2000. DOI: 10.1080/09500340008235138. eprint: https://doi.org/10.1080/09500340008235138.

[188] M. S. Kim, J. Lee, and W. J. Munro, "Experimentally realizable characterizations of continuous-variable gaussian states," *Phys. Rev. A*, vol. 66, p. 030 301, 3 Sep. 2002. DOI: 10.1103/PhysRevA.66.030301.

[189] G. Adesso, A. Serafini, and F. Illuminati, "Extremal entanglement and mixedness in continuous variable systems," *Physical Review A - Atomic, Molecular, and Optical Physics*, vol. 70, p. 022 318, 2 Aug. 2004, ISSN: 10502947. DOI: 10.1103/PHYSREVA.70.022318/FIGURES/9/MEDIUM.

[190] S. Olivares, "Quantum optics in the phase space," *The European Physical Journal Special Topics 2012 203:1*, vol. 203, pp. 3–24, 1 Apr. 2012, ISSN: 1951-6401. DOI: 10.1140/EPJST/E2012-01532-4.

[191] D. C. Cole, E. S. Lamb, P. Del'Haye, S. A. Diddams, and S. B. Papp, "Soliton crystals in kerr resonators," *Nature Photonics 2017 11:10*, vol. 11, pp. 671–676, 10 Sep. 2017, ISSN: 1749-4893. DOI: 10.1038/s41566-017-0009-z.

[192] S. Fujii and T. Tanabe, "Dispersion engineering and measurement of whispering gallery mode microresonator for kerr frequency comb generation," *Nanophotonics*, vol. 9, pp. 1087–1104, 5 May 2020, ISSN: 21928614. DOI: 10.1515/NANOPH-2019-0497/MACHINEREADABLECITATION/RIS.

[193] C. W. Gardiner and M. J. Collett, "Input and output in damped quantum systems: Quantum stochastic differential equations and the master equation," *Physical Review A*, vol. 31, p. 3761, 6 Jun. 1985, ISSN: 10502947. DOI: 10.1103/PhysRevA.31.3761.

[194] A. S. Parkins, C. W. Gardiner, and M. J. Collett, "Input and output in damped quantum systems. ii. methods in non-white-noise situations and application to inhibition of atomic phase decays," *JOSA B, Vol. 4, Issue 10, pp. 1683-1699*, vol. 4, pp. 1683–1699, 10 Oct. 1987, ISSN: 1520-8540. DOI: 10.1364/JOSAB.4.001683.

[195] D. F. Walls and G. J. Milburn, *Quantum optics*. Springer Berlin Heidelberg, 2008, pp. 1–425, ISBN: 9783540285731. DOI: 10.1007/978-3-540-28574-8.

[196] S. Thomas and P. Senellart, "The race for the ideal single-photon source is on," *Nature Nanotechnology*, vol. 16, no. 4, pp. 367–368, Apr. 2021, ISSN: 1748-3395. DOI: 10.1038/s41565-021-00851-1.

[197] N. Tomm *et al.*, "A bright and fast source of coherent single photons," *Nature Nanotechnology*, vol. 16, no. 4, pp. 399–403, Apr. 2021, ISSN: 1748-3395. DOI: 10.1038/s41565-020-00831-x.

[198] P. Senellart, G. Solomon, and A. White, "High-performance semiconductor quantum-dot single-photon sources," *Nature Nanotechnology*, vol. 12, no. 11, pp. 1026–1039, Nov. 2017, ISSN: 1748-3395. DOI: 10.1038/nnano.2017.218.

[199] G. J. Mendoza *et al.*, "Active temporal and spatial multiplexing of photons," *Optica*, vol. 3, no. 2, pp. 127–132, Feb. 2016. DOI: 10.1364/OPTICA.3.000127.

[200] M. J. Collins *et al.*, "Integrated spatial multiplexing of heralded single-photon sources," *Nature Communications*, vol. 4, no. 1, p. 2582, Oct. 2013, ISSN: 2041-1723. DOI: 10.1038/ncomms3582.

[201] R. J. A. Francis-Jones, R. A. Hoggarth, and P. J. Mosley, "All-fiber multiplexed source of high-purity single photons," *Optica*, vol. 3, no. 11, pp. 1270–1273, Nov. 2016. DOI: 10.1364/OPTICA.3.001270.

[202] D. Bonneau, G. J. Mendoza, J. L. O'Brien, and M. G. Thompson, "Effect of loss on multiplexed single-photon sources," *New Journal of Physics*, vol. 17, no. 4, p. 043 057, Apr. 2015. DOI: 10.1088/1367-2630/17/4/043057.

[203] A. L. Migdall, D. Branning, and S. Castelletto, "Tailoring single-photon and multiphoton probabilities of a single-photon on-demand source," *Phys. Rev. A*, vol. 66, p. 053 805, 5 Nov. 2002. DOI: 10.1103/PhysRevA.66.053805.

[204] F. N. Wong and J. H. Shapiro, "On-demand single-photon generation using a modular array of parametric downconverters with electro-optic polarization controls," *Optics Letters, Vol. 32, Issue 18, pp. 2698-2700*, vol. 32, pp. 2698–2700, 18 Sep. 2007, ISSN: 1539-4794. DOI: 10.1364/OL.32.002698.

[205] K. T. Kaczmarek *et al.*, "High-speed noise-free optical quantum memory," *Phys. Rev. A*, vol. 97, p. 042 316, 4 Apr. 2018. DOI: 10.1103/PhysRevA.97.042316.

[206] N. Sinclair *et al.*, "Spectral multiplexing for scalable quantum photonics using an atomic frequency comb quantum memory and feed-forward control," *Phys. Rev. Lett.*, vol. 113, p. 053 603, 5 Jul. 2014. DOI: 10.1103/PhysRevLett.113.053603.

[207] C. Joshi, A. Farsi, S. Clemmen, S. Ramelow, and A. L. Gaeta, "Frequency multiplexing for quasi-deterministic heralded single-photon sources," *Nature Communications 2018 9:1*, vol. 9, pp. 1–8, 1 Feb. 2018, ISSN: 2041-1723. DOI: 10.1038/s41467-018-03254-4.

[208] M. Grimau Puigibert *et al.*, "Heralded single photons based on spectral multiplexing and feed-forward control," *Phys. Rev. Lett.*, vol. 119, p. 083 601, 8 Aug. 2017. DOI: 10.1103/PhysRevLett.119.083601.

[209] H. Yu *et al.*, "Spectrally multiplexed indistinguishable single-photon generation at telecom-band," *Photon. Res.*, vol. 10, no. 6, pp. 1417–1429, Jun. 2022. DOI: 10.1364/PRJ.450731.

[210] P. Fisher, R. Cernansky, B. Haylock, and M. Lobino, "Single photon frequency conversion for frequency multiplexed quantum networks in the telecom band," *Phys. Rev. Lett.*, vol. 127, p. 023 602, 2 Jul. 2021. DOI: 10.1103/PhysRevLett.127.023602.

[211] B. A. Bell, J. He, C. Xiong, and B. J. Eggleton, "Frequency conversion in silicon in the single photon regime," *Opt. Express*, vol. 24, no. 5, pp. 5235–5242, Mar. 2016. DOI: 10.1364/OE.24.005235.

[212] M. Kues *et al.*, "Quantum optical microcombs," *Nature Photonics 2019 13:3*, vol. 13, pp. 170–179, 3 Feb. 2019, ISSN: 1749-4893. DOI: 10.1038/s41566-019-0363-0.

[213] M. Pysher, Y. Miwa, R. Shahrokhshahi, R. Bloomer, and O. Pfister, "Parallel generation of quadripartite cluster entanglement in the optical frequency comb," *Phys. Rev. Lett.*, vol. 107, p. 030 505, 3 Jul. 2011. DOI: 10.1103/PhysRevLett.107.030505.

[214] N. C. Menicucci, S. T. Flammia, and O. Pfister, "One-way quantum computing in the optical frequency comb," *Physical Review Letters*, vol. 101, p. 130 501, 13 Sep. 2008, ISSN: 00319007. DOI: 10.1103/PHYSREVLETT.101.130501/FIGURES/3/MEDIUM.

[215] A. Pasquazi *et al.*, "Micro-combs: A novel generation of optical sources," *Physics Reports*, vol. 729, pp. 1–81, Jan. 2018, ISSN: 03701573. DOI: 10.1016/J.PHYSREP.2017.08.004.

[216] C. Reimer *et al.*, "Integrated frequency comb source of heralded single photons," *Opt. Express*, vol. 22, no. 6, pp. 6535–6546, Mar. 2014. DOI: 10.1364/OE.22.006535.

[217] C. Reimer *et al.*, "Generation of multiphoton entangled quantum states by means of integrated frequency combs," *Science*, vol. 351, no. 6278, pp. 1176–1180, 2016. DOI: 10.1126/science.aad8532. eprint: https://www.science.org/doi/pdf/10.1126/science.aad8532.

[218] L. Caspani *et al.*, "Multifrequency sources of quantum correlated photon pairs on-chip: A path toward integrated quantum frequency combs," *Nanophotonics*, vol. 5, no. 2, pp. 351–362, 2016. DOI: doi:10.1515/nanoph-2016-0029.

[219] M. Kues *et al.*, "On-chip generation of high-dimensional entangled quantum states and their coherent control," *Nature 2017 546:7660*, vol. 546, pp. 622–626, 7660 Jun. 2017, ISSN: 1476-4687. DOI: 10.1038/nature22986.

[220] B. M. Burridge, I. I. Faruque, J. G. Rarity, and J. Barreto, "High spectro-temporal purity single-photons from silicon micro-racetrack resonators using a dual-pulse configuration," *Opt. Lett.*, vol. 45, no. 14, pp. 4048–4051, Jul. 2020. DOI: 10.1364/OL.393077.

[221] Z. Yang *et al.*, "A squeezed quantum microcomb on a chip," *Nature Communications 2021 12:1*, vol. 12, pp. 1–8, 1 Aug. 2021, ISSN: 2041-1723. DOI: 10.1038/s41467-021-25054-z.

[222] A. Pasquazi *et al.*, "All-optical wavelength conversion in an integrated ring resonator," *Opt. Express*, vol. 18, no. 4, pp. 3858–3863, Feb. 2010. DOI: 10.1364/OE.18.003858.

[223] M. Heuck *et al.*, "Unidirectional frequency conversion in microring resonators for on-chip frequency-multiplexed single-photon sources," *New Journal of Physics*, vol. 21, p. 033 037, 3 Mar. 2019, ISSN: 1367-2630. DOI: 10.1088/1367-2630/AB09A7.

[224] M. Beck, "Comparing measurements of $g^{\{}(2)\}(0)$ performed with different coincidence detection techniques," *JOSA B, Vol. 24, Issue 12, pp. 2972-2978*, vol. 24, pp. 2972–2978, 12 Dec. 2007, ISSN: 1520-8540. DOI: 10.1364/JOSAB.24.002972.

[225] J. B. Christensen, J. G. Koefoed, K. Rottwitt, and C. J. McKinstrie, "Engineering spectrally unentangled photon pairs from nonlinear microring resonators by pump manipulation," *Opt. Lett.*, vol. 43, no. 4, pp. 859–862, Feb. 2018. DOI: 10.1364/OL.43.000859.

[226] Z. Vernon *et al.*, "Truly unentangled photon pairs without spectral filtering," *Opt. Lett.*, vol. 42, no. 18, pp. 3638–3641, Sep. 2017. DOI: 10.1364/OL.42.003638.

[227] G. Enzian *et al.*, "Observation of brillouin optomechanical strong coupling with an 11ghz mechanical mode," *Optica, Vol. 6, Issue 1, pp. 7-14*, vol. 6, pp. 7–14, 1 Jan. 2019, ISSN: 2334-2536. DOI: 10.1364/OPTICA.6.000007.

[228] X. Yi, "Physics and applications of microresonator solitons and electro-optic frequency combs," 2017.

[229] J. M. Dudley, G. Genty, and S. Coen, "Supercontinuum generation in photonic crystal fiber," *Reviews of Modern Physics*, vol. 78, pp. 1135–1184, 4 Oct. 2006, ISSN: 00346861. DOI: 10.1103/REVMODPHYS.78.1135/FIGURES/28/MEDIUM.

Appendix A

Numerical solution to the Lugiato-Lefever Equation

The normalised Lugiato-Lefever equation is given by (see Chapter 2):

$$\frac{\partial\psi}{\partial\tau} = -\left(1+i\alpha\right)\psi + i\left|\psi\right|^2\psi - \frac{i\beta}{2}\frac{\partial^2\psi}{\partial\theta^2} + F, \tag{A.1}$$

with the (all parameters are dimensionless) cavity field ($\psi = \psi\left(\theta,\tau\right)$) as a function of time (τ) and position around the resonator (θ). The system is made of a resonator with second-order dispersion characterised by a magnitude β and is forced by a field F that is detuned from the pump mode by an amount α.

The method to solve this equation is described in [228], taking from the works [60, 229], and adapted here for completeness. In this context, solution of the equation means the propagation of the field amplitudes in time: $\psi\left(\theta,\tau\right) \rightarrow \psi\left(\theta,\tau+\delta\tau\right)$, in an efficient manner such that a steady-state solution is converged upon quickly.

1. Convert the field into the frequency domain using the Fast Fourier Transform (FFT) over the spatial distribution. The resultant frequency domain field is denoted by a tilde, and is parameterised by a mode number l.

$$\tilde{\psi}\left(l,\tau\right) = \mathrm{FFT}_\theta\left(\psi\left(\theta,\tau\right)\right). \tag{A.2}$$

2. Propagate $\tilde{\psi}$ in time by $\frac{\delta\tau}{2}$, accounting only for the dispersive term. In the Fourier domain, this evolution is straightforward and the resulting fields are denoted with a subscript D to show that dispersion has been accounted for.

$$\tilde{\psi}_D\left(l,\tau+\frac{\delta\tau}{2}\right) = \exp\left(-\beta\frac{il^2}{2}\frac{\delta\tau}{2}\right)\tilde{\psi}\left(l,\tau\right). \tag{A.3}$$

3. Transform back into the spatial domain using the Inverse Fast Fourier Transform (IFFT) over the frequency variable.

$$\psi_D\left(\theta,\tau+\frac{\delta\tau}{2}\right) = \mathrm{IFFT}_l\left(\tilde{\psi}_D\left(l,\tau+\frac{\delta\tau}{2}\right)\right). \tag{A.4}$$

4. Evolve these fields in time - this time for the entire time-step $\delta\tau$ - accounting for all the other terms (the Kerr effect, detuning, dissipation and forcing). The

result has a subscript N to show the nonlinear effects have been accounted for.

$$\psi_N(\theta, \tau + \delta\tau) = \exp\left(-(1 + i\alpha) + i\left|\psi_D\left(\theta, \tau + \frac{\delta\tau}{2}\right)\right|^2\right)\psi_D\left(\theta, \tau + \frac{\delta\tau}{2}\right) + \delta\tau F. \quad \text{(A.5)}$$

5. Repeat steps 1 & 2 to account for the remaining half-time-step of dispersion, now using subscript $N+D$ to show both nonlinearity and dispersion have been accounted for.

$$\tilde{\psi}_N(\theta, \tau + \delta\tau) = \mathrm{FFT}_\theta\left(\psi_N(\theta, \tau + \delta\tau)\right), \quad \text{(A.6)}$$

$$\tilde{\psi}_{N+D}(l, \tau + \delta\tau) = \exp\left(-\beta\frac{il^2}{2}\frac{\delta\tau}{2}\right)\tilde{\psi}_N(\theta, \tau + \delta\tau). \quad \text{(A.7)}$$

6. Perform the IFFT to get back to the time domain.

$$\psi(\theta, \tau + \delta\tau) = \mathrm{IFFT}_l\left(\tilde{\psi}_{N+D}(l, \tau + \delta\tau)\right). \quad \text{(A.8)}$$

7. *Optional.* Add noise to excite four-wave mixing. This can be done in the frequency domain to a level that would be expected from quantum fluctuations if preferred.

The solution of the LLE (with inputs $F = 1.91$, $\alpha = 4.16$, $\beta = -0.15$) is shown in Fig. A.1. The input values, along with an initial condition for $\psi(\theta, \tau = 0)$ that has a small pulse, was used found to give the desired evolution into a single soliton state.

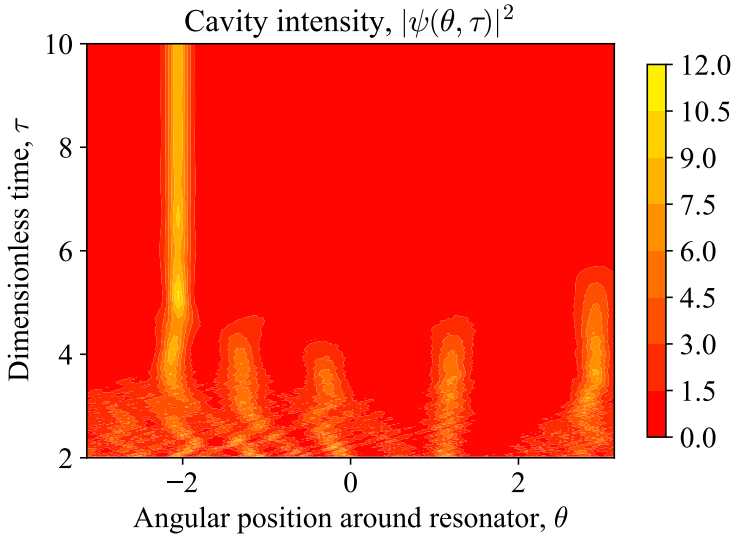

(a)

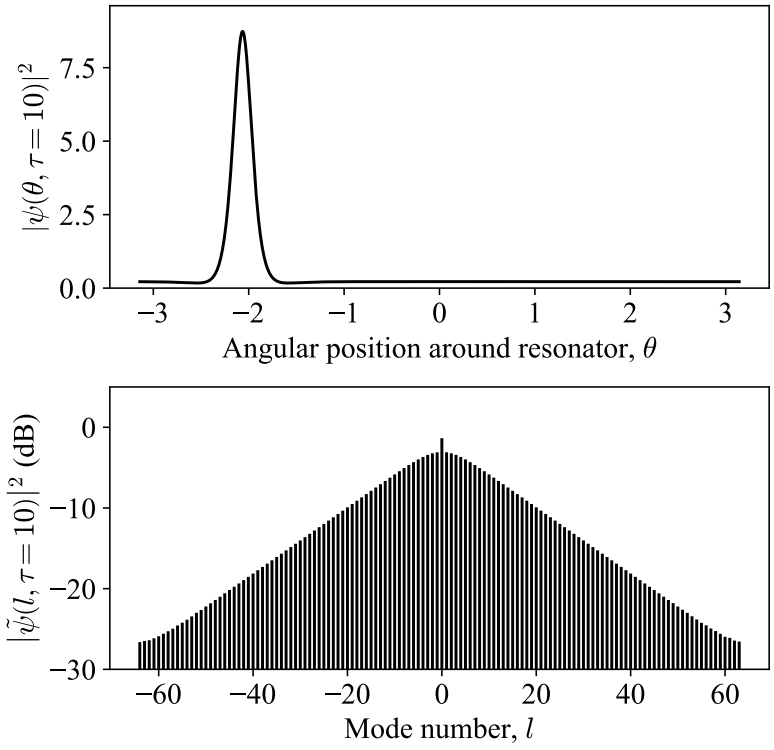

(b)

Figure A.1: a) Evolution of a cavity field under the LLE with inputs $F = 1.91$, $\alpha = 4.16$, $\beta = -0.15$. Before $\tau = 2$ the solution is highly chaotic and so not shown. Between $\tau \approx 2-6$, there are a number of pulses inside the cavity that are interacting, settling down to a single pulse after $\tau = 6$. b) Cavity field at $\tau = 10$. The LLE solution shows a soliton: a sharp pulse in the spatial domain, and a sech^2 profile in the frequency domain.

Appendix B

Covariance matrix of a two-mode squeezed vacuum

Let the two-mode squeezed vacuum be denoted by:

$$|\xi\rangle = S(\xi)\,|0,0\rangle\,, \tag{B.1}$$

$$= \exp\left(\xi\hat{a}^{\dagger}\hat{b}^{\dagger} - \xi^{\star}\hat{a}\hat{b}\right)|0,0\rangle\,, \tag{B.2}$$

where $\xi = re^{i\phi}$ is the squeezing parameter, and $\hat{a}^{\dagger}$ ($\hat{a}$), $\hat{b}^{\dagger}$ ($\hat{b}$), being the creation (annihilation) operators for the two modes of the system. In the Fock basis, this expands to:

$$|\xi\rangle = \frac{1}{\cosh(r)}\sum_{n}^{\infty} e^{in\phi}\tanh^{n}(r)\,|n,n\rangle\,, \tag{B.3}$$

and the associated Hermitian conjugate:

$$\langle\xi| = \frac{1}{\cosh(r)}\sum_{n}^{\infty} e^{-in\phi}\tanh^{n}(r)\,\langle n,n|\,. \tag{B.4}$$

The quadrature operators of these systems are given by:

$$\hat{X}_{\mathrm{A}} = \frac{\hat{a}^{\dagger} + \hat{a}}{\sqrt{2}}, \tag{B.5a}$$

$$\hat{X}_{\mathrm{B}} = \frac{\hat{b}^{\dagger} + \hat{b}}{\sqrt{2}}, \tag{B.5b}$$

$$\hat{Y}_{\mathrm{A}} = \frac{i\left(\hat{a}^{\dagger} - \hat{a}\right)}{\sqrt{2}}, \tag{B.5c}$$

$$\hat{Y}_{\mathrm{B}} = \frac{i\left(\hat{b}^{\dagger} - \hat{b}\right)}{\sqrt{2}}, \tag{B.5d}$$

The covariance matrix of such a state is given by (N.B. all first-order moments are zero):

$$\boldsymbol{V} = \begin{bmatrix} \left\langle \hat{X}_{\mathrm{A}}^2 \right\rangle, & \left\langle \left\{ \hat{X}_{\mathrm{A}}, \hat{Y}_{\mathrm{A}} \right\} \right\rangle, & \left\langle \hat{X}_{\mathrm{A}} \hat{X}_{\mathrm{B}} \right\rangle, & \left\langle \hat{X}_{\mathrm{A}} \hat{Y}_{\mathrm{B}} \right\rangle \\ \left\langle \left\{ \hat{Y}_{\mathrm{A}}, \hat{X}_{\mathrm{A}} \right\} \right\rangle, & \left\langle \hat{Y}_{\mathrm{A}}^2 \right\rangle, & \left\langle \hat{Y}_{\mathrm{A}} \hat{X}_{\mathrm{B}} \right\rangle, & \left\langle \hat{Y}_{\mathrm{A}} \hat{Y}_{\mathrm{B}} \right\rangle \\ \left\langle \hat{X}_{\mathrm{B}} \hat{X}_{\mathrm{A}} \right\rangle, & \left\langle \hat{X}_{\mathrm{B}} \hat{Y}_{\mathrm{A}} \right\rangle, & \left\langle \hat{X}_{\mathrm{B}}^2 \right\rangle, & \left\langle \left\{ \hat{X}_{\mathrm{B}}, \hat{Y}_{\mathrm{B}} \right\} \right\rangle \\ \left\langle \hat{Y}_{\mathrm{B}} \hat{X}_{\mathrm{A}} \right\rangle, & \left\langle \hat{Y}_{\mathrm{B}} \hat{Y}_{\mathrm{A}} \right\rangle, & \left\langle \left\{ \hat{Y}_{\mathrm{B}}, \hat{X}_{\mathrm{B}} \right\} \right\rangle, & \left\langle \hat{Y}_{\mathrm{B}}^2 \right\rangle \end{bmatrix}, \tag{B.6}$$

with the anti-commutator expectation $\left\langle \left\{ \hat{A}, \hat{B} \right\} \right\rangle = \frac{1}{2} \left\langle \hat{A}\hat{B} + \hat{B}\hat{A} \right\rangle$, and the fact that many of these operators commute ensuring that many of the elements are replicated. The independent parameters will now be derived:

Diagonal elements

The following method shows how to calculate $\left\langle \hat{X}_{\mathrm{A}}^2 \right\rangle$ (which is the same as $\left\langle \hat{X}_{\mathrm{B}}^2 \right\rangle$ due to the symmetry of how the operators work on both systems):

$$\begin{aligned} \left\langle \hat{X}_{\mathrm{A}}^2 \right\rangle &= \langle \xi | \, \hat{X}_{\mathrm{A}}^2 \, | \xi \rangle \,, \\ &= \frac{1}{2\cosh^2(r)} \sum_{m,n=0}^{\infty} e^{i\phi(n-m)} \tanh^{(n+m)}(r) \, \langle m, m | \left(\hat{a}^\dagger + \hat{a} \right) \left(\hat{a}^\dagger + \hat{a} \right) | n, n \rangle \,, \\ &= \frac{1}{2\cosh^2(r)} \sum_{m,n=0}^{\infty} e^{i\phi(n-m)} \tanh^{(n+m)}(r) \, \langle m, m | \left(\hat{a}^\dagger \hat{a}^\dagger + \hat{a}\hat{a}^\dagger + \hat{a}^\dagger \hat{a} + \hat{a}\hat{a} \right) | n, n \rangle \,, \\ &= \frac{1}{2\cosh^2(r)} \sum_{m,n=0}^{\infty} e^{i\phi(n-m)} \tanh^{(n+m)}(r) \, (2n+1) \, \delta_{m,n}, \\ &= \frac{1}{2\cosh^2(r)} \sum_{n=0}^{\infty} \tanh^{(2n)}(r) \, (2n+1) \,, \\ &= \frac{\cosh(2r)}{2}. \end{aligned} \tag{B.7}$$

Only the $\hat{a}^\dagger \hat{a}$ and $\hat{a}\hat{a}^\dagger$ terms added to this expectation due to the orthogonality of different Fock states. In calculating $\left\langle \hat{Y}_{\mathrm{A,B}}^2 \right\rangle$, the sign of these terms are flipped, but this is reversed by the two imaginary prefactors to the $\hat{Y}$ operators - thus all diagonal terms are the same.

Anti-commutator terms

Symmetries in the anti-commutator terms ensures that they all have the same value. Looking at one example of these:

$$\begin{aligned} \left\{ \hat{X}_{\mathrm{A}}, \hat{Y}_{\mathrm{A}} \right\} &= \hat{X}_{\mathrm{A}} \hat{Y}_{\mathrm{A}} + \hat{Y}_{\mathrm{A}} \hat{X}_{\mathrm{A}}, \\ &= \frac{i}{2} \left(\left(\hat{a}^\dagger + \hat{a} \right) \left(\hat{a}^\dagger - \hat{a} \right) + \left(\hat{a}^\dagger - \hat{a} \right) \left(\hat{a}^\dagger + \hat{a} \right) \right), \\ &= i \left(\hat{a}^\dagger \hat{a}^\dagger - \hat{a}\hat{a} \right), \end{aligned} \tag{B.8}$$

which only includes terms that would lead to orthogonal Fock states in the expectation calculation and so all of these terms are zero.

Coupling terms

The symmetry of how the operators act on both systems, and the fact operators that act on different states together mean that the remaining elements of the matrix are only made of two independent values. These will be taken as $\left\langle \hat{X}_{\mathrm{A}}\hat{X}_{\mathrm{B}} \right\rangle$ and $\left\langle \hat{X}_{\mathrm{A}}\hat{Y}_{\mathrm{B}} \right\rangle$.

$$\begin{aligned}\left\langle \hat{X}_{\mathrm{A}}\hat{X}_{\mathrm{B}} \right\rangle &= \langle \xi | \, \hat{X}_{\mathrm{A}}^2 \, | \xi \rangle \,, \\ &= \frac{1}{2\cosh^2(r)} \sum_{m,n=0}^{\infty} e^{i\phi(n-m)} \tanh^{(n+m)}(r) \, \langle m,m | \left(\hat{a}^\dagger + \hat{a}\right) \left(\hat{b}^\dagger + \hat{b}\right) | n,n \rangle \,.\end{aligned} \tag{B.9}$$

Now, in order to retain the parity of the photon number in both systems, which is needed for a term to add to the expectation value, only the $\hat{a}^\dagger\hat{b}^\dagger$ and $\hat{a}\hat{b}$ terms need be included.

$$\begin{aligned}\left\langle \hat{X}_{\mathrm{A}}\hat{X}_{\mathrm{B}} \right\rangle &= \frac{1}{2\cosh^2(r)} \sum_{m,n=0}^{\infty} e^{i\phi(n-m)} \tanh^{(n+m)}(r) \, \langle m,m | \left(\hat{a}^\dagger\hat{b}^\dagger + \hat{a}\hat{b}\right) | n,n \rangle \,, \\ &= \frac{1}{2\cosh^2(r)} \sum_{m,n=0}^{\infty} e^{i\phi(n-m)} \tanh^{(n+m)}(r) \left(m\delta_{m,n+1} + n\delta_{m+1,n}\right) , \\ &= \frac{1}{2\cosh^2(r)} \sum_{n=0}^{\infty} (n+1) \tanh^{(2n+1)}(r) \left(e^{-i\phi} + e^{i\phi}\right) , \\ &= \frac{1}{2}\cos(\phi)\sinh(2r).\end{aligned} \tag{B.10}$$

Using a similar method we arrive at:

$$\left\langle \hat{X}_{\mathrm{A}}\hat{Y}_{\mathrm{B}} \right\rangle = \frac{1}{2}\sin(\phi)\sinh(2r). \tag{B.11}$$